



UNIVERSIDADE FEDERAL DO CEARÁ
TECHNOLOGY CENTER
DEPARTMENT OF METALLURGICAL AND MATERIALS ENGINEERING
GRADUATE PROGRAM IN MATERIALS SCIENCE AND ENGINEERING
PHD IN MATERIALS SCIENCE AND ENGINEERING

PAULO HENRIQUE TEIXEIRA DA SILVA

**$\text{Bi}_3\text{R}_2\text{Ti}_3\text{FeO}_{15}$ (R=Bi, Gd, AND Nd) : FROM STRUCTURAL PROPERTIES TO
MICROWAVE DEVICE APPLICATIONS**

FORTALEZA

2022

PAULO HENRIQUE TEIXEIRA DA SILVA

**$\text{Bi}_3\text{R}_2\text{Ti}_3\text{FeO}_{15}$ (R=Bi, Gd, AND Nd) : FROM STRUCTURAL PROPERTIES TO
MICROWAVE DEVICE APPLICATIONS**

Doctorate thesis submitted to Graduate Program in Materials Science and Engineering at the Technology Center of the Universidade Federal do Ceará, for the obtainment of the title of PhD in Materials Science and Engineering. Study Area: Physical and Mechanical Properties of Materials

Supervisor: Prof. Dr. Pierre Basílio Almeida Fechine

FORTALEZA

2022

Dados Internacionais de Catalogação na Publicação
Universidade Federal do Ceará
Sistema de Bibliotecas
Gerada automaticamente pelo módulo Catalog, mediante os dados fornecidos pelo(a) autor(a)

S582b Silva, Paulo Henrique Teixeira da.
Bi₃R₂Ti₃FeO₁₅ (R = Bi, Gd, and Nd): from structural properties to microwave device applications /
Paulo Henrique Teixeira da Silva. – 2022.
98 f. : il. color.

Tese (doutorado) – Universidade Federal do Ceará, Centro de Tecnologia, Programa de Pós-Graduação
em Engenharia e Ciência de Materiais, Fortaleza, 2022.
Orientação: Prof. Dr. Pierre Basílio Almeida Fachine.

1. Bi₅Ti₃FeO₁₅. 2. Terras-raras. 3. Aurivillius. 4. CDRA. I. Título.

CDD 620.11

PAULO HENRIQUE TEIXEIRA DA SILVA

**$\text{Bi}_3\text{R}_2\text{Ti}_3\text{FeO}_{15}$ (R=Bi, Gd, AND Nd) : FROM STRUCTURAL PROPERTIES TO
MICROWAVE DEVICE APPLICATIONS**

Doctorate thesis submitted to Graduate Program in Materials Science and Engineering at the Technology Center of the Universidade Federal do Ceará, for the obtainment of the title of PhD in Materials Science and Engineering. Study Area: Physical and Mechanical Properties of Materials

Approval Date: July 5, 2022

COMITTE MEMBERS

Prof. Dr. Pierre Basílio Almeida Fechine (Supervisor)
Universidade Federal do Ceará (UFC)

Prof. Dr. Francisco Nivaldo Aguiar Freire
Universidade Federal do Ceará (UFC)

Prof. Dr. Antonio Sergio Bezerra Sombra
Universidade Federal do Ceará (UFC)

Prof. Dr. Felipe Bohn
Universidade Federal do Rio Grande do Norte (UFRN)

Prof. Dr. Rafael Melo Freire
Instituto de Investigaciones Agropecuarias - CRI La Platina (INIA)

Dedicated to my wife, Nadieli Alves, whose love, support and inspiration for the last ten plus years have been fundamental to my professional achievements and personal happiness.

ACKNOWLEDGEMENTS

Many people contributed directly or indirectly to my professional and personal growth, obviously an achievement of such difficulty is not only due to my individual merits. I had help from the shoulders of giants for me achieve this goal.

First of all, I would like to thank God for giving me the necessary seriousness whenever I asked.

I thank my wife, Nadieli Alves, for always supporting my decisions, understanding my constant absence, and believing in my dreams.

I would like to thank my family for their support. Especially my mother Maria José and my Father Paulo Agostinho, was fundamental for me to become the person I am today.

I would like to express my sincere gratitude to my supervisor Dr. Pierre Basílio Almeida Fechine for the continuous support of my Ph.D study and research, for his patience, motivation, enthusiasm, and immense knowledge. I could not have imagined having a better supervisor and mentor for my Ph.D study.

To my friend and co-supervisor Marcelo Antonio Santos da Silva, for all the hours of conversations and support in order to show me the best ways to conduct my work.

I am grateful for all the academic support offered by the Universidade Federal do Ceará, especially the Graduate Program in Materials Science and Engineering, Department of Metallurgical and Materials Engineering.

To Advanced Materials Chemistry Group (GQMat) and its great team. Thank you so much for all the memories, conversations and debates we share in our lab, at the University, and at other social gatherings (happy hour). These will be unforgettable years that I will keep in my memory.

To prof. Dr. Antonio Sergio Bezerra Sombra, from Universidade Federal do Ceará- LOCEM, for for its technical support and access to the equipment of the Laboratory of Telecommunications and Science and Materials Engineering (LOCEM). To Prof. Dr. Alejandro Pedro Ayala, from Universidade Federal do Ceará, for making the Raman spectroscopy, Prof. Dr. Alan Silva de Menezes, from Universidade Federal do Maranhão, for making the Powder X-ray Diffraction, Prof. Dr. Felipe Bohn, Rodolfo Bezerra da Silva, and Marcio Assolin Correa, from Universidade Federal do Rio Grande do Norte, for making the Mössbauer spectroscopy and magnetic measurements available. All went essential for the development of the works presented in this thesis.

I would like to express my sincere gratitude to my committee members: Dr. Francisco Nivaldo Aguiar Freire, Dr. Antonio Sergio Bezerra Sombra, Dr. Felipe Bohn, and Dr. Rafael Melo Freire for their technical contributions and words of encouragement.

This study was financed in part by the Coordenação de Aperfeiçoamento de Pessoal de Nível Superior - Brasil (CAPES) - (Finance Code 001, PROEX 23038.000509/2020-82), Conselho Nacional de Desenvolvimento Científico e Tecnológico (CNPq) - (408790/2016-4), and Fundação Cearense de Apoio ao Desenvolvimento Científico e Tecnológico (Funcap) - (PNE-0112-00048.01.00/16).

RESUMO

Este trabalho compreende o estudo do material ferroelétrico estruturado em camada de bismuto $\text{Bi}_3\text{R}_2\text{Ti}_3\text{FeO}_{15}$ ($\text{R} = \text{Bi}, \text{Nd}$ e Gd) e a investigação de suas propriedades, visando avaliar esses materiais como alternativa para aplicação em dispositivos eletrônicos, como capacitores cerâmicos e antenas ressoadoras dielétricas cilíndricas (CDRA). Os materiais cerâmicos foram obtidos por reação de estado sólido convencional, e as caracterizações foram realizadas através das técnicas de PXR, Espectroscopia Raman, magnetização FC-ZFC, espectroscopia Mössbauer e espectroscopia de impedância, a fim de melhor compreender as relações entre as propriedades morfológicas e estruturais desses materiais cerâmicos e suas propriedades elétricas, magnéticas e dielétricas. A difração por raios-X e o refinamento Rietveld, revelam que todas as amostras apresentaram estrutura ortorrômbica com grupo espacial $A2_1am$. $\text{Bi}_3\text{Nd}_2\text{Ti}_3\text{FeO}_{15}$ (BNFTO) e $\text{Bi}_3\text{Gd}_2\text{Ti}_3\text{FeO}_{15}$ (BGFTO) apresentaram redução na distorção ortorrômbica quando comparados ao $\text{Bi}_5\text{Ti}_3\text{FeO}_{15}$ (BFTO). Para a análise Raman, mudanças significativas observadas na intensidade de alguns modos, bem como o deslocamento dos modos para frequências mais altas, ocorreram devido à substituição dos átomos de Bi nas camadas de perovskita pelos átomos mais leves de Gd e Nd. A suscetibilidade magnética de todas as amostras segue a lei de Curie-Weiss, com valores negativos da temperatura de Curie-Weiss, demonstrando que as interações magnéticas são de natureza antiferromagnética. As curvas de magnetização sugeriram um comportamento *weak canted ferromagnetic* para $T < 25$ K, seguido de um comportamento linear nas curvas em altas temperaturas. Medidas de espectroscopia Mössbauer revelaram um aumento dos valores de desdobramento quadrupolar à medida que a temperatura diminui, indicando que as amostras apresentam distorções locais, favorecendo a existência de fase ferromagnética fraca via interação Dzyaloshinskii-Moriya antisimétrica. A espectroscopia de impedância foi realizada para estabelecer uma correlação entre as propriedades elétricas e a microestrutura das cerâmicas. Uma relaxação do tipo não-Debye, induzida por um mecanismo termicamente ativado, pode ser observado em todas as amostras. Em caráter inovador, esses materiais foram aplicados como capacitores cerâmicos e CDRA. Os parâmetros de estabilidade térmica e de desempenho de operação, obtidos por análise experimental e simulada, são contrastados em detalhes com outros trabalhos publicados. Os resultados sugerem, que as três fases são novos candidatos para capacitores X4D, com excelente estabilidade de temperatura ($29\text{--}150$ °C, $\text{TCC} \leq \pm 3,3\%$). Além disso, as CDRA mostraram grande potencial para aplicação em microondas, operando na banda S. Uma mudança no valor de τ_f da fase BFTO ($-428,48$ ppm °C⁻¹) para BGFTO (+

59,17 ppm °C⁻¹) e BNFTO (+ 57,69 ppm °C⁻¹) é observada. Este resultado abre uma grande oportunidade para trabalhos futuros em CDRA com coeficientes de temperatura próximos de zero ($\tau_f \sim 0$).

Palavras-chave: Bi₅Ti₃FeO₁₅ . Terras-raras. Aurivillius . CDRA.

ABSTRACT

This work comprises the study of bismuth layer-structured ferroelectric material $\text{Bi}_3\text{R}_2\text{Ti}_3\text{FeO}_{15}$ ($\text{R} = \text{Bi}, \text{Nd}, \text{and Gd}$) and the investigation of their properties, aiming to evaluate these materials as alternative for application in electronic devices, such as ceramic capacitors and cylindrical dielectric resonator antenna (CDRA). The ceramic materials were obtained by conventional solid-state reaction, and the characterizations were performed through the techniques of PXRD, Raman Spectroscopy, FC-ZFC magnetization, Mössbauer spectroscopy, and Impedance spectroscopy, in order to better understand the relations between the morphological and structural properties of these ceramic materials and their electrical, magnetic, and dielectric properties. X-ray diffraction and Rietveld refinement reveal that all samples presented orthorhombic structure with $\text{A2}_1\text{am}$ space group. $\text{Bi}_3\text{Nd}_2\text{Ti}_3\text{FeO}_{15}$ (BNFTO) and $\text{Bi}_3\text{Gd}_2\text{Ti}_3\text{FeO}_{15}$ (BGFTO) presented a reduction in the orthorhombicity when compared to $\text{Bi}_5\text{Ti}_3\text{FeO}_{15}$ (BFTO). For the Raman analysis, significant changes observed in the intensity of some modes, as well as the shift of modes to higher frequencies, occurred due to the replacement of Bi atoms in the perovskite layers by the lighter Gd and Nd atoms. The magnetic susceptibility of all samples followed the Curie–Weiss law, with negative values of the Curie–Weiss temperature, demonstrating that the magnetic interactions are antiferromagnetic in nature. The magnetization curves suggested a weak canted ferromagnetic behavior for temperatures below 25 K, followed by a linear behavior in the curves at high temperatures. Mössbauer spectroscopy measurements revealed an increase of the quadrupole splitting values as the temperature decreases, indicating that the samples present local distortions, favoring the existence of weak ferromagnetic phase via the antisymmetric Dzyaloshinskii–Moriya interaction. Impedance spectroscopy was performed to establish a correlation between the electrical properties and the microstructure of the ceramics. A non-Debye relaxation induced by a thermally activated mechanism can be observed in all samples. In an innovative way, these materials were applied as ceramic capacitors and CDRA. The thermal stability and operating performance parameters, obtained by experimental and simulated analysis, are contrasted in detail with other published works. The results suggest that the three phases are new candidates for X4D capacitors, with excellent temperature stability ($29\text{--}150\text{ }^\circ\text{C}$, $\text{TCC} \leq \pm 3.3\%$). Furthermore, CDRA showed great potential for microwave application, operating in the S band. A change in the value of τ_f of the BFTO phase ($-428.48\text{ ppm }^\circ\text{C}^{-1}$) for BGFTO ($+ 59.17\text{ ppm }^\circ\text{C}^{-1}$) and BNFTO ($+ 57.69\text{ ppm }^\circ\text{C}^{-1}$) is observed. This result opens a great opportunity for future work on CDRA with temperature coefficients close to zero ($\tau_f \sim 0$).

Keywords: Bi₅Ti₃FeO₁₅ . Rare earth . Aurivillius . CDRA.

LIST OF FIGURES

Figure 1 – Approximate number of annual publications on the perovskite structure over the past eighty years. Data were taken from the Scopus database (searching for “perovskite”, “perovskite structure” AND “perovskite layer-structured”). The red arrows indicate a simplified timeline containing the most important contributions regarding layered perovskites.	19
Figure 2 – Applications for Layered perovskites.	20
Figure 3 – Idealised structures of the Aurivillius phases: (a) m=3 (b) m=4.	22
Figure 4 – Ratio of microwave dielectric compounds with different crystal structures.	24
Figure 5 – The frequency dependence of the real and imaginary parts of the dielectric constant in the presence of Space charge, hopping, dipole rotation, ionic, and electronic polarization mechanisms.	25
Figure 6 – Fields in a microwave resonance dielectric in the simplest standing wave mode: (a) magnetic field; (b) electric field, (c) variation in E_ϕ and H_z with r at $z = 0$, with reference to cylindrical coordinates (the z axis is perpendicular to the plane of the disc and the origin is at the disc centre).	27
Figure 7 – Resonant frequencies of a cylindrical resonator as a function of (a) the diameter of the resonator for three different ϵ_r values and (b) as a function of the resonator materials ϵ_r for three different geometries.	28
Figure 8 – (a) Impedance bandwidth according to the dielectric permittivity and loss tangent and (b) Radiation efficiency according to the dielectric permittivity and loss tangent.	29
Figure 9 – Frequency response of a microwave resonator.	31
Figure 10 – The microwave portion of the electromagnetic spectrum and its constituent bands and applications (from L to D band).	32
Figure 11 – (a) PXRD patterns of the BGFTO, BNFTO, and BFTO ceramics, at room temperature. (b) The (200) and (020) peaks of BFTO, BGFTO, and BNFTO. (c) Comparison of the orthorhombic distortion and the cell volume for the samples BGFTO, BNFTO, and BFTO. (d) Illustration of the 3D atomic structure of the $\text{Bi}_5\text{Ti}_3\text{FeO}_{15}$ compound	38

Figure 12 – Rietveld refinement of the BFTO PXRD pattern using the $A2_1am$ (ICSD-51862) and $Fmm2$ (ICSD-154483). The peaks ($2\theta = 19.5^\circ, 22.2^\circ, 28.9^\circ, 38.3^\circ,$ and 51.6° .) are identified with arrows.	39
Figure 13 – (a) Comparison of the Raman modes for the samples BFTO, BGFTO and BNFTO at room temperature. (b) Zoom view of the modes at low wavenumbers. (c) Experiment and theory for the Raman spectra of the BFTO, BGFTO and BNFTO ceramics at room temperature.	42
Figure 14 – ZFC and FC magnetization curves (left axis) and temperature dependence of the inverse of magnetic susceptibility (right axis) for the (a) BFTO, (b) BNFTO, and (c) BGFTO samples. The solid lines are fits obtained with the Curie–Weiss law.	45
Figure 15 – Isothermal magnetization curves for (a) BFTO, (b) BNFTO and (c) BGFTO samples. (d) Magnetic contribution at room temperature, obtained after removing the component χH from the magnetization curve measured at 300 K, for field values above 80 kOe.	47
Figure 16 – Mössbauer spectra of (a) BFTO, (b) BNFTO and (c) BGFTO compounds at $T = 12$ K and $T = 300$ K (inset). (d) Illustration to the replacement of Bi^{3+} ion by Nd^{3+} and Gd^{3+} . Different radii induce lattice distortion (compression) and tilting of FeO_6 octahedral by the Nd^{3+} , and Gd^{3+} ion doping into the Bi-site.	50
Figure 17 – SEM images of the samples: (a) BFTO, (b) BGFTO, and (c) BNFTO ceramics sintered at 1100°C for 3 h in air. The (d) BFTO, (e) BGFTO, and (f) BNFTO give the average grain size (AG), particle size distribution, and standard deviation (SD) of each ceramic.	54
Figure 18 – ϵ for (a) BFTO, (b) BGFTO, (c) BNFTO, and $\tan\delta$ for (d) BFTO, (e) BGFTO, (f) BNFTO as a function of frequency under different temperatures.	57
Figure 19 – ϵ for (a) BFTO, (b) BGFTO, (c) BNFTO, and $\tan\delta$ for (d) BFTO, (e) BGFTO, (f) BNFTO as a function of temperature under different frequencies.	58
Figure 20 – Z'' for (a) BFTO, (b) BGFTO, and (c) BNFTO ceramics as a function of frequency for different temperatures. The inset shows the normalized Z''/Z''_{max} shift of the peaks as a function of temperature. (d) Arrhenius plots for the samples at f_{max} versus $1000/T$	59

Figure 21 – Frequency dependence of M'' at various temperatures for (a) BFTO, (b) BGFTO, and (c) BNFTO. (d) Frequency dependence of the samples for σ_{ac} at temperature 260 °C.	61
Figure 22 – Nyquist diagrams for (a) BFTO, (b) BGFTO, and (c) BNFTO under various temperatures. (d) Equivalent circuit that best fitting the parameters of grain and grain boundaries.	63
Figure 23 – TCC as a function of temperature (29–150 °C) for (a) BFTO, (b) BGFTO, and (c) BNFTO under different frequency. (d) Variation of TCC for different frequencies. The dotted horizontal lines show the operating window for X4D capacitors.	65
Figure 24 – Plot of simulated and experimental data impedance of CDRA for (a) BFTO, (b) BGFTO, and (c) BNFTO. (d) Reflection coefficient S_{11} for CDRA from experimental data and numerical simulation). Inset shows the typical radiation profile and schematic setup used in CDRA measurements.	69

LIST OF TABLES

Table 1 – Examples of Aurivillius Phases with different layers.	21
Table 2 – Lattice parameters, density, crystallite size, microstrain, factors of the Rietveld analysis	37
Table 3 – The structural distortion parameter Δ of the samples	40
Table 4 – Summary and identification of the observed Raman modes positions for the BFTO, BGFTO, and BNFTO phases.	43
Table 5 – The hyperfine parameters of samples BFTO, BNFTO, and BGFTO at 12 and 300 K.	49
Table 6 – Dimensions, activation energy (measured from σ_{dc} , M''_{max} , and Z''_{max} spectrum) and the relative density for all samples.	60
Table 7 – Temperature dependence for parameters adjusted from the Nyquist diagram ($Z'' \times Z'$) for grain and grain boundary of BFTO, BGFTO, and BNFTO samples.	64
Table 8 – Sintered temperature (T_s), dielectric properties in MW, and temperature coefficient of capacitance (TCC) with EIA specification for all samples and previous works.	66
Table 9 – Antenna parameters and percent error for all samples and previous works.	67
Table 10 – Atomic positions and factors occupation the samples BFTO, BGFTO and BNFTO.	88
Table 11 – Distribution of the normal modes of vibration of the BFTO	89

CONTENTS

1	INTRODUCTION	17
1.1	Motivation	17
1.2	Bismuth Layer-Structured Ferroelectric Materials	20
1.3	Summary of Dielectric Ceramics Physics and Microwave Applications	24
1.3.1	<i>Dielectric Resonator Antenna</i>	26
1.4	Main Goal	33
1.5	Structure of this thesis	33
2	EFFECTS OF THE Bi^{3+} SUBSTITUTION ON THE STRUCTURAL, VIBRATIONAL, AND MAGNETIC PROPERTIES	34
2.1	Introduction	34
2.2	Experimental Methods	35
2.3	Results and Discussion	36
2.3.1	<i>Powder X-ray Diffraction</i>	36
2.3.2	<i>Raman Spectra Analysis</i>	40
2.3.3	<i>Magnetic Property Analysis</i>	44
2.3.4	<i>Mössbauer Spectra Analysis</i>	47
2.4	Conclusions	49
3	DIELECTRIC PROPERTIES OF BLSF AT MICROWAVE AND RA- DIOFREQUENCY	51
3.1	Introduction	51
3.2	Experimental Methods	52
3.3	Results and Discussion	53
3.3.1	<i>Morphological Analysis</i>	53
3.3.2	<i>Dielectric Characterization</i>	55
3.3.3	<i>Performance of BLSF Materials as CDRA</i>	66
3.4	Conclusions	70
4	GENERAL CONCLUSIONS	71
	BIBLIOGRAPHY	73
	APPENDIX	88
	APPENDIX A–ATOMIC POSITIONS AND FACTORS OCCUPATION THE SAMPLES BFTO, BGFTO AND BNFTO	88

APPENDIX B–DISTRIBUTION OF THE NORMAL MODES TO BFTO	
PHASE	89
APPENDIX C–LIST OF PAPERS AND ABSTRACTS RELATED TO	
THIS THESIS	90

1 INTRODUCTION

“It is only through science and art
that civilization is of value.”

Henri Poincaré

This thesis compiles the work developed during the doctoral period at the Universidade Federal do Ceará. It presents the results of the synthesis and characterization of a ceramic material belonging to the perovskite group, called Bismuth Layer-Structured Ferroelectric (BLSF), popularly known as the Aurivillius phase.

The structural, morphological, electrical, and magnetic characterizations, as well as its application in microwave and radiofrequency regimes were studied. Thus, this chapter is dedicated to understanding of the importance of developing and improving new materials to satisfy the aspirations and demands of technological applications. In addition, it justifies the motivation of this thesis, list the main goal, present the summary of dielectric ceramics physics, and explains the structure of this thesis.

1.1 Motivation

The ceramics materials should follow the trend of development of industry and modern technology. Currently, there is a well-established nomenclature to differentiate advanced ceramics from other so-called classic ceramics (HEIMANN, 2010). Among advanced ceramics, the subclass of electronic ceramics stands out due to their characteristic such as high-temperature stability, durability, and low thermal expansion properties. Today, they are used in a wide range of end-use industries such as home appliances, medical devices, power grids, mobile phone applications, radars, and military technology (CALLISTER; RETHWISCH, 2018; HEIMANN, 2010).

The high demand and the great current technological development provide a very lucrative market. Recently, the Global Electronics Ceramics & Electrical Ceramics Market size was estimated at USD 10.94 Billion in 2020 and expected to reach USD 11.52 billion in 2021, at a Compound Annual Growth Rate (CAGR) 5.60% to reach USD 15.18 billion by 2026 (MCKENZIE, 2021). For example, approximately four trillion of multi-layer ceramic capacitors (MLCC) are used per year in electronics devices, from smartphones to automobiles (SUZUKI *et al.*, 2021). Already on a modern smartphone, notebook, tablet, and LED TVs has

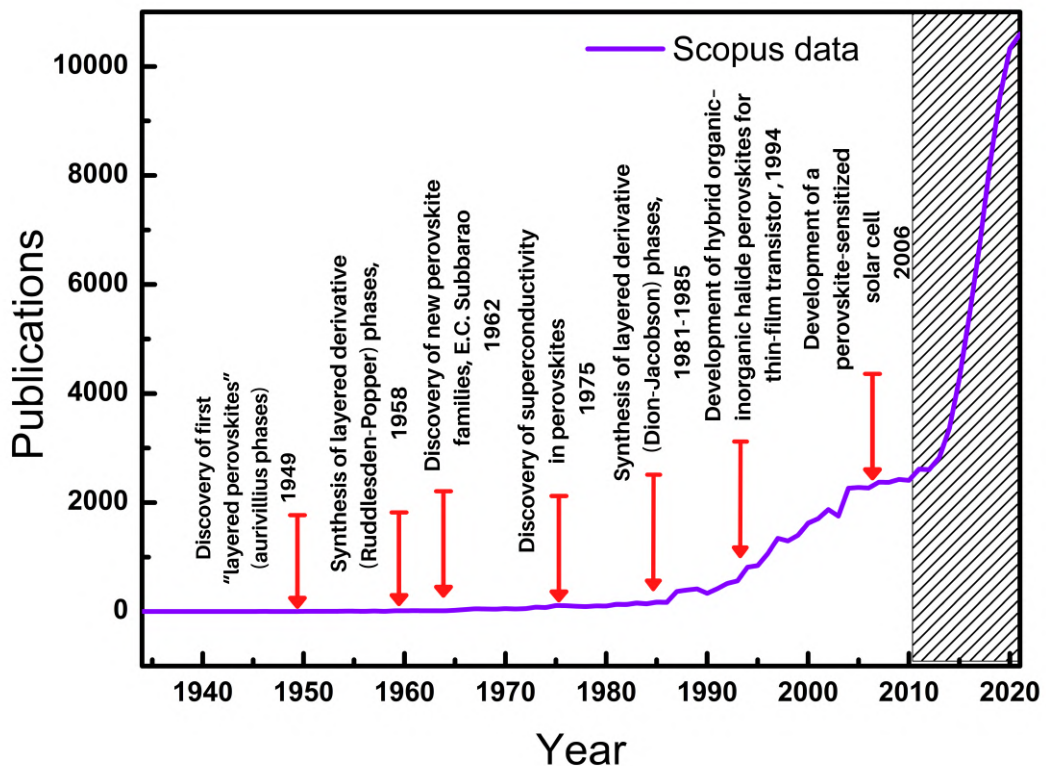
about 1000 of these capacitors (HONG *et al.*, 2019). Considering the trend towards electric vehicles, with electronic controls and automotive systems, that number could reach ten thousand (RAVANAMMA *et al.*, 2021). Today, there are an estimated 2.5 billion smartphone users worldwide, roughly a third of the planet's inhabitants. And by 2025, according to the Ericsson company's in the new edition of the "Mobility Report" (ERICSSON, 2021) estimates, around 7.7 billion smartphones will be active in the world in five years, or practically the number of inhabitants estimated for the world population in 2021. Categorically, the document highlights the way in which the coronavirus pandemic accelerated the transition from physical to virtual and cites the development of the 5G network as a result.

Due to the high demand for transmission technology service compatible with the large number of applications and the very high increase in cell phone, television and computer users, new materials applied to antennas need to accompany this evolution from 3G to 5G. It is expected that 5G technology will initially be divided into three frequency bands: the lower frequency band (below 1 GHz), the high frequency band (1–6 GHz), and the very high frequency band (greater than 6 GHz). (ULLAH *et al.*, 2021). Probably, this evolution should trigger new businesses and new markets, such as news on the internet of things (IoTs), electric cars and other industrial devices with new generation technologies (DEDECKER; GRANCINI, 2020).

A class of materials with multiple functionalities and applications has been effectively contributing to meet this great demand. First discovered in 1839 by Gustav Rose and named after the Russian mineralogist L. A. Perovski, the perovskites have been extensively studied (KATZ, 2020). These materials have a wide range of properties and many potential applications. Within the perovskite group there is a subclass known in the literature as layered perovskites. Layered perovskites can be divided into various types according to the structural feature of separated perovskite-like sheets. Figure 1 shows the approximate number of annual publications on the perovskite structure over the past eighty years. Data were taken from the Scopus database (searching for "perovskite", "perovskite structure" AND "perovskite layer-structured"). The red arrows indicate a simplified timeline containing the most important contributions regarding layered perovskites. The first works are more focused on knowing the structural relationships, stability properties and possible families of these structures (AURIVILLIUS, 1949; RUDDLESDEN; POPPER, 1957; RUDDLESDEN; POPPER, 1958; DION *et al.*, 1981; JACOBSON *et al.*, 1985). After the improvement of the production of these materials, due to the instrumental advance, new routes of synthesis and training of specialized personnel,

the applications grew enormously (see hatched area). Starting from hybrid perovskites for applications in transistors (MITZI *et al.*, 1994) to the construction of solar cells (KOJIMA *et al.*, 2006). Many phases related to the perovskite group are modular in nature, being built from layers of a parent perovskite structure interleaved with other structures. These phases are able to accommodate composition change, by changing the thickness of the perovskite units or the inter-layer species.

Figure 1 – Approximate number of annual publications on the perovskite structure over the past eighty years. Data were taken from the Scopus database (searching for “perovskite”, “perovskite structure” AND “perovskite layer-structured”). The red arrows indicate a simplified timeline containing the most important contributions regarding layered perovskites.



Source: Elaborated by the author.

Here, attention is paid to BLSF materials, which even after more than seventy years of its first appearance reported by B. Aurivillius (AURIVILLIUS, 1949) continue to attract the interest of the scientific community, being developed and rapidly improved due to its great structural versatility and multifunctionality arising from its electrical, magnetic, optical, and mechanical properties. Nowadays, in certain way that solid-state devices are now indispensable part of any modern consumer electronics.

1.2 Bismuth Layer-Structured Ferroelectric Materials

Over the past few years, BLSF have attracted great attention due to their interesting physical properties and broad potential of applications, such as in mobile phone applications (5G), military technology, medical devices, clean energy, water treatment, radar, sensors, electronic devices, memory storage, antennas, and solar cells (LIU *et al.*, 2020; BADGE; DESHPANDE, 2020; WENDARI *et al.*, 2020; PATRI *et al.*, 2020; DING *et al.*, 2020; LONG *et al.*, 2020; LI *et al.*, 2020; JIANG *et al.*, 2020; GUO *et al.*, 2020; GAO *et al.*, 2020). Figure 2 shows a series of the main applications of the materials today.

Figure 2 – Applications for Layered perovskites.



Source: Elaborated by the author.

Generally, BLSF are presented in the form $(\text{Bi}_2\text{O}_2)^{2+} [\text{A}_{m-1}\text{B}_m\text{O}_{3m+1}]^{2-}$, in which site A can be mono, di or trivalent cations (or a combination of these). Site B generally holds tetravalent, pentavalent, and hexavalent cations, similar ions or combinations (ANDO *et al.*, 2002; CHU *et al.*, 1996; SCOTT *et al.*, 1996). The subscript m informs the number of perovskite layers $[\text{A}_{m-1}\text{B}_m\text{O}_{3m+1}]$ intercalated by $(\text{Bi}_2\text{O}_2)^{2+}$ layers (LOMANOVA *et al.*, 2006;

LOMANOVA *et al.*, 2012). When the modular components are ordered, regular homologous series of phases occur. Commonly, as with the other structures belonging to layered perovskites, such as Ruddlesden–Popper and Dion–Jacobson phases, the symmetry of mixed cation materials is often lower than that implied by the idealised structures, due to distortions of the metal–oxygen octahedra in the perovskite slabs and alterations in the cation arrangements in the inter-perovskite layers. Structures are often given similar but different space groups. Examples of layered bismuth compounds, with different m are shown in Table 1.

Table 1 – Examples of Aurivillius Phases with different layers.

Phase	Space group	Structure*	Perovskite layer	Reference
Bi_2WO_6	P2 ₁ ab (29)	orthorhombic	$m = 1$	(DJANI <i>et al.</i> , 2014)
$\text{SrBi}_2\text{Ta}_2\text{O}_9$	A2 ₁ am (36)	orthorhombic	$m = 2$	(SWAIN <i>et al.</i> , 2015)
$\text{Bi}_4\text{Ti}_3\text{O}_{12}$	Aba2 (41)	orthorhombic	$m = 3$	(LIU <i>et al.</i> , 2021)
$\text{Bi}_5\text{Ti}_3\text{FeO}_{15}$	A2 ₁ am (36)	orthorhombic	$m = 4$	(SILVA <i>et al.</i> , 2020)
$\text{Ca}_2\text{Bi}_4\text{Ti}_5\text{O}_{18}$	B2cb (41)	orthorhombic	$m = 5$	(WANG <i>et al.</i> , 2021)

* Room temperature.

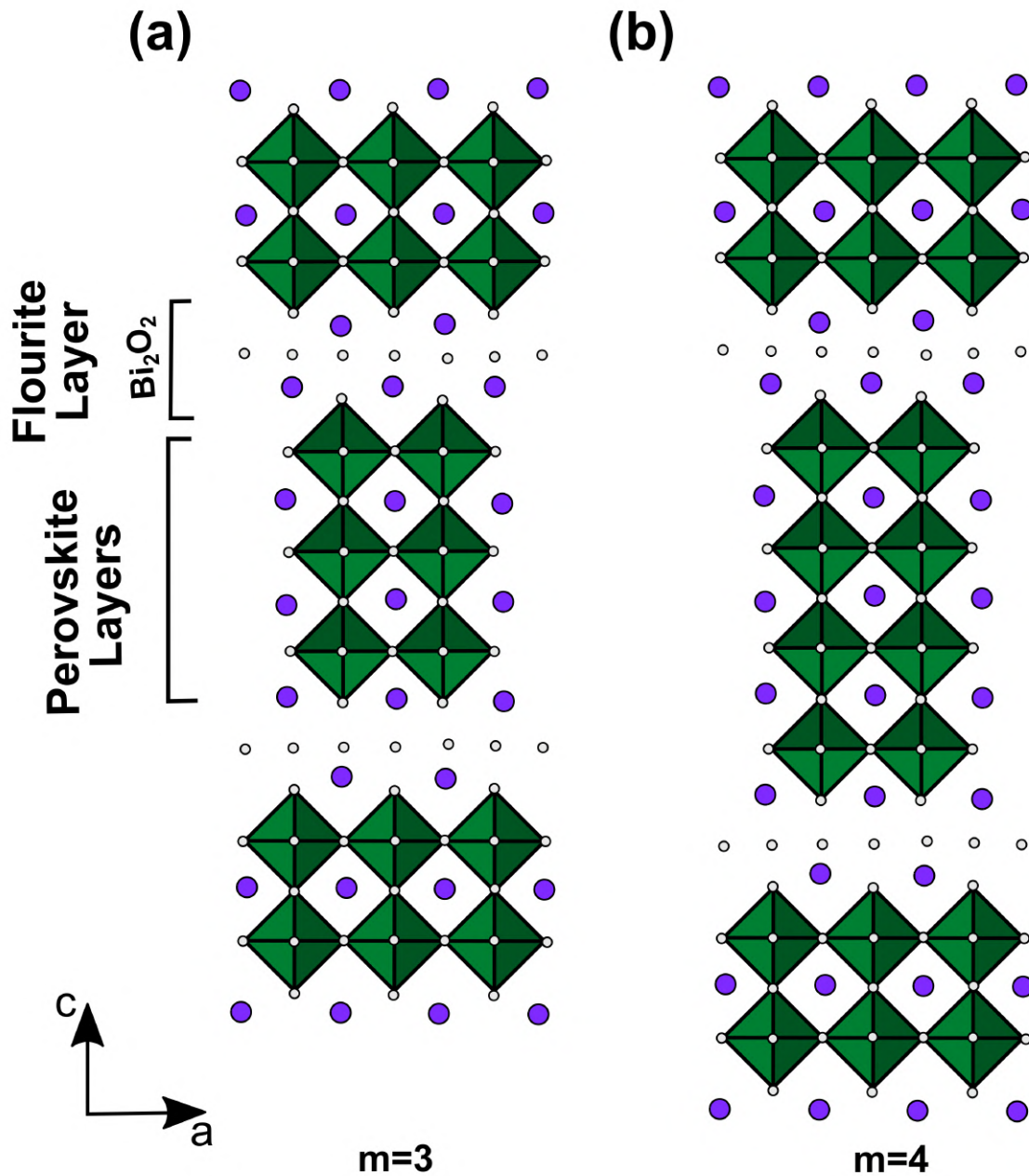
Source: Elaborated by the author.

Although $\text{Ca}_2\text{Nb}_2\text{Bi}_2\text{O}_9$ was the first BLSF studied in depth in the literature (AURIVILLIUS, 1949), the best known member of this series is the ferroelectric $\text{Bi}_4\text{Ti}_3\text{O}_{12}$, in which $m = 3$ (SUBBARAO, 1962). When combining the ferroelectric phase $\text{Bi}_4\text{Ti}_3\text{O}_{12}$ with the long-range magnetic one BiFeO_3 , the phase $\text{Bi}_5\text{Ti}_3\text{FeO}_{15}$ is obtained, having atoms with a lone-pair of electrons (Bi^{+3}) and a half-filled d -shell (Fe^{+3}) (KRZHIZHANOVSKAYA *et al.*, 2005).

$\text{Bi}_5\text{Ti}_3\text{FeO}_{15}$ (BFTO) is a typical member of the Aurivillius family with $m = 4$ (four perovskite-like layers per unit cell), where the cube-octahedral site A is occupied by 12 coordinated Bi^{3+} and site B is occupied by Ti/Fe octahedrally coordinated. For BFTO there are two orthorhombic phases with Fmm2 (KUBEL; SCHMID, 1992; GARCIA-GUADERRAMA *et al.*, 2005) and A2₁am (HERVOCHES *et al.*, 2002) space groups. Several works on the properties of the BFTO phase have been done in recent years. Its structural, electrical, magnetic, and optical properties have already been reported by various techniques (MOHAPATRA *et al.*, 2014; PIKULA *et al.*, 2017; LI *et al.*, 2010; DONG *et al.*, 2008). These works show that the BFTO presents ferroelectricity with Curie temperature (T_c) close to 1023 K and antiferromagnetic (Néel temperature) of approximately 80 K (HERVOCHES *et al.*, 2002; JIANG *et al.*, 2014a). In addition, some work has been carried out to develop a single-phase multiferroic, based on the BFTO phase, with strong magnetoelectric coupling at room temperature (BIRENBAUM;

EDERER, 2014; ZUO *et al.*, 2022). Figure 3 shows the idealised structures of the Aurivillius phases for $m = 3$ and $m = 4$.

Figure 3 – Idealised structures of the Aurivillius phases: (a) $m=3$ (b) $m=4$.



Source: Adapted from (TILLEY, 2016).

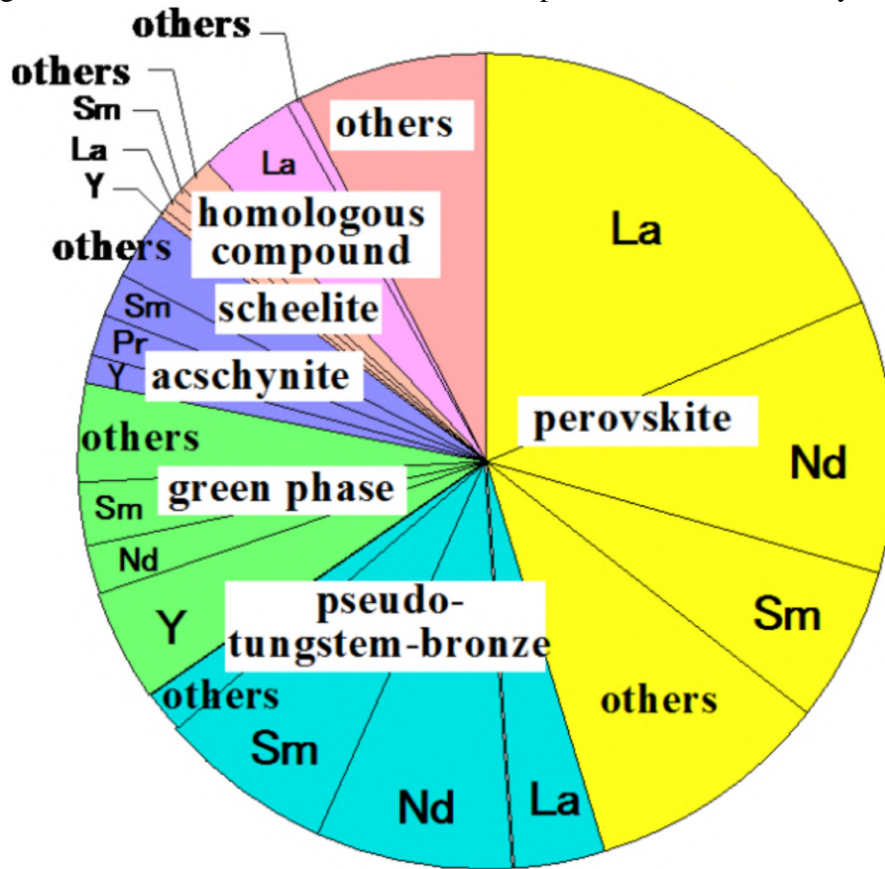
In the literature, there are several ways to implement new effects and develop improvements in certain properties for BLSF. For example, effects arising directly from different forms of synthesis (FARAZ *et al.*, 2015), the formation of local defects in the structural arrangement (UNIYAL; YADAV, 2009; THAKUR *et al.*, 2016), a change in the number of perovskite m

layers (LOMANOVA *et al.*, 2012; JARTYCH *et al.*, 2013), a doping at sites A and B (CHEN *et al.*, 2016; CHEN *et al.*, 2017; CHEN *et al.*, 2018; KUMARI *et al.*, 2018; YIN *et al.*, 2016), and even a total or partial replacement of elements in the A and/or B site (CHEN *et al.*, 2006; MOHAPATRA *et al.*, 2016; REHMAN *et al.*, 2016).

Among the possibilities mentioned above, the last one presents itself as a very successful method. The partial and/or total replacement of elements at sites A and B in the perovskite layers present in the BFTO ceramic phase is capable of generating a wide variety of isostructural phases, and this mechanism has drawn the attention of researchers, in particular, to studies in which the replacement of a certain site in the perovskite layer is an element of the so-called rare earth group. For example, a study carried out by Ohsato (OHSATO, 2016) made a quantitative survey of works that mention the use and/or development of dielectric materials, especially with regard to microwave technology. In this study, it is possible to verify that about 3000 compounds and 1600 references, a considerable amount (about 45%) are of the perovskite-type. The second largest group of compounds are the pseudotungsten-bronze solid solutions, also related to perovskite compounds (about 21%) and sizeable amount (46%) includes rare earth ions. This information and the other structures mentioned in the research are shown in Figure 4.

In this work, the elements Nd and Gd are chosen to implement the modifications in the $\text{Bi}_5\text{FeTi}_3\text{O}_{15}$ (BFTO) phase. The variations, after the replacement of Bi^{3+} , by Nd^{3+} and Gd^{3+} , generate two new phases $\text{Bi}_3\text{Nd}_2\text{FeTi}_3\text{O}_{15}$ (BNFTO) and $\text{Bi}_3\text{Gd}_2\text{FeTi}_3\text{O}_{15}$ (BGFTO). The strategy of replacing bismuth ions present in the perovskite layers with lanthanides originates from several works with the famous BiFeO_3 and the bismuth titanate $\text{Bi}_4\text{Ti}_3\text{O}_{12}$. Some limitations of these phases, such as the low electrical resistance and current loss due to the volatilization of bismuth at the time of synthesis, in addition to the interest in implementing multiferroic properties at room temperature, made the specialists converge on the use of rare earth elements to modify these phases. Modifications to the A or B sites of these phases can result in polarizable constituents in the crystalline structure. These include cation displacements, octahedral distortions and tilting as well as the defect-related structural disorders and inhomogeneity. Therefore, it is expected that the BNFTO and BGFTO phases, when compared to the reference phase, the BFTO, present several properties that can serve the development of new electronic devices or even improve technologies already consolidated. For the purposes of this work, among the properties mentioned, the dielectric ones will be of fundamental importance.

Figure 4 – Ratio of microwave dielectric compounds with different crystal structures.



Source: (OHSATO, 2016)

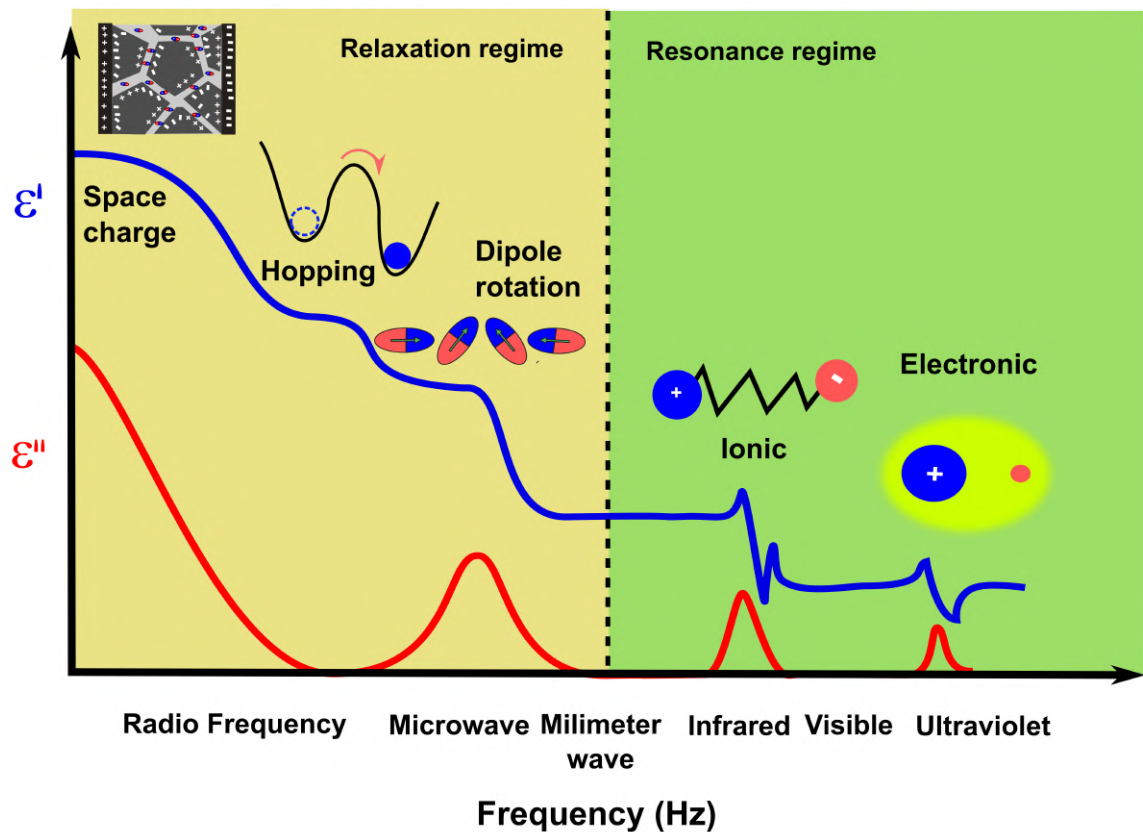
1.3 Summary of Dielectric Ceramics Physics and Microwave Applications

The relative permittivity is the basic parameter describing a dielectric material. In a static electric field, all the various contributions will be important, and both polarisability and relative permittivity will arise from electrons, ions, dipoles, defects and surfaces (CHEN *et al.*, 2004). However, in a variable electric field regime, the permittivity is a function of the field frequency and temperature (apart from the dependence of other parameters such as pressure, etc.) which result is a complex formulation ($\epsilon^* = \epsilon' - i\epsilon''$), in which ϵ' is called the dielectric constant and ϵ'' the loss factor.

The dependence of ϵ' and ϵ'' on the field frequency is represented schematically in Figure 5 for a dielectric medium that exhibits all types of polarization. In short, it is possible to divide all the phenomena present along the frequency range, into relaxations and resonances. Basically, relaxations inform how the mobility of charge carriers and dipoles is taking place as a function of the applied field, whereas resonances are regimes in which the physical system responds with frequencies very close to the external field. At each direction reversal of field,

the charge carriers attempt to reorient with the field, as illustrated Figure 5 (see inset), in a process requiring some finite time. All polarization type, some minimum reorientation time exists that depends on the ease with which the particular charge carriers are capable to reorganize. This minimum reorientation time is denominated relaxation time. The relaxation time is an important parameter and is directly related to resistive and capacitive activities of electronic devices (PANDIT *et al.*, 2019).

Figure 5 – The frequency dependence of the real and imaginary parts of the dielectric constant in the presence of Space charge, hopping, dipole rotation, ionic, and electronic polarization mechanisms.



Source: Elaborated by the author.

In engineering applications of dielectrics in electronic devices, the interest is to minimize ϵ'' for a given ϵ' . The relative magnitude of ϵ'' with respect to ϵ' is defined by a quantity, $\tan \delta$, called the loss tangent (or loss factor), as $\tan \delta = \frac{\epsilon''}{\epsilon'}$, which is, essentially, the quantitative representation of the energy dissipation in the dielectric in an alternating electric field. In practical terms, these two parameters will specify the vital circuit elements for many electronic purposes, from simple miniaturization, quality factor, time delay to thermal stability, operation band, etc. Continuing the summary and objectives of this work, consider the specific

case: dielectric resonator antennas (DRA).

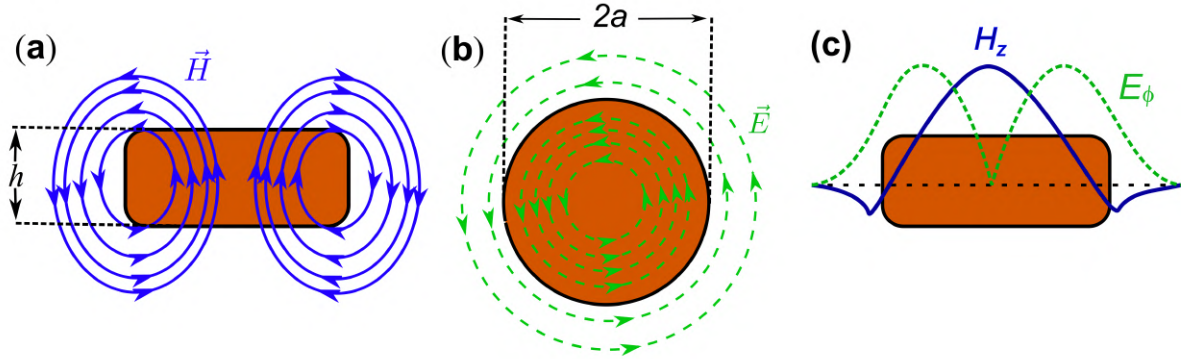
1.3.1 Dielectric Resonator Antenna

According to Members of the Antennas and Waveguides Committee of the IEEE Antennas and Propagation Group, an antenna is a means for radiating and receiving radio waves (MONEBHURRUN, 2019). Within the diversity found for these devices are the so-called DRA. Some works on this topic cite Robert Richtmyer (RICHTMYER, 1939) work as the initial step that adopted the concept of a dielectric material with useful properties as a dielectric resonator (LONG *et al.*, 1983; MCALLISTER *et al.*, 1983; MCALLISTER; LONG, 1984; KISHK *et al.*, 1989). Since then, various front-end antenna solutions relying on monopoles, dipoles, and patch antennas have been proposed for RF-wave, microwave, and millimeter-wave applications (PANDEY *et al.*, 2019).

In its simplest form a DRA is a cylinder of ceramic of relative permittivity ϵ_r sufficiently high for a standing electromagnetic wave to be sustained within its volume because of reflection at the dielectric–air interface (MOULSON; HERBERT, 2003). Figure 6 shows the fields \vec{H} and \vec{E} in a microwave resonance dielectric in the simplest standing wave mode with cylindrical geometry (designer used in this thesis). In this configuration the magnetic field lines are represented in blue and the electric field in green shown in Figure 6 (a) and (b), respectively. h is the thickness and a is the radius of the ceramic device. The dimensions of the ceramic device, through the $h/2a$ ratio, are important when determining the main modes of radiation propagation (BLADEL, 1975; KOBAYASHI; KATOH, 1985).

In a cylindrical DRA, the main resonant modes are called Transverse Electric (TE) and Transverse Magnetic (TM), and hybrid modes (HEM) can also appear (MONGIA; BHARTIA, 1994). The electric and magnetic field components of the fundamental mode of a standing electromagnetic field are illustrated in Figure 6-(c) using cylindrical coordinates, with the axis z perpendicular to the plane of the sample and the origin at the center of the ceramic disk, we have the variation in E_ϕ and H_z with r at $z = 0$. Its performance can be affected by adjustable parameters inherent to the manufacturing design, such as: resonant frequency (f_0), coefficient of frequency resonant (τ_f), impedance (Z), gain (G), irradiation diagram, polarization, efficiency (η) and bandwidth (BW). These parameters, in general, are dependent on the electrical, dielectrical, and magnetic properties and their thermal stability (RAVEENDRAN *et al.*, 2019). Details on the relationships of these parameters are explored in Chapter 3.

Figure 6 – Fields in a microwave resonance dielectric in the simplest standing wave mode: (a) magnetic field; (b) electric field, (c) variation in E_ϕ and H_z with r at $z = 0$, with reference to cylindrical coordinates (the z axis is perpendicular to the plane of the disc and the origin is at the disc centre).



Source: Adapted from (MOULSON; HERBERT, 2003)

Dielectric resonators are characterized by small size, low weight, low cost, and offer a more-compact alternative to waveguide-cavity resonators, and are more amenable to printed-circuit integration (PETOSA; ITTIPIBOON, 2010). According to Keyrouz and Caratelli (KEYROUZ; CARATELLI, 2016), we can list some advantages of dielectric resonator antennas when compared to traditional metallic antennas:

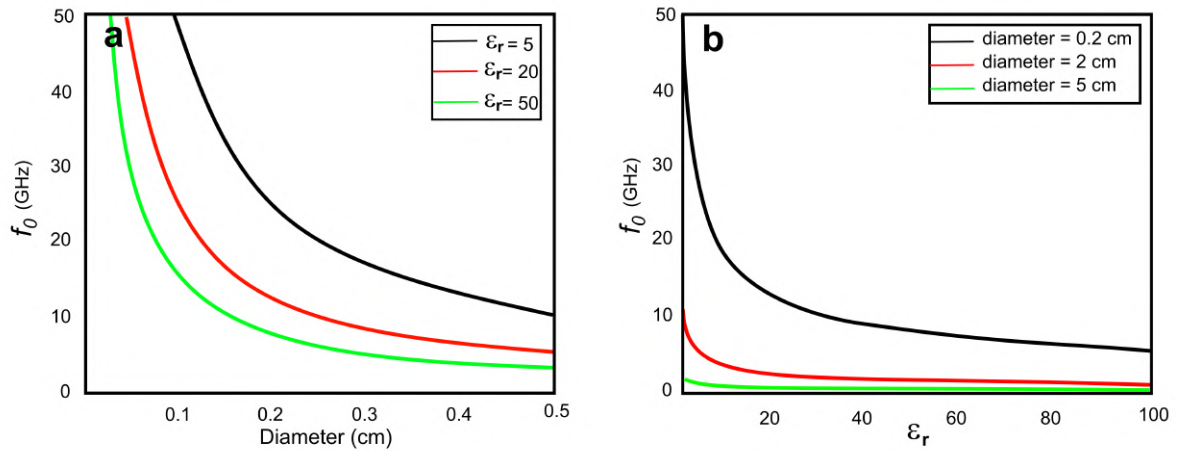
- (I) It has a great capacity for miniaturization, since its size is proportional to $\lambda_0/\sqrt{\epsilon_r\mu_r}$, with $\lambda_0 = c/f_0$ being the free-space wavelength at the resonant frequency f_0 , ϵ_r and μ_r denotes, respectively, the relative permittivity and magnetic constant of the material. In a dielectric material case, $\mu_r = 1$ and the main dimension of a DRA is proportional to $\lambda_0/\sqrt{\epsilon_r}$. In a non-magnetic dielectric medium we can write the resonance frequency as

$$f_0 \approx \frac{c}{D\sqrt{\epsilon_r}}. \quad (1.1)$$

To illustrate this relationship of dependence between these parameters, Kamutzki et al. (KAMUTZKI *et al.*, 2021) presents through Figure 7 the resonant frequencies of a cylindrical resonator as a function of (a) the diameter of the resonator for three different ϵ_r values and (b) as a function of the resonator materials ϵ_r for three different geometries.

The resonant frequency decreases when the dielectric permittivity and diameter increases. According to the literature, the possibility of building very small antennas using dielectric resonators was first proposed by Sager and Tisi (SAGER; TISI, 1968).

Figure 7 – Resonant frequencies of a cylindrical resonator as a function of (a) the diameter of the resonator for three different ϵ_r values and (b) as a function of the resonator materials ϵ_r for three different geometries.



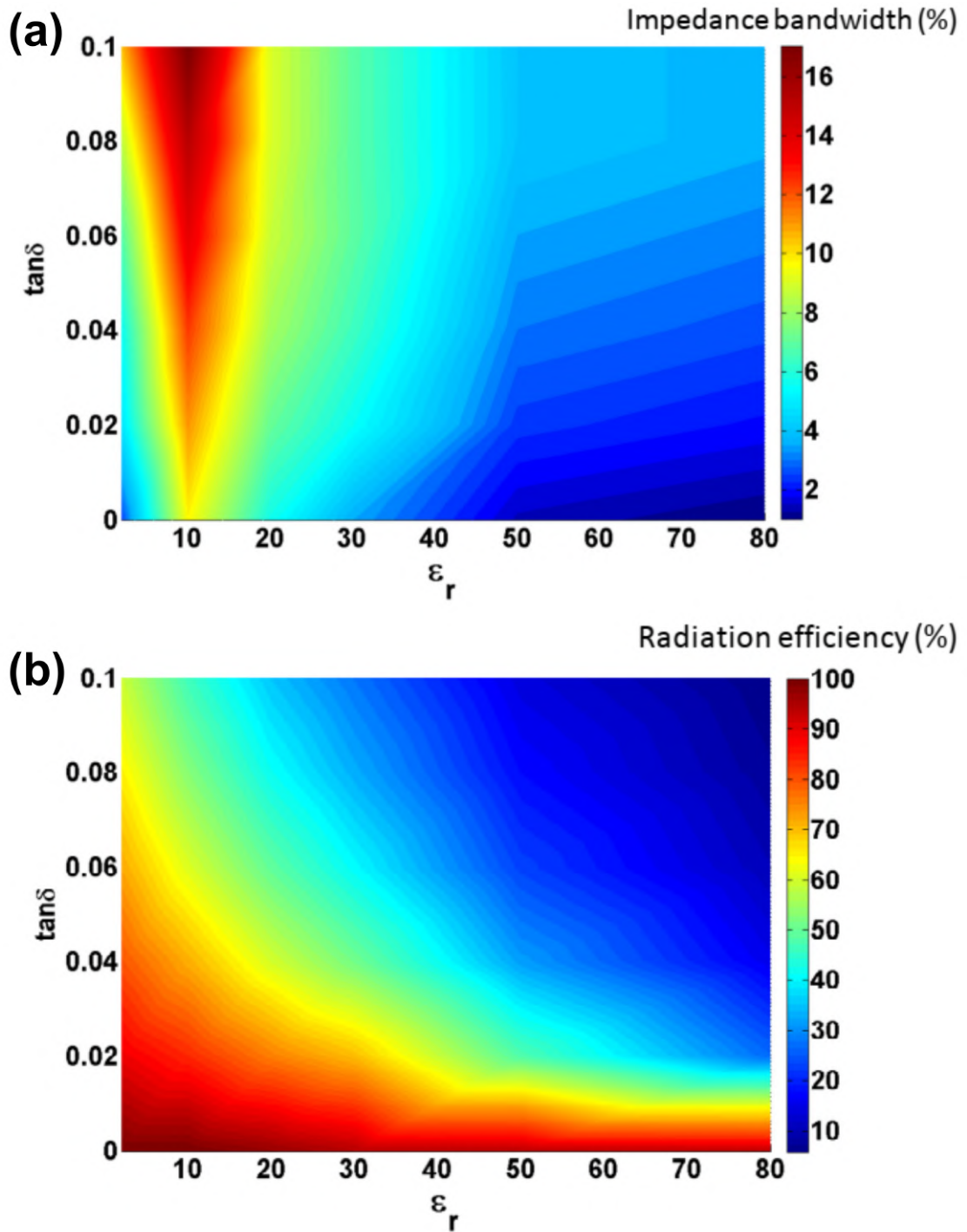
Source: (KAMUTZKI *et al.*, 2021)

- (II) DRA can be characterized by a large impedance bandwidth if the dimensions of the resonator and the material dielectric constant are chosen properly. Figure 8-(a) shows the behavior of the impedance bandwidth according to the dielectric permittivity and loss tangent. Note that the impedance bandwidth is the largest when for $\epsilon_r = 10$, regardless of the loss values. They have high radiation efficiency and low dielectric losses due to the absence of conductive materials. This feature is essential for applications in high frequency regions (30 GHz to 300 GHz). Figure 8-(b) shows the behavior of the radiation efficiency according to the dielectric permittivity and loss tangent. Note that the antenna radiation efficiency is all the more affected by the losses as the dielectric permittivity increase. For low dielectric permittivity, even in case of a high losses material, the radiation efficiency remains higher than 50%.

To provide the results presented in Figure 8 (a) and (b), (HUITEMA; MONÉDIÈRE, 2012) considered simulations of a cylindrical DRA mounted on a ground plane with radius and height respectively equal to 40 mm and 45 mm and excited in its fundamental mode. The study of losses is carried out for different values of dielectric permittivity.

- (III) It can be excited using different techniques which is helpful in different applications and for array integration (Coaxial probe excitation, Microstrip feeding line and coplanar waveguide, Aperture coupling, etc) (SOREN; TAMBOLI, 2022). The parameters of performance as gain, bandwidth, and polarization characteristics can be easily controlled using different design techniques (PANDEY; PATHAK, 2022).

Figure 8 – (a) Impedance bandwidth according to the dielectric permittivity and loss tangent and (b) Radiation efficiency according to the dielectric permittivity and loss tangent.



Source: (HUITEMA; MONÉDIÈRE, 2012)

There are a few disadvantages of DRA as well when compared with other commonly used antenna types, especially the mass produced microstrip patch antennas. The disadvantages include (BRAUN *et al.*, 2017):

- (I) The fabrication of DRA is more complex (in some cases where the use of a simple mold is

not possible) as they need to be machined (mostly) from hard ceramic and therefore the fabrication costs are higher. In this case, can say that its reproducibility on a large scale becomes difficult (BASILE *et al.*, 2020).

- (II) The DRA are 3D structures prepared separately which then needs to be glued or placed with in the rest of the circuitry. This makes it more complex and prone to fabrication errors. Dependence on density and porosity control in the manufacturing process (WU *et al.*, 2022).

One of the outstanding aspects of DRA is their wide range of applications with respect to the frequency bands originating from the microwave spectrum (SABBAN, 2016). Microwave dielectric ceramics are being developed for a variety of applications from communication systems, through molecular spectroscopy, astronomical observations, to automotive radar and dense 5G communications (KUI, 2021).

In order to distinguish different bands of this spectrum, a good selectivity and stability during the operation of the electronic device is necessary (CHEN *et al.*, 2004). Stability and selectivity are indispensable to guarantee that signals are confined to narrowly defined frequency bands and to prevent the interference with unwanted signals that could hamper with satisfactory system performance (MOULSON; HERBERT, 2003). In a simplified way, the parameters associated with these two antenna characteristics are BW and τ_f . The bandwidth of an antenna is

$$BW = \frac{s-1}{Q\sqrt{s}} = \frac{\Delta f}{f_0} \quad (1.2)$$

in which s is the maximum acceptable voltage standing wave ratio (VSWR), Q (inverse of dielectric loss) is the quality factor, Δf the absolute bandwidth, and f_0 is the resonant frequency.

As the temperature changes, the resonant frequency will also change, since f_0 is a function of ϵ_r and the dimensions of the dielectric (see Equation 1.1). The thermal stability of the operating frequency can be calculated using the equation

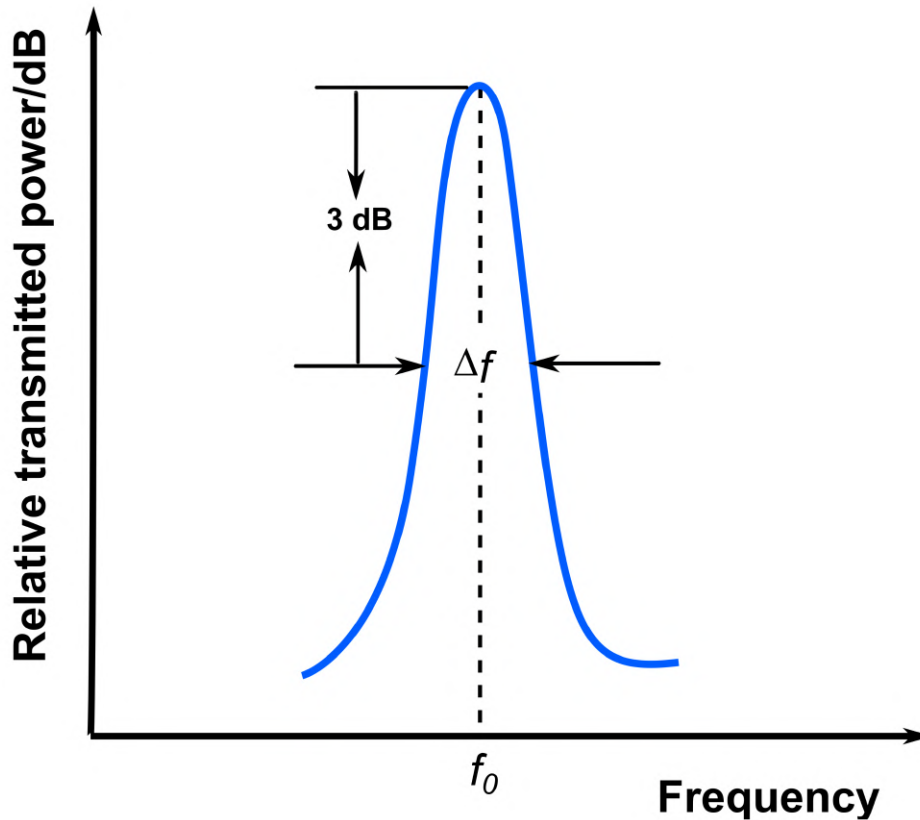
$$\frac{1}{f_0} \frac{\partial f_0}{\partial T} = -\frac{1}{D} \frac{\partial D}{\partial T} - \frac{1}{2\epsilon_r} \frac{\partial \epsilon_r}{\partial T} \quad (1.3)$$

in which $\frac{1}{f_0} \frac{\partial f_0}{\partial T} = \tau_f$ is the temperature coefficient of resonance frequency, $\frac{1}{D} \frac{\partial D}{\partial T}$ is the temperature coefficient of linear expansion, $\frac{1}{\epsilon_r} \frac{\partial \epsilon_r}{\partial T}$ is the temperature coefficient of permittivity.

Therefore, the BW is required for achieving prominent frequency selectivity and stability in microwave transmitter components and the small temperature coefficient of the resonant frequency ($\tau_f \sim 0$) ensures the stability of the microwave components at different

working temperatures (TSENG *et al.*, 2006). Figure 9 shows the frequency response of a DRA coupled to a microwave circuit.

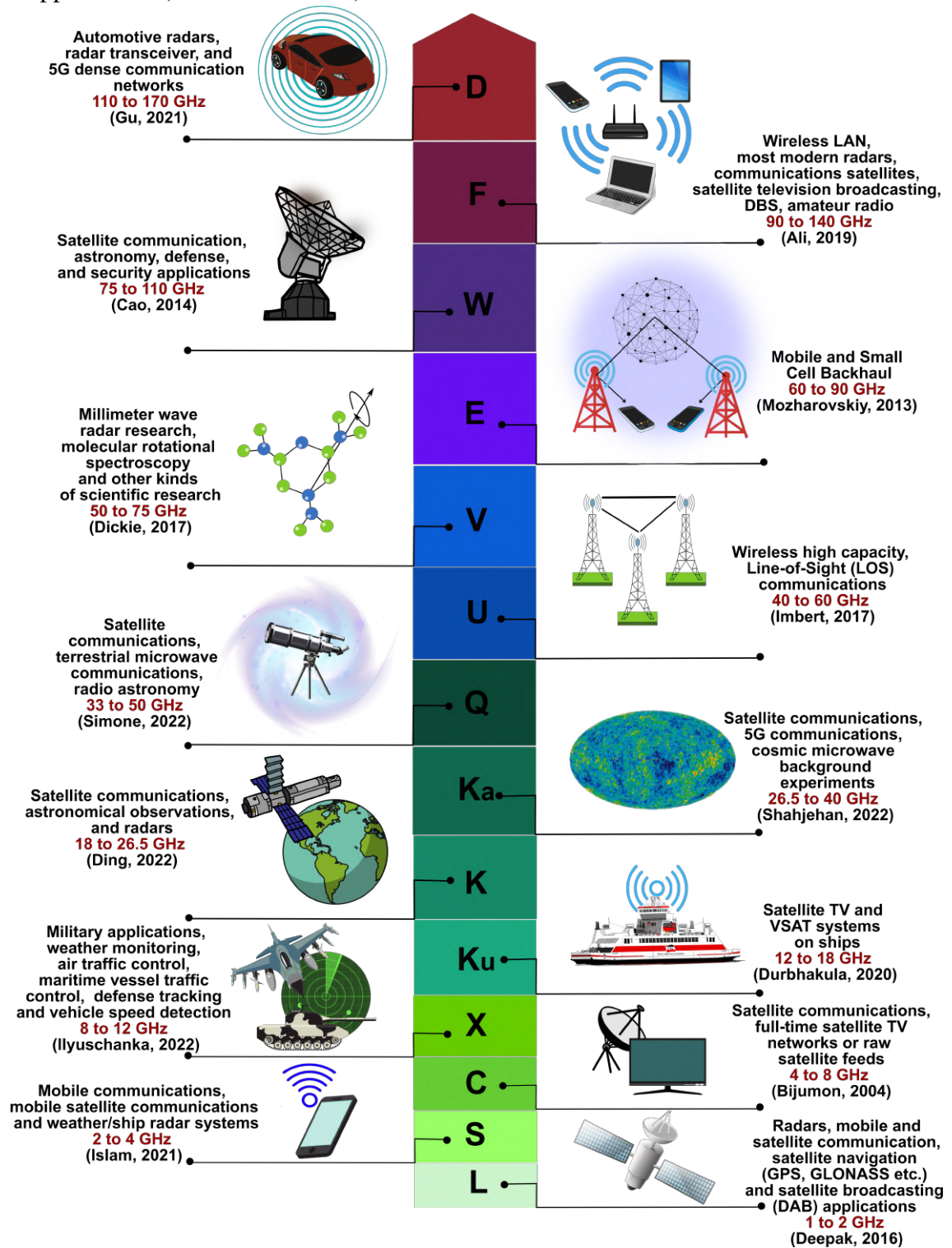
Figure 9 – Frequency response of a microwave resonator.



Source: Adapted from (MOULSON; HERBERT, 2003).

Figure 10 details microwave frequency bands from L to D (IEEE radar band designations (BRUDER *et al.*, 2003)), designation frequency range, and typical uses for various applications (PRASATH *et al.*, 2016; ISLAM *et al.*, 2021; BIJUMON; SEBASTIAN, 2004; DURBHAKULA; AOUTHU, 2020; DING *et al.*, 2022; SHAHJEHAN *et al.*, 2022; SIMONE *et al.*, 2022; IMBERT *et al.*, 2017; DICKIE *et al.*, 2017; MOZHAROVSKIY *et al.*, 2013; CAO *et al.*, 2014; ALI *et al.*, 2019; GU; BAI, 2021; ULLAH *et al.*, 2021; SABBAN, 2017; RAI *et al.*, 2022).

Figure 10 – The microwave portion of the electromagnetic spectrum and its constituent bands and applications (from L to D band).



Source: Elaborated by the author.

1.4 Main Goal

The goal is to provide significant advances in the knowledge of the BLSF materials, in particular the $\text{Bi}_3\text{R}_2\text{Ti}_3\text{FeO}_{15}$ phases, with $\text{R} = \text{Bi}, \text{Gd}, \text{and Nd}$, and to investigate its structural, vibrational and magnetic properties. Use impedance spectroscopy (IS) to relate microstructural properties and dielectric response in the radiofrequency/microwave regime as a function of temperature. In an innovative character, these materials were tested as ceramic capacitors and the CDRA performance parameters are contrasted in detail by experimental and simulated analysis. A comparison with previous works was made to increase the possibility of future discoveries in this area.

1.5 Structure of this thesis

This thesis contains results from three articles. Two fully published articles (Chapter 2 and Chapter 3) and one unsubmitted first draft manuscript are presented. In the introduction, there is the part in the writing process (submission). Basically, the importance of BLSF within the perovskite family is presented, through a historical overview, a brief review of its properties and its capacity for structural modification. A summary of the physical properties of dielectric ceramics, the effects arising from the application of a variable external electric field and the parameters required for application in dielectric resonator antennas.

In Chapter 2, a series of properties of these materials are analyzed. The characterization by X-ray powder diffraction, Raman spectroscopy, magnetic measurements (ZFC, FC) and Mössbauer spectroscopy is discussed. These characterizations were important to elucidate the effects arising from the replacement of Bi^{3+} ions by rare earth elements within the perovskite layers.

In Chapter 3, the BFTO, BGFTO, and BNFTO samples were analyzed through their morphology and dielectric properties in microwave and radiofrequency regime with temperature variations. It is made some comparisons of performance parameters as a ceramic capacitor and also as CDRA of these samples and some works present in the literature.

Chapter 4 presents a summary with the key findings and perspectives. The Appendix A contains some data on atomic positions and occupancy factors of the three phases. Appendix B contains the first page of each published article, book chapters, and the conference abstracts related to this thesis.

2 EFFECTS OF THE Bi^{3+} SUBSTITUTION ON THE STRUCTURAL, VIBRATIONAL, AND MAGNETIC PROPERTIES

“It doesn’t matter how beautiful your theory is, it doesn’t matter how smart you are. If it doesn’t agree with experiment, it’s wrong”.

Richard P. Feynman

2.1 Introduction

The structural, electrical, magnetic, and optical properties of $\text{Bi}_5\text{Ti}_3\text{FeO}_{15}$ (BFTO) have been investigated by numerous techniques, focusing on different aspects (MOHAPATRA *et al.*, 2014; GARCÍA-GUADERRAMA *et al.*, 2014; JARTYCH *et al.*, 2013; LI *et al.*, 2010; NAN *et al.*, 2008). These works show that the crystalline structure belongs to the $A2_1am$ space group and presents ferroelectricity with Curie temperature (T_c) close to 1023 K and an antiferromagnetic order with Néel temperature of approximately 80 K (HERVOCHES *et al.*, 2002; JIANG *et al.*, 2014a). The $P - E$ hysteresis loops of the BFTO at room temperature (MAO *et al.*, 2008), under a driven electric field of 300 kV cm^{-1} , show that this phase has a ferroelectric response with well-defined remnant polarization ($2P_r \sim 11.8 \mu \text{ C cm}^{-2}$) and coercive field ($2E_c \sim 270 \text{ kV cm}^{-1}$).

Investigations on the magnetism of BFTO, however, are still controversial, even for the same form ceramics synthesized by distinct fabrication routes (DONG *et al.*, 2008; WU *et al.*, 2012; ZHAO *et al.*, 2014; PIKULA *et al.*, 2017). The superparamagnetic behavior with dominant antiferromagnetic at low temperature (5 K) was reported in (DONG *et al.*, 2008). On the other hand, measurements revealed the paramagnetic behavior of the BFTO compounds down to 3.7 K (PIKULA *et al.*, 2017). At room temperature, the result of magnetic measurement indicated the weak ferromagnetism order (WU *et al.*, 2012) and Zhao *et al.* (ZHAO *et al.*, 2014) suggest the spin canting of magnetic-ion-based nanodomains via the Dzyaloshinskii–Moriya interaction might yield a robust magneto-electric coupling of $\sim 400 \text{ mV/Oe.cm}$. It is worth mentioning here the findings in (JARTYCH *et al.*, 2013; MAZUREK *et al.*, 2012; JARTYCH *et al.*, 2010), who have reported the properties of the magnetic and hyperfine interactions of the series of multiferroic $\text{Bi}_{m+1}\text{Ti}_3\text{Fe}_{m-3}\text{O}_{3m+3}$ Aurivillius compounds with $m = 4 - 8$. In these

works, the authors have investigated the samples by using ^{57}Fe Mössbauer spectroscopy, and vibrating sample magnetometry, concluding that, for $m = 4$, we have the BFTO phase, at room temperature, where the compound has paramagnetic ordering.

Due to the aforementioned results, the BFTO phase has already been considered a promising material. Nevertheless, several studies considering the doping of the BFTO phase, with partial or total substitution of elements in the sites A and B of perovskite layers, presented interesting new results. For instance, Huang et al. (HUANG *et al.*, 2011) suggest that the T_c decreases with increasing the doping of Na and Ce ions in $\text{Bi}_{5-x}\text{Na}_{x/2}\text{Ce}_{x/2}\text{Ti}_3\text{FeO}_{15}$ ($x = 0, 0.05$, and 0.10 – 0.60). The magnetic behavior of polycrystalline $\text{Bi}_5\text{Ti}_3\text{Cr}_x\text{Fe}_{1-x}\text{O}_{15}$ (for $x = 0, 0.05$, and 0.1 – 1.0) is an example where doping occurs at the B site (with a Fe/Cr ion ratio) (SUN *et al.*, 2016). The ferromagnetism in the Ni-doped BFTO Aurivillius phase, in turn, has been interpreted by Xiao et al. (XIAO *et al.*, 2015) as the aggregation of magnetic ions at the inner octahedra and spin canting of magnetic-ion-based sublattices.

In this chapter, Nd^{3+} and Gd^{3+} ions are selected as potential candidates to improve the already known properties of the BFTO, studying the effects of partial replacement of bismuth at the A -site of the perovskite layers systemically. Diverse characterization techniques were employed to investigate the $\text{Bi}_3\text{R}_2\text{Ti}_3\text{FeO}_{15}$ phase, with $\text{R} = \text{Gd}$, and Nd , identified hereinafter as BGFTO and BNFTO, thus obtaining fundamental information on the structural, vibrational, and magnetic properties of these materials.

2.2 Experimental Methods

The synthesis of the BFTO, $\text{Bi}_3\text{Gd}_2\text{Ti}_3\text{FeO}_{15}$ (BGFTO), and $\text{Bi}_3\text{Nd}_2\text{Ti}_3\text{FeO}_{15}$ (BNFTO) was performed by a conventional solid-state reaction method. The starting materials (Bi_2O_3 , Fe_2O_3 , TiO_2 , Gd_2O_3 , and Nd_2O_3) with high purity (Bi_2O_3 with 99.9 and 99% for other reagents) were purchased from Sigma-Aldrich. The reagents were weighted according to the stoichiometric composition, following the reactions presented in Eqs. 2.1, 2.2, and 2.3, and manually homogenized in a mortar for 10 min. The powders were brought to the oven and calcined at 1000°C for 6 h.



On the structural characterization, diffraction patterns were obtained with a Bruker diffractometer (D8 Advance), operating at 40 kV and 40 mA, with $\text{CuK}\alpha$ radiation ($K\alpha = 1.5418 \text{ \AA}$) equipped with the LynxEye linear detector, at room temperature, with 2θ varying from 10° to 100° , with a step size of 0.02° . Rietveld refinement was performed, using Bruker AXS TOPAS program (COELHO, 2018).

The Raman spectra of BGFTO, BNFTO, and BFTO samples, measured at room temperature, were recorded in a Horiba Lab-Raman spectrometer equipped with a liquid N_2 -cooled (Charge Coupled Device (CCD)). The spectrometer slits were set for a resolution of 2 cm^{-1} . The 633-nm line of He-Ne laser was used to excite the Raman signals.

The magnetic characterization was performed with a quantum design dynacool Physical Property Measurement System (PPMS). In this case, the Zero-Field-Cooled (ZFC) and Field-Cooled (FC) magnetization curves were acquired in the temperature range of 5-300 K, under an external magnetic field of 50 Oe. From the ZFC curve, the inverse of magnetic susceptibility was also obtained. Moreover, isothermal magnetization, with maximum magnetic field $\pm 100 \text{ kOe}$ and after zero-field cooling, were measured at the selected temperatures of 5, 10, 25, 50, 100, 200, and 300 K.

Finally, Mössbauer spectra (MS) were recorded in transmission mode at 300 K (room temperature) and 12 K, using a conventional spectrometer in a constant acceleration mode, with gamma rays provided by ^{57}Co (Rh) source. The MS were analyzed using a non-linear least square routine, with Lorentzian line shape. Isomer shift values are related to $\alpha\text{-Fe}$ at 300 K.

2.3 Results and Discussion

2.3.1 Powder X-ray Diffraction

Figure 11 shows the PXRD patterns with Rietveld refinements of $\text{Bi}_3\text{R}_2\text{Ti}_3\text{FeO}_{15}$ (R = Bi, Nd, and Gd) samples. The crystalline structure of all the samples has been refined as an orthorhombic perovskite ($A2_1am$ space group, ICSD-51862) (HERVOCHES *et al.*, 2002). These results show that the samples exhibit a single-phase perovskite structure, and no secondary or impurity phases were detected.

Rietveld refinement of the PXRD patterns have confirmed that the samples crystallize in the $A2_1am$ space group, since the $Fmm2$ space group does not index some small intensity peaks close to $2\theta = 19.5^\circ, 22.2^\circ, 28.9^\circ, 38.3^\circ, \text{ and } 51.6^\circ$. The Rietveld refinement of the BFTO PXRD

pattern, using the $A2_1am$ (ICSD-51862) and $Fmm2$ (ICSD-154483) (GARCIA-GUADERRAMA *et al.*, 2005) space groups, can be seen in Figure 12, in which the above-mentioned peaks are identified with arrows. The lattice parameters, crystallite size, microstrain, density, goodness of fit (GOF), and R_{wp} are summarized in Table 2. It was observed that the peak position of BGFTO and BNFTO samples is shifted to higher angles compared to the BFTO phase. Figure 11-(b) shows the (200) and (020) peaks of BFTO, BGFTO, and BNFTO. These peaks present an evident shift towards higher angles for BGFTO and BNFTO, and an overlapping, evidencing that a and b lattice parameters have very close values and, consequently, a reduction in the orthorhombicity of these samples. This can be seen in the lattice parameters presented in Table 2.

Table 2 – Lattice parameters, density, crystallite size, microstrain, factors of the Rietveld analysis

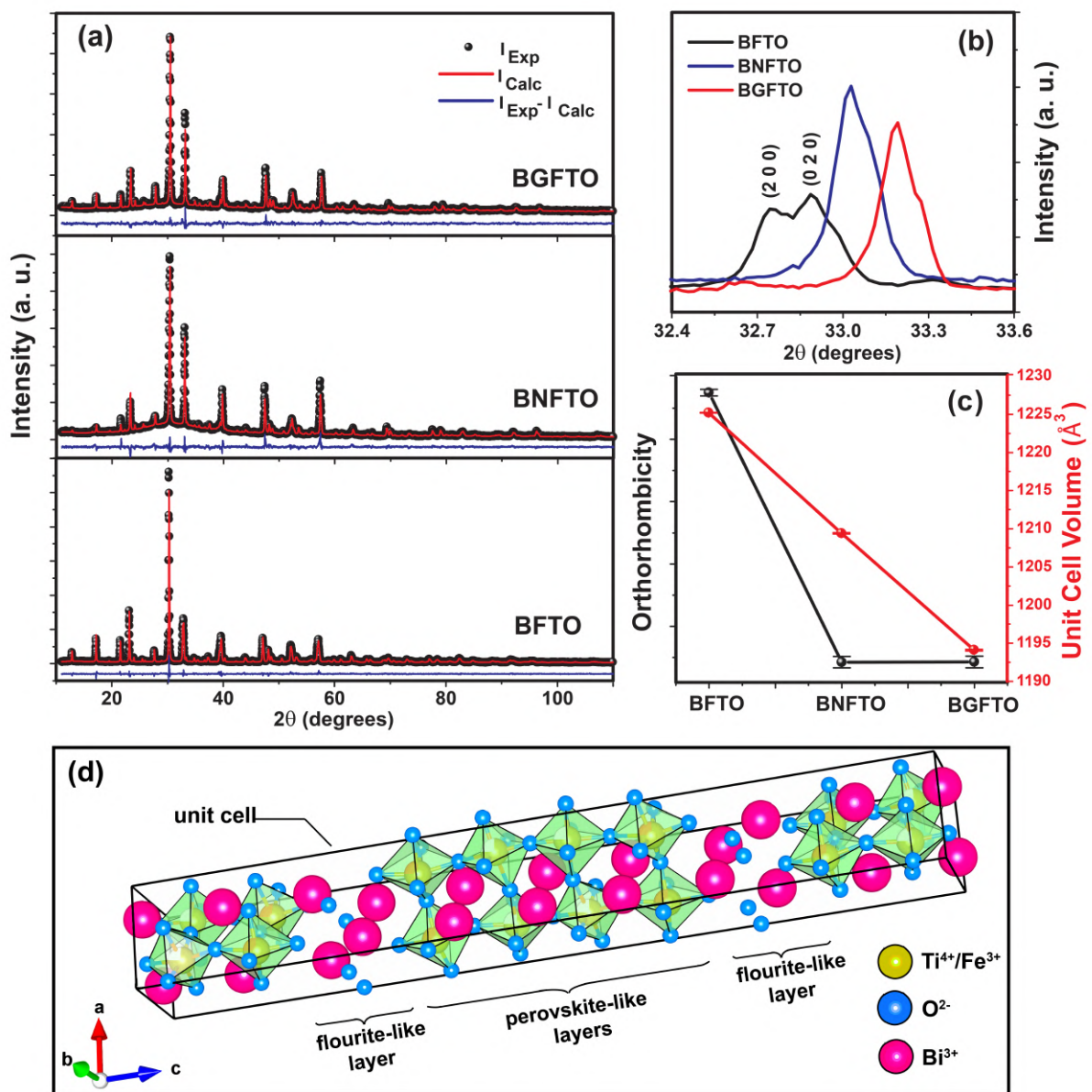
Samples	Lattice parameters (Å)	Density (g/cm ³)	L (nm)	ξ (%)	R_{wp}	GOF
BFTO	$a = 5.4655(1)$ $b = 5.4396(1)$ $c = 41.211(1)$	8.047(1)	214(5)	0.056(1)	9.54	1.30
BNFTO	$a = 5.4205(4)$ $b = 5.4182(2)$ $c = 41.177(3)$	7.443(1)	164(9)	0.053(1)	8.95	1.87
BGFTO	$a = 5.3944(4)$ $b = 5.3921(3)$ $c = 41.052(2)$	7.681(1)	186(9)	0.058(2)	7.31	1.50

Source: (SILVA *et al.*, 2020), Copyright ©2020, Springer Nature.

The lattice parameters and orthorhombicity reduction are due to the Bi^{3+} substitution by Gd^{3+} and Nd^{3+} . The crystal structure orthorhombicity $\bar{\delta} = 2(a - b)/(a + b)$ (JEON *et al.*, 2004), and unit cell volume, were plotted in Figure 11-(c) to analyze the substitution-induced structural changes in BFTO by neodymium and gadolinium ions. Compared to BFTO, the orthorhombicity and unit cell volume of the BGFTO and BNFTO phases exhibit a shrinking behavior, which can be attributed to the smaller ionic radius of Nd^{3+} (~ 0.111 nm) and Gd^{3+} (~ 0.105 nm), compared to the one of Bi^{3+} (~ 0.117 nm). This reduction in the orthorhombicity, also observed by other authors (PENG *et al.*, 2014; JEON *et al.*, 2006; LONG *et al.*, 2017; ZUO *et al.*, 2017), can be associated with an inherent mechanism of the partial substitution of bismuth ions of A -site cations, in the inner perovskite-like, by gadolinium and neodymium ions. Figure 11-(d) shows an illustration of the 3D atomic structure of the BFTO compound, obtained using the Vesta software (MOMMA; IZUMI, 2008). These structural changes were previously justified by Armstrong (ARMSTRONG; NEWNHAM, 1972), who demonstrated a dependence of this

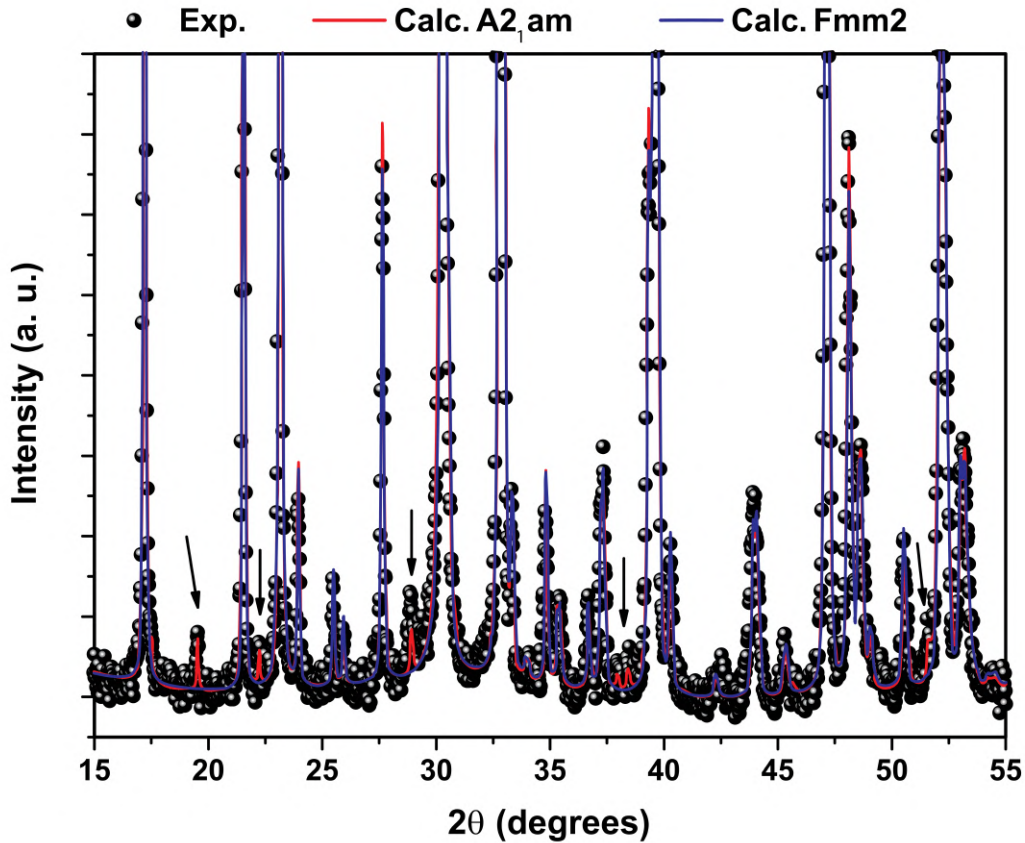
effect on the tension/compression ratio between the perovskite and fluorite layers present in the Aurivillius structure. In addition, similar studies such as the contributions of Ruixia et al. (TI *et al.*, 2015) on the $\text{Bi}_4\text{LaTi}_3\text{FeO}_{15}$ (Bi^{3+} for $\text{La}^{3+} \sim 0.103$ nm) phase, and Rehman et al. (REHMAN *et al.*, 2016) on $\text{NdBi}_4\text{Ti}_3\text{FeO}_{15}$ (Bi^{3+} for Nd^{3+}) are in very good agreement with our findings.

Figure 11 – (a) PXRD patterns of the BGFTO, BNFTO, and BFTO ceramics, at room temperature. (b) The (200) and (020) peaks of BFTO, BGFTO, and BNFTO. (c) Comparison of the orthorhombic distortion and the cell volume for the samples BGFTO, BNFTO, and BFTO. (d) Illustration of the 3D atomic structure of the $\text{Bi}_5\text{Ti}_3\text{FeO}_{15}$ compound



Source: (SILVA *et al.*, 2020), Copyright ©2020, Springer Nature.

Figure 12 – Rietveld refinement of the BFTO PXRD pattern using the $A2_1am$ (ICSD-51862) and $Fmm2$ (ICSD-154483). The peaks ($2\theta = 19.5^\circ, 22.2^\circ, 28.9^\circ, 38.3^\circ,$ and $51.6^\circ.$) are identified with arrows.



Source: (SILVA *et al.*, 2020), Copyright ©2020, Springer Nature.

The fractional atomic positions and occupancy factors of the samples are listed in Table 10 of the appendix A. From atomic positions, the structural distortion parameter (Δ), defined as the sum of the squared deviations of bond lengths from the average, can be calculated by

$$\Delta = \frac{1}{z} \sum \left[\frac{R - \bar{R}}{\bar{R}} \right]^2, \quad (2.4)$$

where z is the coordination number, R is the individual bond length, and \bar{R} is the average bond length (SHANNON, 1976; SHIMAKAWA *et al.*, 2000; ZHANG *et al.*, 2016). From the calculated values presented in Table 3 it is possible to see a reduction in the distortion of the Bi_2O_2 layer and Ti1/Fe1-O octahedral and an increase in the distortion of the Ti2/Fe2-O octahedral of the BNFTO and BGFTO samples, when compared to the BFTO sample.

Table 3 – The structural distortion parameter Δ of the samples

Samples	Bi3/RE3-O (Bi2O2-layer)	Ti1/Fe1-O (octahedral)	Ti2/Fe2-O (octahedral)
BFTO	0.00224	0.00959	0.00724
BNFTO	0.00130	0.00576	0.01841
BGFTO	0.00057	0.00638	0.01783

Source: (SILVA *et al.*, 2020), Copyright ©2020, Springer Nature.

2.3.2 Raman Spectra Analysis

The Raman spectra of BGFTO, BNFTO, and BFTO samples at room temperature are shown in Figure 13. In general, the profiles of all samples are very similar, presenting the characteristic vibrational modes of the Aurivillius phases (AGUIAR *et al.*, 2017; FERREIRA *et al.*, 2020). The dashed vertical lines indicate the vibrational modes of the BFTO. From this figure, the Raman spectra of the rare-earth substituted compounds exhibit the main phonon modes of BFTO.

According to the factor group analysis based on the method proposed by Rousseau *et al.* (ROUSSEAU *et al.*, 1981), and with the use of The Bilbao Crystallographic Server (AROYO *et al.*, 2006; AROYO *et al.*, 2006; AROYO *et al.*, 2011), it was possible to determine the number of vibrational modes in terms of the irreducible representations of the factor group. The group-theory analysis predicts a number of 141 zone-center optical modes for BFTO, BGFTO, and BNFTO with $A_{21}am$ (C_{2v}^{12}) orthorhombic symmetry. It is difficult to identify each phonon due to the mode overlapping and its weak intensity. The details of the phonon distribution for the BFTO phase are shown in Appendix B and it is in agreement with the literature (GRAVES *et al.*, 1995; JIANG *et al.*, 2014b; ARANDA *et al.*, 2018). By fitting the experimental spectra with a set of Lorentzian profiles (see Figure 13-(c)-(e)), it was possible to identify 21 Raman bands for BFTO and 18 for both BGFTO and BNFTO.

The study of the Raman modes for the BFTO phase had been previously reported (ARANDA *et al.*, 2018). The modes in the vibrational spectra below 200 cm^{-1} can be attributed to the A-site cations (Bi^{3+}), while the high-frequency modes (above 200 cm^{-1}) come from the bending, torsion, and stretching of the octahedra BO_6 . The classification of the observed vibrational modes for all samples is shown in Table 4. The modes ν_1 , ν_2 , and ν_3 , shown in Figure 13-(b), were related to the largest atomic mass and reflected the vibration of Bi^{3+} ions in $(\text{Bi}_2\text{O}_2)^{2+}$ layers (MAO *et al.*, 2012). The modes between ν_4 and ν_7 are closely related to the Bi^{3+} substitution by Gd^{3+} and Nd^{3+} at the A-sites of the perovskite layers (KOVAL *et al.*, 2018; LIU *et al.*, 2007). The peak centered around ν_8 and ν_9 was assigned to the Bi-O, Bi/Gd-O, and

Bi/Nd-O stretching in the A-site in the perovskite layers (GRAVES *et al.*, 1995; ARANDA *et al.*, 2018). The mode ν_{10} was assigned to the torsional bending of Ti/FeO₆ octahedra (JIANG *et al.*, 2014a; ARANDA *et al.*, 2018; LIU *et al.*, 2007). The vibrational modes related to the oxygen stretching along the *c*-axis (O-Ti/Fe-O stretching) were identified around ν_{11} (ARANDA *et al.*, 2018), whereas ν_{12} agrees with the O-Ti-O bending (GRAVES *et al.*, 1995; YAFENG *et al.*, 2007). The phonon bands around ν_{13} were assigned to variations of the bond distances between the Bi atoms within the Bi₂O₂ layer and the apical O atoms of the perovskite-like block (JIANG *et al.*, 2014a; JIANG *et al.*, 2014b). The modes between ν_{14} to ν_{16} were attributed to internal modes of the TiO₆ octahedra, while the former was related to Ti-O twisting effects and the other two to opposite excursion of the oxygen atoms (ARANDA *et al.*, 2018). Additionally, in the high-frequency regions, ν_{17} and ν_{18} bands were attributed to the stretching of the Bi-O bonds in the A-site (ARANDA *et al.*, 2018). The last three modes, ν_{19} to ν_{21} , are related to vibrations of torsional bending and stretching of the Ti/FeO₆ octahedra (JIANG *et al.*, 2014a; JEON *et al.*, 2006; ARANDA *et al.*, 2018; RAGHAVAN *et al.*, 2015).

As shown in Figure 13, changes in the positions and intensities of the Raman peaks were detected. The most noticeable differences were observed for low-frequency regions, which are attributed to the A-site cations and Bi³⁺ ions vibrations in the (Bi₂O₂)²⁺ layers. The modes ν_1 , ν_2 , and ν_3 of BFTO subtly overlap in the BGFTO and BNFTO phases. This effect suggests that the vibrations of the (Bi₂O₂)²⁺ layers are sensitive to the substitution of rare-earth ions into the A-site. Significant changes observed in the intensity for the modes between ν_4 and ν_7 , as well as the ν_7 mode shift towards higher frequencies, occurred due to the substitution of Bi atoms in the perovskite layers by the lighter Gd and Nd atoms. Another fingerprint of this substitution is in the shifting to higher frequencies of ν_{17} and ν_{18} bands. These results agree with the suggestion that rare earth (RE) atoms preferentially replace Bi in perovskite layers (KOVAL *et al.*, 2018). The merging of ν_{16} and ν_{15} modes can be attributed to the decrease of the Ti/FeO₆ octahedra tilting distortion (RAGHAVAN *et al.*, 2015; LAVADO; STACHIOTTI, 2018; DIAS *et al.*, 2019). Thus, the observed Raman modes correlate with the structural changes identified by PXRD, a consequence of the lowering of the orthorhombicity mentioned in the previous section.

Figure 13 – (a) Comparison of the Raman modes for the samples BFTO, BGFTO and BNFTO at room temperature. (b) Zoom view of the modes at low wavenumbers. (c) Experiment and theory for the Raman spectra of the BFTO, BGFTO and BNFTO ceramics at room temperature.

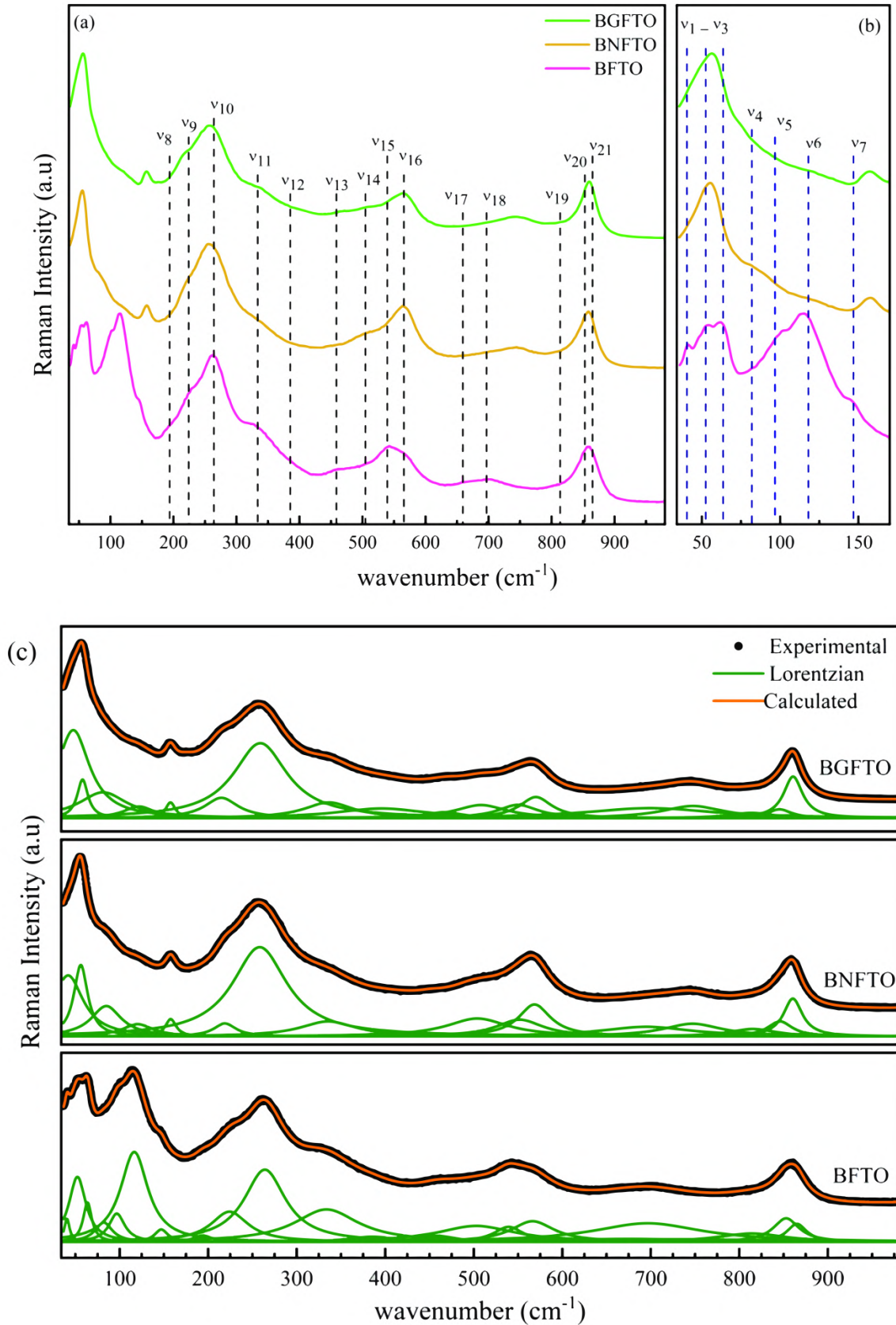


Table 4 – Summary and identification of the observed Raman modes positions for the BFTO, BGFTO, and BNFTO phases.

Phonon positions (cm ⁻¹)	BFTO	BGFTO	BNFTO	Assignments
ν_1	40.4	47.5	41.7	Vibration of Bi ³⁺ ions in (Bi ₂ O ₂) ²⁺ layers
ν_2	52.4	58.0	56.0	
ν_3	63.5			
ν_4	81.9	81.1	84.8	Bi ³⁺ , Gd ³⁺ , and Nd ³⁺ vibrations at the A-sites in the perovskite layers
ν_5	96.7			
ν_6	118.0	121.7	120.3	
ν_7	146.8	157.3	157.5	
ν_8	193.8	214.8	218.7	
ν_9	223.9			
ν_{10}	263.9	258.1	258.9	Internal angles torsional bending of Ti/FeO ₆
ν_{11}	333.6	336.3	335.4	Stretching vibration of oxygen along the c-axis (O-Ti/Fe-O stretching)
ν_{12}	385.2	395.8	407.3	Vibrations in the O-Ti-O bending
ν_{13}	458.4	466.6	450.7	Variation of the bond distances between the Bi atoms within Bi ₂ O ₂ layer and the apical O atoms of the perovskite-like block
ν_{14}	504.5	508.2	503.9	Ti-O torsional mode
ν_{15}	539.1	550.0	551.8	Opposing excursion of the oxygen atoms of TiO ₆
ν_{16}	565.6	570.0	568.5	
ν_{17}	659.1			Stretching of the Bi-O bonds, Bi in the A-site
ν_{18}	696.8	698.8 747.4	694.8 747.2	
ν_{19}	813.7	813.4	815.0	Vibrations Ti/FeO ₆ bonds
ν_{20}	852.8	845.3	845.7	Symmetric stretching mode of the Ti/FeO ₆
ν_{21}	864.9	860.6	860.4	

Source: (SILVA *et al.*, 2020), Copyright ©2020, Springer Nature.

2.3.3 Magnetic Property Analysis

ZFC and FC magnetization curves, measured under an external magnetic field of 50 Oe, are shown in Figure 14-(a-c). From the curves, it was possible to observe an increase in the magnetization as temperature decreases. No divergence between ZFC and FC curves was observed. Remarkably, similar features have been previously observed by Zuo et al. (ZUO *et al.*, 2017) in polycrystalline $\text{Bi}_5\text{FeTi}_{3-3x}(\text{WCr}_2)_x\text{O}_{15}$, with $0 \leq x \leq 0.15$. To infer the nature of the magnetic interaction in our samples, we verified the dependence of the inverse susceptibility (χ) as a function of temperature (T) by fitting this curve with a Curie–Weiss law (CULLITY; GRAHAM, 2011),

$$\frac{1}{\chi} = \frac{T + \theta_{CW}}{C} \quad (2.5)$$

where θ_{CW} is the Curie-Weiss temperature and C is the Curie constant. The fitting curve is represented by the solid lines in Figure 14-(a-c). Note that a good agreement between experiment and theory was obtained.

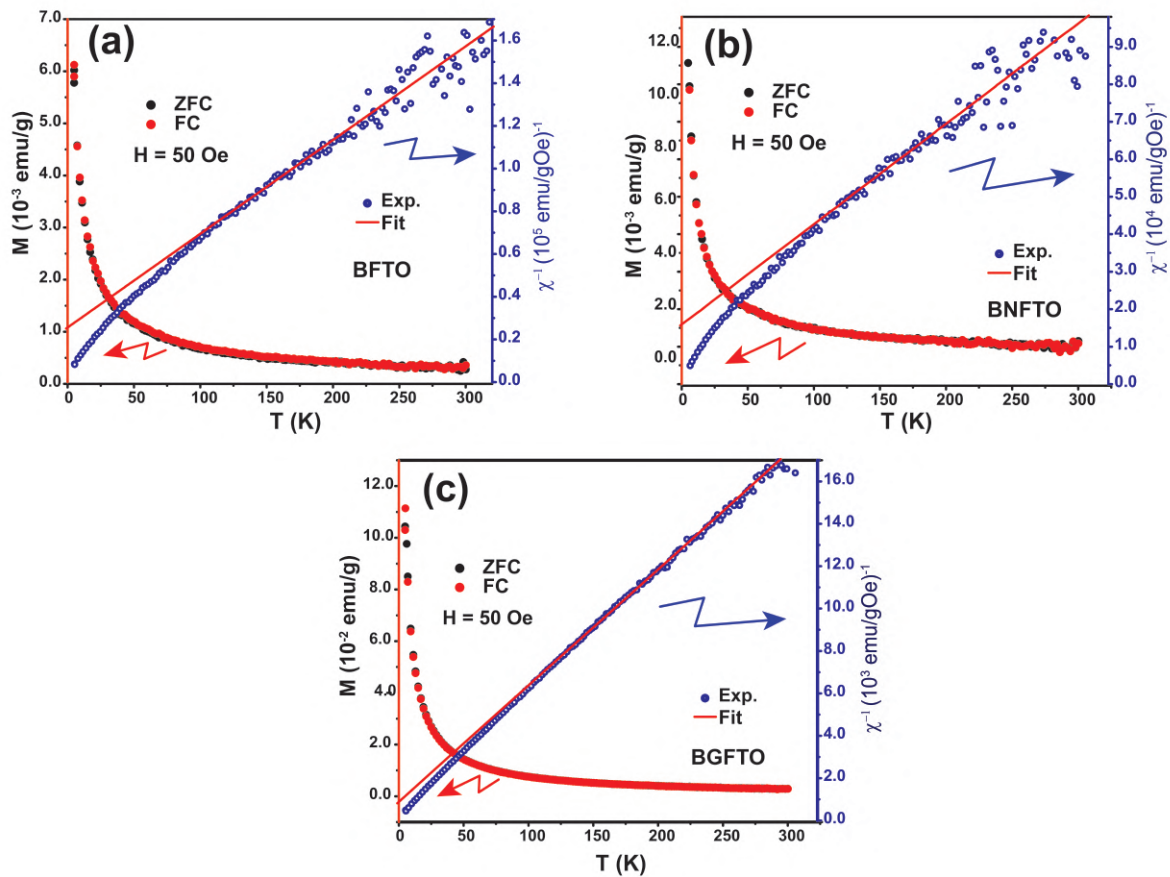
The extrapolation of $1/\chi$ dependence intercepts the temperature axis at $T < 0$, suggesting an interaction with antiferromagnetic (AFM) nature (LIU *et al.*, 2013; TANG *et al.*, 2015). The fitting of BFTO and BNFTO phases gave $C \cong 0.002 \text{ emuK}/(\text{gOe})$, $\theta_{CW} \cong -54.6 \text{ K}$ and $C \cong 0.003 \text{ emu K}/(\text{gOe})$, $\theta_{CW} \cong -55.1 \text{ K}$, respectively. These values suggest that the magnetic response remains almost unchanged. In contrast, the replacement of bismuth with gadolinium causes a striking change in these parameters. In this case, $C \cong 0.016 \text{ emuK}/(\text{gOe})$ and the Curie-Weiss temperature reaches $\theta_{CW} \cong -14.7 \text{ K}$. The decrease of the absolute value of θ_{CW} implies the weakening of the AFM interaction. These results are in accordance with the results previously reported by Lavado et al. (LAVADO; STACHIOTTI, 2018). In summary, all the results suggest weak correlations between the magnetic moments, leading to an AFM behavior.

The magnetization as a function of the magnetic field for the BFTO, BNFTO, and BGFTO are shown in Figure 15-(a-c). At low temperatures (5 K and 10 K), it is possible to observe a well-defined hysteretic behavior. This behavior is typical of materials not having quite antiparallel spins, like an ideal (AFM). This small net magnetization characterizes a well-known effect called canted ferromagnetism (LIU *et al.*, 2013; TANG *et al.*, 2015). The magnetic moment of the antiferromagnetic samples that present spins tilted may be expressed by,

$$\sigma = \sigma_F + \chi H \quad (2.6)$$

where σ is the total moment, σ_F is the moment of the weak ferromagnetism, and χH is the antiferromagnetic component. This canted ferromagnetic effect can be verified in $M(H)$ in two ways. Specifically, at low magnetic fields, it should be observed a hysteretic behavior related to the parasitic ferromagnetism. Also, at high magnetic fields, the dependence of the magnetization with the magnetic field should exhibit a linear behavior, which is related to the AFM component. Both effects were observed in our results as expected in a material with canted ferromagnetism.

Figure 14 – ZFC and FC magnetization curves (left axis) and temperature dependence of the inverse of magnetic susceptibility (right axis) for the (a) BFTO, (b) BNFTO, and (c) BGFTO samples. The solid lines are fits obtained with the Curie–Weiss law.



Source: (SILVA *et al.*, 2020), Copyright ©2020, Springer Nature.

On the other hand, above 25 K, the curves show an almost linear behavior, a fact associated with the reduction of the interaction between the magnetic moments. Similar behavior has been reported in the literature (KHOMCHENKO *et al.*, 2010).

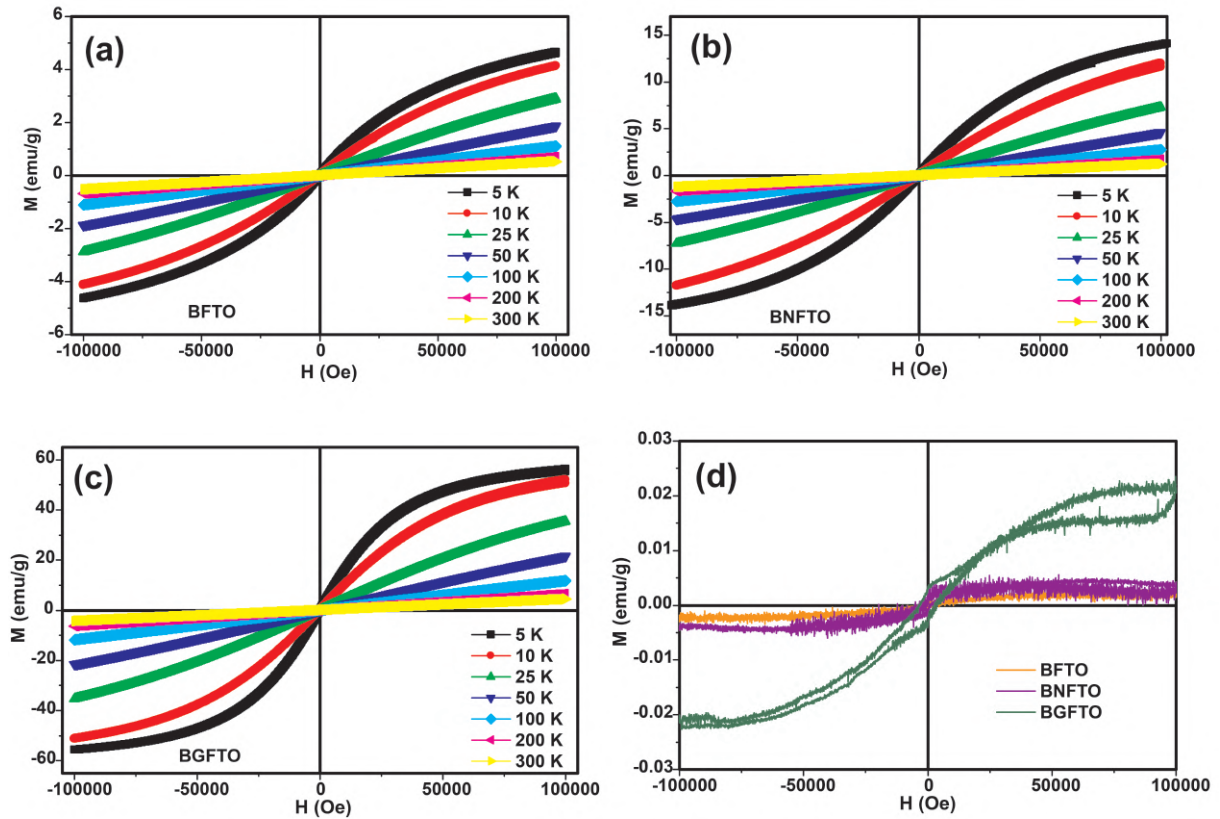
Figure 15-(d) presents the magnetic contribution in the curves. This signal was obtained by subtracting the component of type χH from the magnetization curve measured at 300 K, for field values above 80 kOe. The maximum values of the magnetization are 0.0025

emu/g, 0.004 emu/g, and 0.02 emu/g for BFTO, BNFTO, and BGFTO, respectively. The magnetic properties of the samples are a result of the interplay between structural distortions, crystallite size, and nature of the dopant. The weak ferromagnetic interaction observed in the $\text{Bi}_3\text{R}_2\text{Ti}_3\text{FeO}_{15}$ (R=Bi, Nd, and Gd) ceramics is believed to originate from spin canting of the Fe-based sublattices via the Dzyaloshinskii-Moriya (DM) interaction (QIU *et al.*, 2016; ZUO *et al.*, 2015).

Furthermore, the substitution of Bi ions at the A-site by RE with a small ionic radius will cause further Fe/TiO₆ octahedral distortion which leads to an increase in the magnetization of the BNFTO and BGFTO ceramics. From atomic positions, the structural distortion parameter (Δ), as shown in Table 3, it is possible to see a reduction in the distortion of the Bi₂O₂ layer and Ti1/Fe1-O octahedral and an increase in the distortion of the Ti2/Fe2-O octahedral of the BNFTO and BGFTO samples, when compared to the BFTO sample. It is known that an angle change, and short bond length favor those spins opposite to the field to align towards the applied field resulting in the enhanced magnetization (YU *et al.*, 2017; KHOMCHENKO *et al.*, 2009).

For the difference between the BNFTO and BGFTO phases, it is worth remarking that BGFTO presents larger crystallite size, when compared to BNFTO, as shown in Table 2. This feature is in agreement with the results provided from the Mössbauer spectrum, since these sample also show larger sextet area in comparison to BNFTO, as we discuss in the following. This fact indicates that BGFTO has higher contribution of induced weak ferromagnetism. Similar results have been also observed by Siddique and colleagues for γ -Fe₂O₃ nanoparticles, who identified an increase of the internal magnetic field with increase in particle size (SIDDIQUE *et al.*, 2010). Given the particle size is above 100 nm, the authors also verified a multidomain structure, with the rotation of magnetic domain influencing the final magnetization. Gadolinium trivalent ions have large magnetic moment, of around 6.9 μ_B , which is higher than that found for Fe³⁺, 5.9 μ_B , making easier the rotation of magnetic domain with the applied magnetic field. Hence, we observe the improvement of the magnetic properties in the BGFTO nanoparticles (PULI *et al.*, 2015). The enhancement of the magnetic properties by insertion of Gd³⁺ has been previously observed by Pawar and collaborators in Co-Zn ferrite nanoparticles, in which the authors found an increase of the saturation magnetization values with the increase of Gd³⁺ content (PAWAR *et al.*, 2018). On the other hand, Nd³⁺ ions have magnetic moment close to 3.3 μ_B . Therefore, it is reasonable that BNFTO phase present lower magnetic response, when compared to BGFTO.

Figure 15 – Isothermal magnetization curves for (a) BFTO, (b) BNFTO and (c) BGFTO samples. (d) Magnetic contribution at room temperature, obtained after removing the component χH from the magnetization curve measured at 300 K, for field values above 80 kOe.



Source: (SILVA *et al.*, 2020), Copyright ©2020, Springer Nature.

2.3.4 Mössbauer Spectra Analysis

Figure 16-(a-c) presents the Mössbauer spectrum for the samples studied in this work. The spectra were measured considering two different temperatures (12 and 300 K). In Figure 16-(a), the spectrum for the BFTO sample measured at 12 K is quite-well fitted with one doublet. The inset in Figure 16-(a) shows the spectrum obtained at 300 K, which is similar to that obtained at 12 K, i.e., it can also be well fitted using a doublet. In this case, the obtained isomer shift (δ) was $\delta \sim 0.370$ mm/s and the quadrupole splitting (ΔEQ) was 0.607 mm/s for the result at 12 K, while $\delta \sim 0.245$ mm/s and $\Delta EQ \sim 0.595$ mm/s for the measurement at 300 K. These parameters are summarized in Table 5. The hyperfine parameters obtained are typical of the Fe^{3+} , with $\delta \sim 0.245$ mm/s and $\Delta EQ \sim 0.595$ mm/s (MANOUN *et al.*, 2011). This result is in concordance with the magnetic properties, in which it is possible to observe a linear behavior of the hysteresis cycle at 300 K.

The Mössbauer spectrum of the BNFTO sample measured at 12 K is shown in Figure 16-(b). For this sample, the spectrum is well fitted with a doublet and a sextet, which is indicative

that Fe^{3+} ions have antiferromagnetic order and also contribute to the total magnetic moment of the sample. The relative area of the doublet is approximately 63.2%, whereas, for the magnetic ordering phase, it is 36.8%. The hyperfine parameters for the doublet obtained at 12 K are $\delta \sim 0.300$ mm/s and $\Delta EQ \sim 0.440$ mm/s, referring to Fe^{3+} . For the sextet component, the hyperfine parameters are $\delta \sim 0.340$ mm/s, $\Delta EQ \sim 0.450$ mm/s, and $B_{HF} \sim 50.6$ T. Such values also refer to Fe^{3+} . These values remain unchanged even at 300 K, as shown in the inset of Figure 16-(b). The hyperfine parameters for the doublet are $\delta \sim 0.340$ mm/s and $\Delta EQ \sim 0.460$ mm/s. For the sextet component, in turn, the hyperfine parameters are $\delta \sim 0.480$ mm/s, $\Delta EQ \sim 0.60$ mm/s, and $B_{HF} \sim 50.6$ T, also referring to Fe^{3+} .

Figure 16-(c) shows the Mössbauer spectrum for the BGFTO measured at 12 K and 300 K. The doublet isomer shift obtained at 12 K is 0.300 mm/s and $\Delta EQ \sim 0.400$ mm/s, referring to Fe^{3+} . However, for the sextet component, $\delta \sim 0.330$ mm/s, it is $\Delta EQ \sim 0.150$ mm/s and $B_{HF} \sim 46.6$ T, such values also referring to the Fe^{3+} . These values at 300 K, for the doublet are $\delta \sim 0.320$ mm/s and $\Delta EQ \sim 0.450$ mm/s. To the sextet component, the hyperfine parameters are $\delta \sim 0.370$ mm/s, $\Delta EQ \sim 0.170$ mm/s and $B_{HF} \sim 46.6$ T, referring to Fe^{3+} .

It is well known that the hyperfine parameters δ and ΔEQ depend on several factors. The isomer shift has two components – the chemical isomer shift and the second-order Doppler shift. The chemical isomer shift depends on the density of s -type electrons within the ^{57}Fe Mössbauer nucleus, being weakly dependent on temperature. Nevertheless, the second-order Doppler shift increases with the decrease of the temperature. The quadrupole splitting value allows us to deduce the symmetry of the charge distribution around ^{57}Fe ions and thus the symmetry of the ^{57}Fe site. Therefore, the value of ΔEQ can provide information about the symmetry of crystal lattice and its local distortions. The results summarized in Table 5 demonstrate that the ΔEQ values are practically independent of the temperature.

However, by comparing the quadrupole splitting values of BFTO with BNFTO and BGFTO, we can observe there is a decrease in the values of ΔEQ . This may be due to the replacement of Bi^{3+} ions, which has a larger radius, by Nd^{3+} and Gd^{3+} , as illustrated in Figure 16-(d). Doping the Bi-site with different radii ions (Nd^{3+} and Gd^{3+}) induces lattice distortion (compression) and tilting of FeO_6 octahedra. The tilting of FeO_6 octahedra would give rise to a canted spin structure, which could favor the existence of a weak ferromagnetic phase via the antisymmetric Dzyaloshinskii–Moriya interaction. This result is in concordance with the PXRD, Raman spectroscopy measurements, and the ferromagnetic contribution at room temperature.

Table 5 – The hyperfine parameters of samples BFTO, BNFTO, and BGFTO at 12 and 300 K.

Samples	Temperature (K)	δ (mm/s)	ΔE_Q (mm/s)	B_{HF} (T)	Area (%)
BFTO	12	0.370	0.607		Dublet
	300	0.245	0.595		100
BGFTO	12	0.300	0.400		Dublet 60.6
		0.330	0.150	46.6	Sextet 39.4
	300	0.320	0.450		Dublet 60.6
		0.370	0.170	46.6	Sextet 39.4
BNFTO	12	0.300	0.440		Dublet 63.2
		0.450	0.340	50.6	Sextet 36.8
	300	0.340	0.460		Dublet 63.2
		0.480	0.600	50.6	Sextet 36.8

Source: (SILVA *et al.*, 2020), Copyright ©2020, Springer Nature.

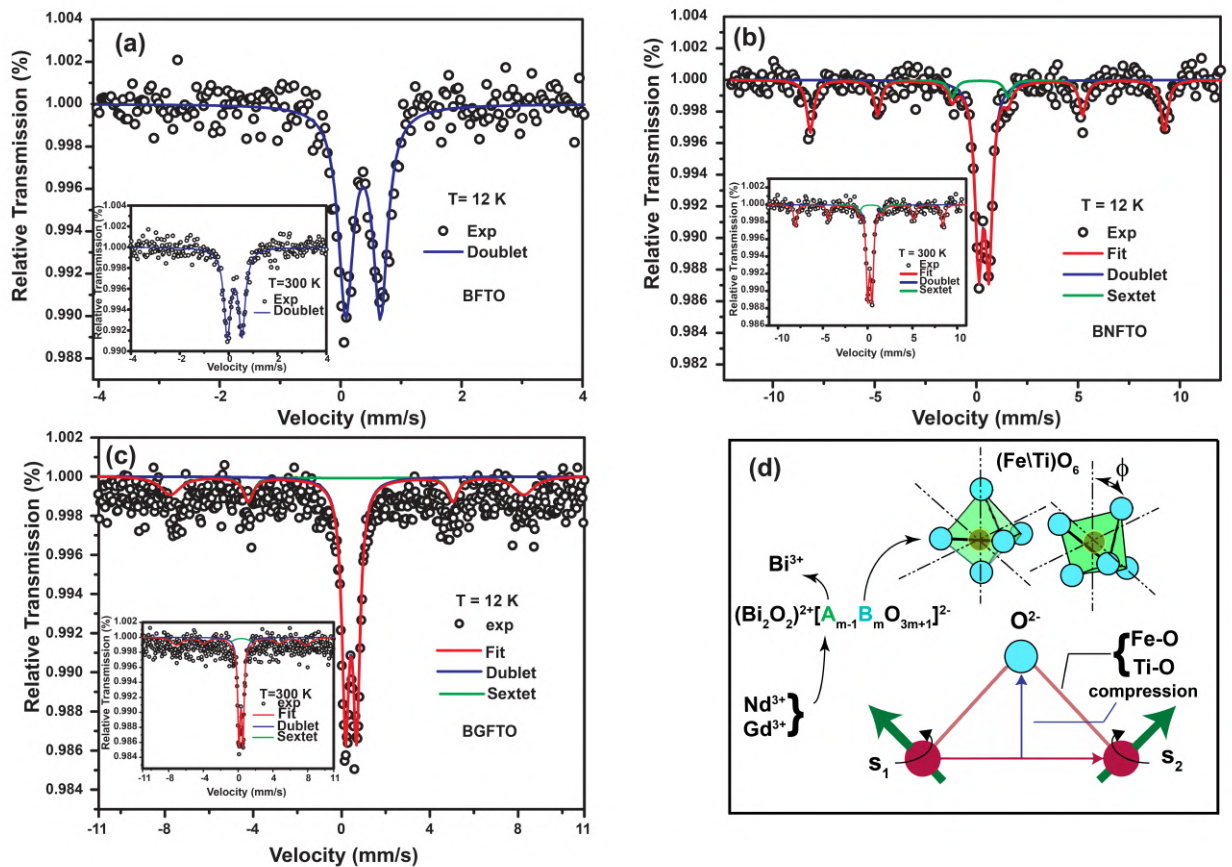
2.4 Conclusions

In summary, $\text{Bi}_3\text{R}_2\text{Ti}_3\text{FeO}_{15}$ (R = Bi, Nd, and Gd) phases have been successfully synthesized. The Rietveld refinement showed that all samples have orthorhombic lattice with space group $A2_1am$. The room temperature PXRD and Raman spectra show that the replacement of bismuth with gadolinium and neodymium causes a structural distortion in the BFTO phase. This result can be attributed to the ionic radius difference between Gd^{3+} (~ 0.105 nm), Nd^{3+} (~ 0.111 nm), and Bi^{+3} (~ 0.117 nm).

The magnetic measurements enable us to verify a partial Bi-site substitution by Gd and Nd ions. The tilting of FeO_6 octahedra would give rise to a canted spin structure, which could favor the existence of a weak ferromagnetic phase via the antisymmetric Dzyaloshinskii–Moriya interaction.

As a result, there was a considerable increase in the magnetic properties in the studied samples. These results bring to light new properties of the already known BFTO phase and their adjustable multifunctionality through a partial replacement of bismuth by neodymium and gadolinium, placing them as highly promising candidates in a wide variety of technological applications.

Figure 16 – Mössbauer spectra of (a) BFTO, (b) BNFTO and (c) BGFTO compounds at $T = 12$ K and $T = 300$ K (inset). (d) Illustration to the replacement of Bi^{3+} ion by Nd^{3+} and Gd^{3+} . Different radii induce lattice distortion (compression) and tilting of FeO_6 octahedral by the Nd^{3+} , and Gd^{3+} ion doping into the Bi-site.



Source: (SILVA *et al.*, 2020), Copyright ©2020, Springer Nature.

3 DIELECTRIC PROPERTIES OF BLSF AT MICROWAVE AND RADIOFREQUENCY

“Science of today is the technology of tomorrow.”

Edward Teller

3.1 Introduction

Due to this great versatility of its properties from structural modifications, certain performance parameters of layer-type bismuth family, have been arousing interest to applications in electronic devices, such as the high dielectric constant (ϵ), low loss tangent ($\tan\delta$), and good stability of the thermal coefficient capacitive temperature coefficient of capacitance (TCC), and coefficient of frequency resonant (τ_f). For example, Wu and colleagues (WU *et al.*, 2021) demonstrated that Rb/Nb co-substituted $\text{Bi}_{0.5}\text{Na}_{0.5}\text{TiO}_3$ -based ceramics display TCC < 10% and 15% in the temperature range of - 43 to 292 °C. It is an applicable candidate material for X7R and X8R capacitors (the Electronic Industries Association (EIA) standard specification codes) (MIAO *et al.*, 2017). The suggestion for this great performance is that the introduction of Nb^{5+} and Rb^+ ions can reduce oxygen vacancies and, thus, decrease tand from structural distortions. On the other hand, it has been difficult to find ceramic materials that meet more stringent specifications in terms of their thermal stability, such as X4D capacitors, which have TCC $\leq \pm 3.3\%$, and are used in situations where dielectric specifications are required with greater temperature reliability.

In the microwave (MW) regime, the research for better performance parameters, such as operation frequency (f_0), return loss (S_{11}), bandwidth (BW), directivity (D), gain (G), efficiency (η), and τ_f has attracted interest in the BLSF class, operating as dielectric resonator antennas (AGUIAR *et al.*, 2017; SILVA *et al.*, 2014; OLIVEIRA *et al.*, 2019; JUNIOR *et al.*, 2018). Aguiar *et al.* (AGUIAR *et al.*, 2017), reported that the behavior of τ_f for the BFTO phase is sensitive to different concentrations of V_2O_5 , finding - 304.3 to - 192.6 ppm °C⁻¹ (from 1 to 5 wt%). However, it did not investigate the other parameters. Previous works to $\text{Ba}_{1-x}\text{Nd}_{2x/3}\text{ZrO}_3$ ($x = 0.0, 0.02, 0.04, 0.06, 0.08, \text{ and } 0.1$) ceramics, using a monopole Dielectric Resonator Antenna (DRA) (PARIDA *et al.*, 2015), demonstrates that the ϵ decreased from 38.40 to 23.49, and the value of τ_f changed from 384.71 to 113.7 ppm °C⁻¹ with increasing of Nd^{3+} content.

This is justified due to a smaller radius of Nd^{3+} than Ba^{2+} , that gives rise to a shortening of Zr-O bonds of $\text{Ba}_{1-x}\text{Nd}_{2x/3}\text{ZrO}_3$ phase. This affects the polarizability and the anharmonicity associated with the motion of ions, contributing to ϵ and τ_f reduction.

In the previous chapter, the focus was on the analysis of structural and magnetic properties. It was demonstrated that the replacement of Bi^{3+} ions by rare earth elements (Gd and Nd) affects the crystalline structure of the BFTO, resulting in different vibrational, magnetic and hyperfine properties. Therefore, based on the above discussion, this chapter lead us naturally to an investigation systematical of microstructural and electrical properties of the $\text{Bi}_3\text{R}_2\text{Ti}_3\text{FeO}_{15}$ (R = Bi (BFTO), Gd (BGFTO), and Nd (BNFTO)) ceramics by impedance spectroscopy (IS) and dielectric response to radiofrequency/microwave regime as a function of the temperatures. In an innovative character, these materials acting as ceramic capacitors are compared to previous works (WU *et al.*, 2021; MIAO *et al.*, 2017; HAN *et al.*, 2020) (with EIA standard specification) and the Cylindrical Dielectric Resonator Antenna (CDRA) performance parameters are contrasted in detail with other published works (SILVA *et al.*, 2014; OLIVEIRA *et al.*, 2019; JUNIOR *et al.*, 2018) by experimental and simulated analysis.

3.2 Experimental Methods

The details employed for manufacturing process samples were detailed in chapter 2. Briefly, the powders were mechanically mixed and brought to the oven and calcined in air at $1000\text{ }^\circ\text{C}/6\text{ h}$. Uniaxial pressing of powders was done at 148 MPa for 5 min, and the pellets were formed with dimensions of approximately 12 mm of diameter and a thickness of 1.5 mm. The pellets were sintered at $1100\text{ }^\circ\text{C}$ for 3 h in air.

The mapping surface of the samples was studied using a scanning electron microscope (SEM). The stubs of the specimen representative of the bodies surface were sputter-coated with gold (20 nm thick) on a Quorum QT150ES Metallizer and analyzed on a Quanta-FEG FEI environmental scanning microscope with an incident electron beam of 20 kV. The average grain diameters were measured by at least 150 grains from different areas using ImageJ software (SCHNEIDER *et al.*, 2012).

Impedance spectroscopy (IS) was performed in a Solartron 1260 Impedance Analyzer in a range of $29\text{--}450\text{ }^\circ\text{C}$ by applying an alternating voltage (2.0 V) with a frequency ranging from 1 Hz to 10 MHz. Silver paste (Joint Metal PC-200) was applied on both surfaces as electrodes to build a parallel face capacitor to make dielectric measurements. The TCC was

calculated according to the following equation (HAN *et al.*, 2020),

$$\text{TCC} = \frac{\Delta\varepsilon}{\varepsilon_{29}\Delta T} \times 100\% \quad (3.1)$$

where ε_{29} is ε at 29 °C, $\Delta\varepsilon$ and ΔT (29—150 °C) are changes in ε and temperature, respectively.

It was used an Agilent Network Analyser (model N5230A) for the characterization at microwave frequency. The Hakki–Coleman method (HAKKI; COLEMAN, 1960), by the analysis of the TE_{011} mode, was used to obtain ε and $\tan\delta$. The Silva-Fernandes-Sombra (SFS) methodology (SILVA *et al.*, 2012) was used to calculate τ_f of all samples, in temperature range of 29—100 °C by Equation 3.2:

$$\tau_f = \frac{1}{f_i} \frac{\Delta f}{\Delta T} \times 10^6 \text{ ppm/}^\circ\text{C} \quad (3.2)$$

where f_i is the initial frequency (GHz), Δf is the variation of resonant frequency (GHz) and ΔT is the temperature range (°C).

The S_{11} was measured through the vector network analyser of Agilent N5230A. The CDRAs has a radius a , height h , and dielectric constant ε . The antenna operating frequency (f_0) can be calculated by Equation 3.3:

$$f_0 = \frac{6.324 c}{2\pi a\sqrt{\varepsilon+2}} \left[0.27 + 0.36 \left(\frac{a}{h} \right) + 0.02 \left(\frac{a}{2h} \right)^2 \right] \quad (3.3)$$

where c is the speed of light in a vacuum (SILVA *et al.*, 2014; OLIVEIRA *et al.*, 2019; JUNIOR *et al.*, 2018). The antenna setup used can be described as a square copper ground plane connected to the coaxial probe (50 Ω) and Sub-Miniature version A (SMA) connector, perpendicularly positioned. The three CDRAs samples were measured separately very near to the probe, to allow the better adjustment of signal. Numerical simulations were performed to obtain far fields parameter (D , G , and η) through Ansoft High Frequency Structure Simulator (HFSS©software), employing the Finite Element Method (FEM).

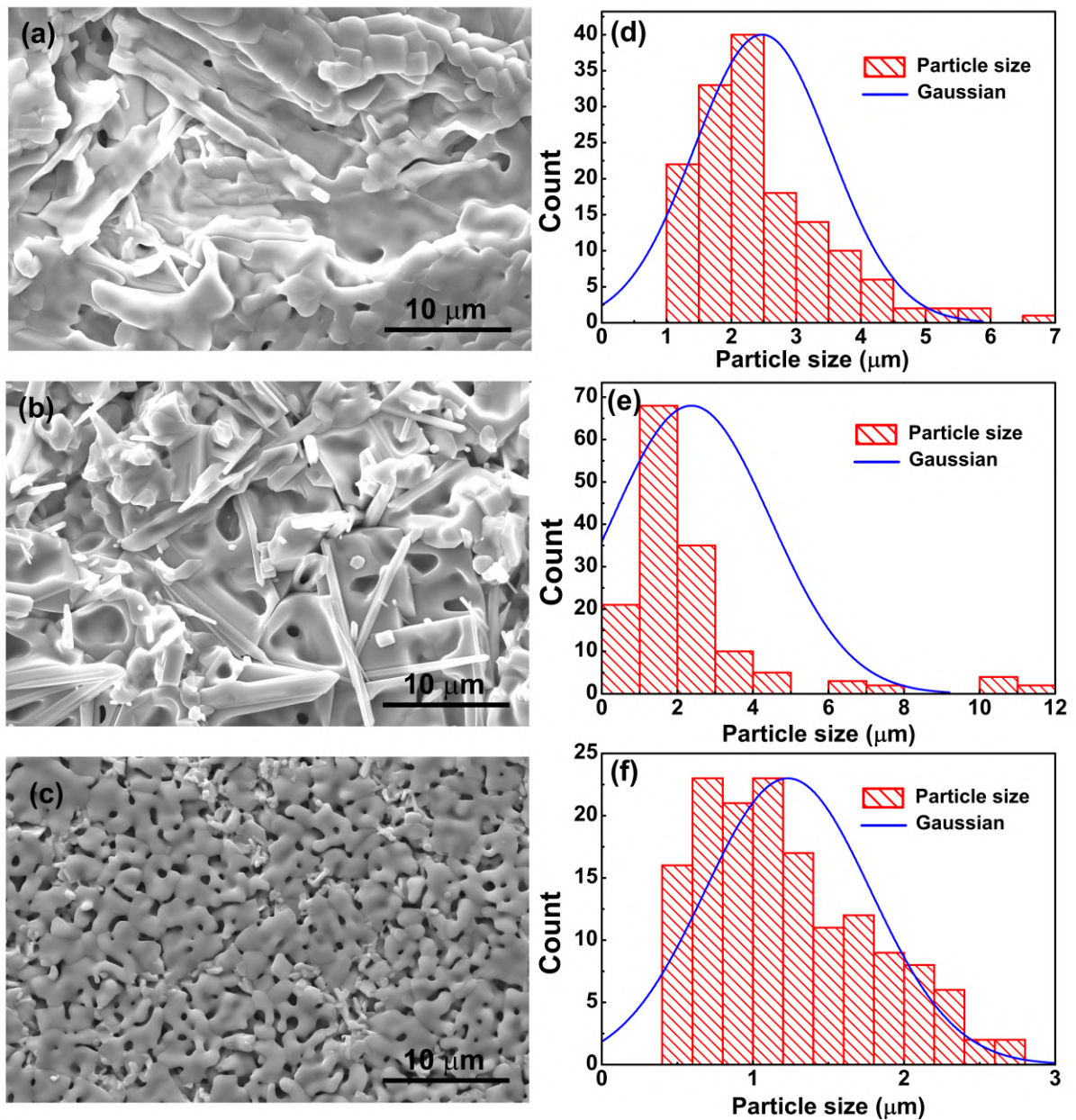
3.3 Results and Discussion

3.3.1 Morphological Analysis

The surface morphology of the BFTO, BGFTO, and BNFTO are shown in Figure 17-(a–c), respectively. It can observe grains zones and partially molten interfacial regions of ceramic, improving the densification of the material. SEM micrographs of BFTO show a microstructure

with plate-like grains, overlapping each other. This plate-like morphology of the grain is a characteristic feature of bismuth layer compounds. Lateral growth of the platelets is preferred in order to maximize the area of low energy faces perpendicular to the $\{001\}$ planes (HORN *et al.*, 1999). Therefore, in the process of sintering, the grains grow in the $a - b$ plane and attain plate-like in the texture of the final microstructure.

Figure 17 – SEM images of the samples: (a) BFTO, (b) BGFTO, and (c) BNFTO ceramics sintered at 1100 °C for 3 h in air. The (d) BFTO, (e) BGFTO, and (f) BNFTO give the average grain size (AG), particle size distribution, and standard deviation (SD) of each ceramic.



Source: (SILVA *et al.*, 2021), Copyright ©2021, Springer Nature.

There is an evident change in size and shape of the BGFTO and BNFTO grains

compared to the BFTO ceramic. Besides the plate-like morphology, the BGFTO shows also needles. BNFTO presented partial melting regions and a better sinterability. The grain size distribution, obtained by ImageJ and Gaussian Fitting, is plotted in Figure 17-(d-f) for BFTO, BGFTO, and BNFTO samples, respectively. The average grain size decreased slightly from 2.47 μm (SD = 1.04 μm) and 2.37 μm (SD = 2.09 μm) for BFTO and BGFTO, respectively, to 1.23 μm (SD = 0.54 μm) for BNFTO.

The presence of Gd and Nd, can help to minimize Bi volatilization and reduce the concentration of oxygen vacancies, which then results in slower oxygen ion motion and consequently lowers grain growth rate (BEHARA *et al.*, 2018; BOBIĆ *et al.*, 2016). Nevertheless, as compared to BGFTO, BNFTO has the smallest grain size. This difference can be justified due to bond dissociation energy between the phases (Gd–O $\sim 715 \text{ kJ mol}^{-1}$ and Nd–O $\sim 703 \text{ kJ mol}^{-1}$) and the crystallite size of BGFTO be greater than BNFTO, as demonstrated in chapter 2. It is known that the higher bond dissociation energy of the oxide bonds of the elements releases a high amount of energy, while forming the final microstructure and is likely to help the coming together of crystallites to form larger grains (GUPTA *et al.*, 2021). However, the final result of grain size depends on many factors, such as the manufacturing method, temperature and time of treatment. The identification of changes in grain and grain boundaries morphology is important for studying the electric behavior of the electroceramics.

3.3.2 Dielectric Characterization

Impedance spectroscopy is a well-known technique, and it is employed in revealing the electrical properties of different structures, e.g., grain, domain boundary, grain boundary and electrode/sample contact, in ceramics materials (MACDONALD; JOHNSON, 2005). IS analysis present in this study was performed by impedance (Z^*), modulus (M^*), and electrical permittivity (ϵ^*). These terms can be written as $Z^* = Z' - jZ''$ and $M^* = M' + jM''$, where Z' , M' and Z'' , M'' are, respectively, the real and imaginary parts of these quantities and are related by Equations 3.4 and 3.5

$$M' = \omega C_0 Z'' \quad (3.4)$$

$$M'' = \omega C_0 Z' \quad (3.5)$$

where $\omega = 2\pi f$ is the angular frequency, $C_0 = \epsilon_0 A/t$, ϵ_0 (vacuum permittivity) equal to $8.854 \times 10^{-12} \text{ F m}^{-1}$, A is the electrode area, and t is the thickness of the samples.

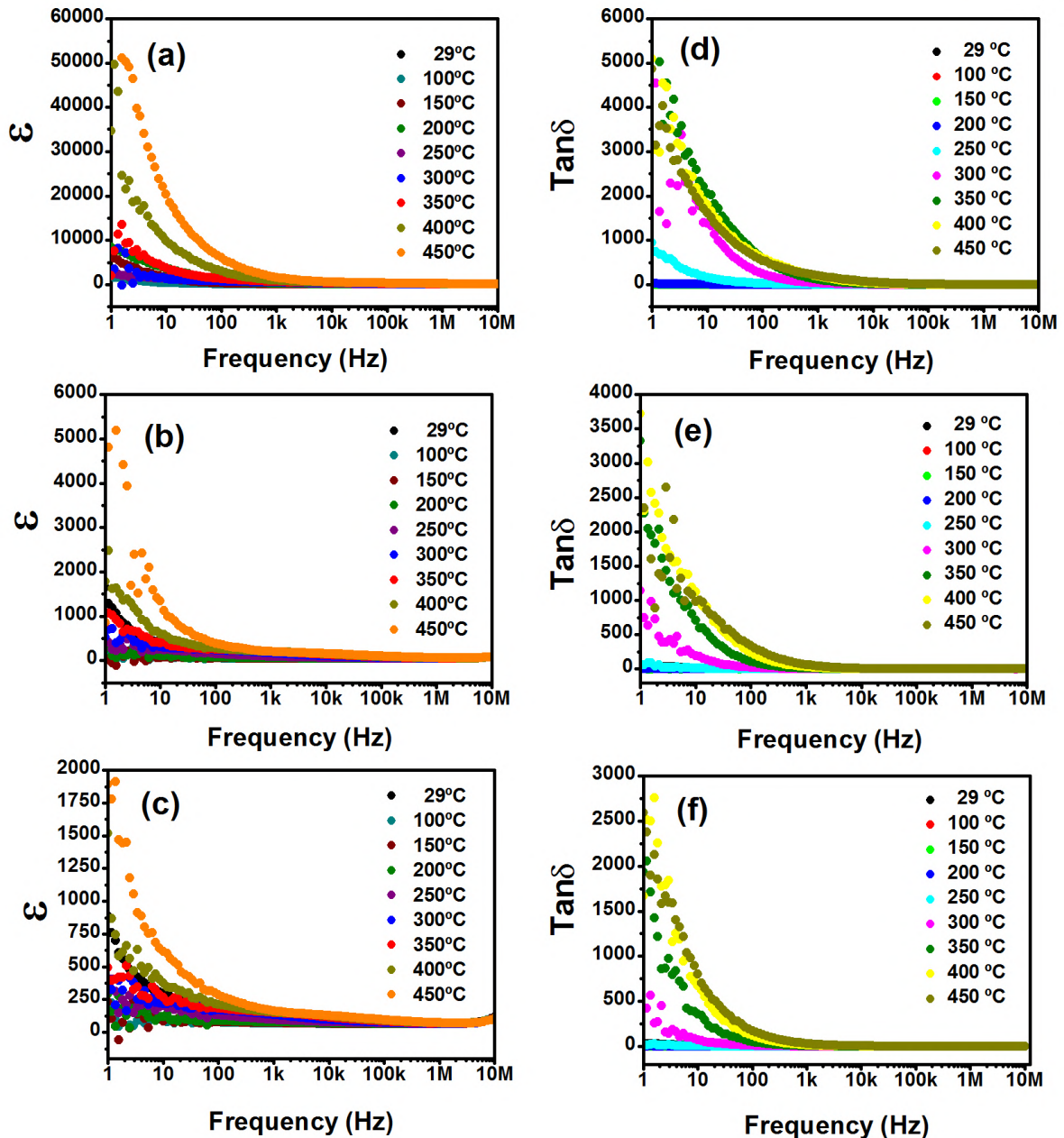
The frequency (1 Hz to 10 MHz) dependence of ϵ and $\tan\delta$ in a range of temperature ranging from 29 to 450 °C, for BFTO, BGFTO, and BNFTO, respectively, are displayed in Figure 18-(a–f). In the low frequency range, the ϵ and $\tan\delta$ decreased in pace with the increase in frequency. Besides that, the curves show a dispersion region exhibited at lower frequency and a plateau region occurring at higher frequency. This behavior is typical for dielectric materials, where at lower frequency region presence of electronic, ionic, orientational, and space-charge polarization exist and contribute towards total polarization of the sample (YU *et al.*, 2020). Moreover, the ϵ and $\tan\delta$ nearly constant at higher frequency may be due to absence of different types of polarization (space charge, for example) and conduction phenomena (PAIVA *et al.*, 2015).

By comparing of the dielectric characteristics of both samples, it appears that Gd and Nd incorporation lowers the dielectric constant and affects the dielectric loss. In comparison, for room temperature (RT) measurements at 100 kHz, BFTO has $\epsilon \sim 83$ and $\tan\delta \sim 4.8 \times 10^{-2}$, BGFTO $\epsilon \sim 51$ and $\tan\delta \sim 4.7 \times 10^{-2}$, and BNFTO $\epsilon \sim 67$ and $\tan\delta \sim 3.2 \times 10^{-2}$. It is reported that the spontaneous unit-cell deformation accompanies spontaneous polarization in perovskite ferroelectrics (ZHANG *et al.*, 2021). The orthorhombic symmetry has domain walls that vary as a function of crystal distortion (MANTRI; DANIELS, 2021). The structural distortion parameter arising due to substitution of the lanthanides at A-site cations in the layer perovskite, as it was calculated in previous researches (SILVA *et al.*, 2020) (see Chapter 2). The result was a reduction in the distortion of the Bi_2O_2 layer and Ti/Fe(1)–O octahedral and an increase in the distortion of the Ti/Fe(2)–O octahedral of the BGFTO and BNFTO samples, when compared to the BFTO. As a consequence, it is expected that the spontaneous polarization of BGFTO and BNFTO ceramics decreases owing to the decrease of dipole moments. Moreover, it was expected that the motion of domain walls subsided at high temperature, inducing a decrease of dielectric permittivity and loss values.

The temperature dependence of ϵ and $\tan\delta$ for BFTO, BGFTO, and BNFTO ceramics from RT to 450 °C with different frequencies are displayed in Figure 19-(a–f). Figure 19-(a) (BFTO) shows, at low temperature range, the nearly invariable ϵ is maintained up to 200 °C. In that same temperature region, for 100 Hz, a peak is observed and later, it exhibits an abrupt increase. This peak becomes a shoulder, which disappears with increasing frequency. Moreover, this dielectric anomaly behavior is significantly suppressed and becomes a shoulder plainly in BGFTO and BNFTO, as plotted in Figure 19-(b) and (c), respectively. The $\tan\delta$ for all the phases

shows a similar behavior, i.e., first increases slowly between RT and 250 °C and then increases abruptly above 250 °C, as shown in Figure 19-(d-f).

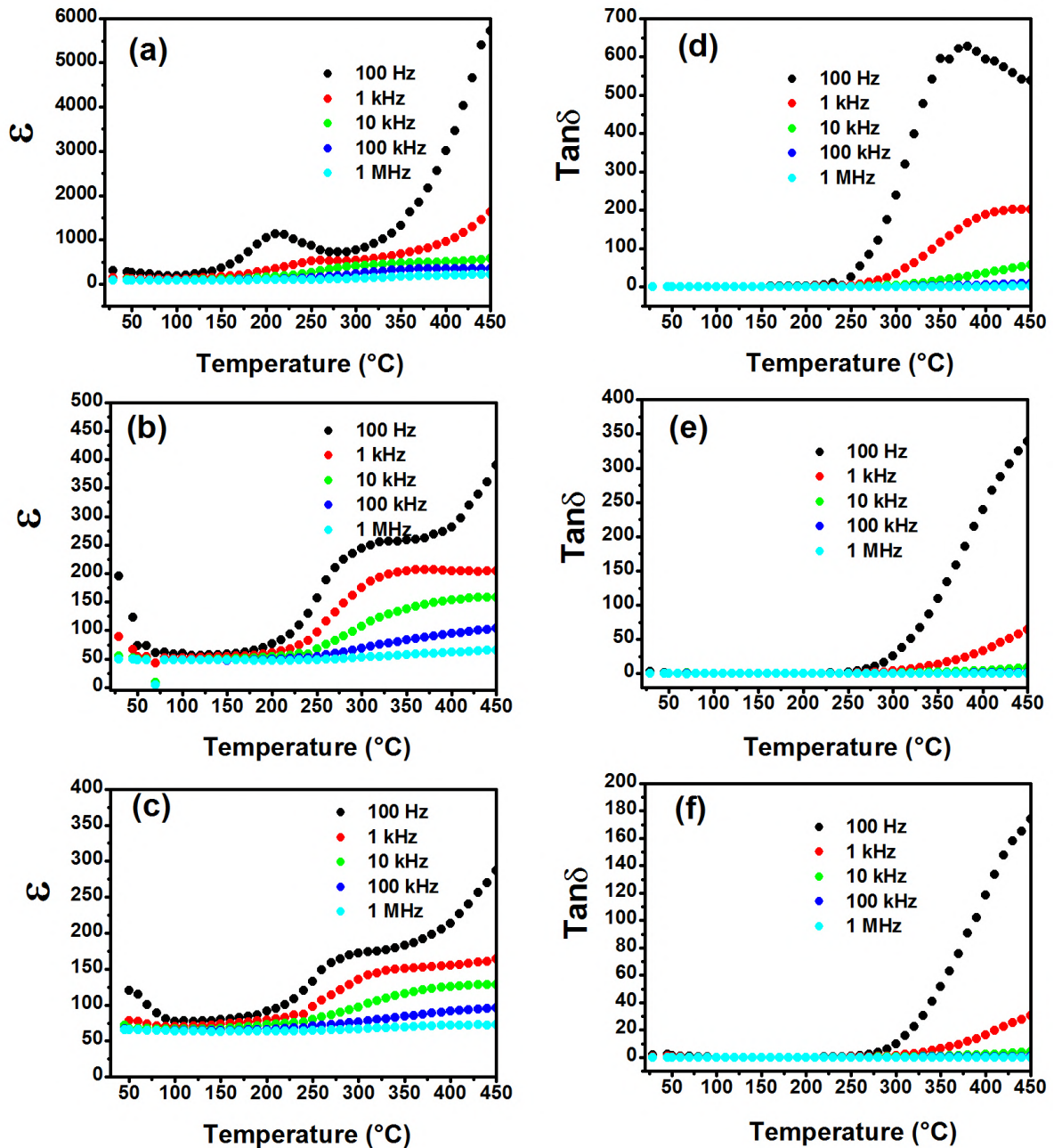
Figure 18 – ϵ for (a) BFTO, (b) BGFTO, (c) BNFTO, and $\tan\delta$ for (d) BFTO, (e) BGFTO, (f) BNFTO as a function of frequency under different temperatures.



Source: (SILVA *et al.*, 2021), Copyright ©2021, Springer Nature.

According to the literature (KOVAL *et al.*, 2018; FERREIRA *et al.*, 2020; SILVA *et al.*, 2020), the phase transition of BFTO ceramics occurs when the temperature rises to T_C up to ~ 750 °C (ferroelectric orthorhombic phase to paraelectric tetragonal phase), a temperature range well above our experimental limitations. On the other hand, several studies (BOBIĆ *et al.*, 2016; GUPTA *et al.*, 2021; YU *et al.*, 2020) suggest that the physical mechanism of dielectric

Figure 19 – ϵ for (a) BFTO, (b) BGFTO, (c) BNFTO, and $\tan\delta$ for (d) BFTO, (e) BGFTO, (f) BNFTO as a function of temperature under different frequencies.



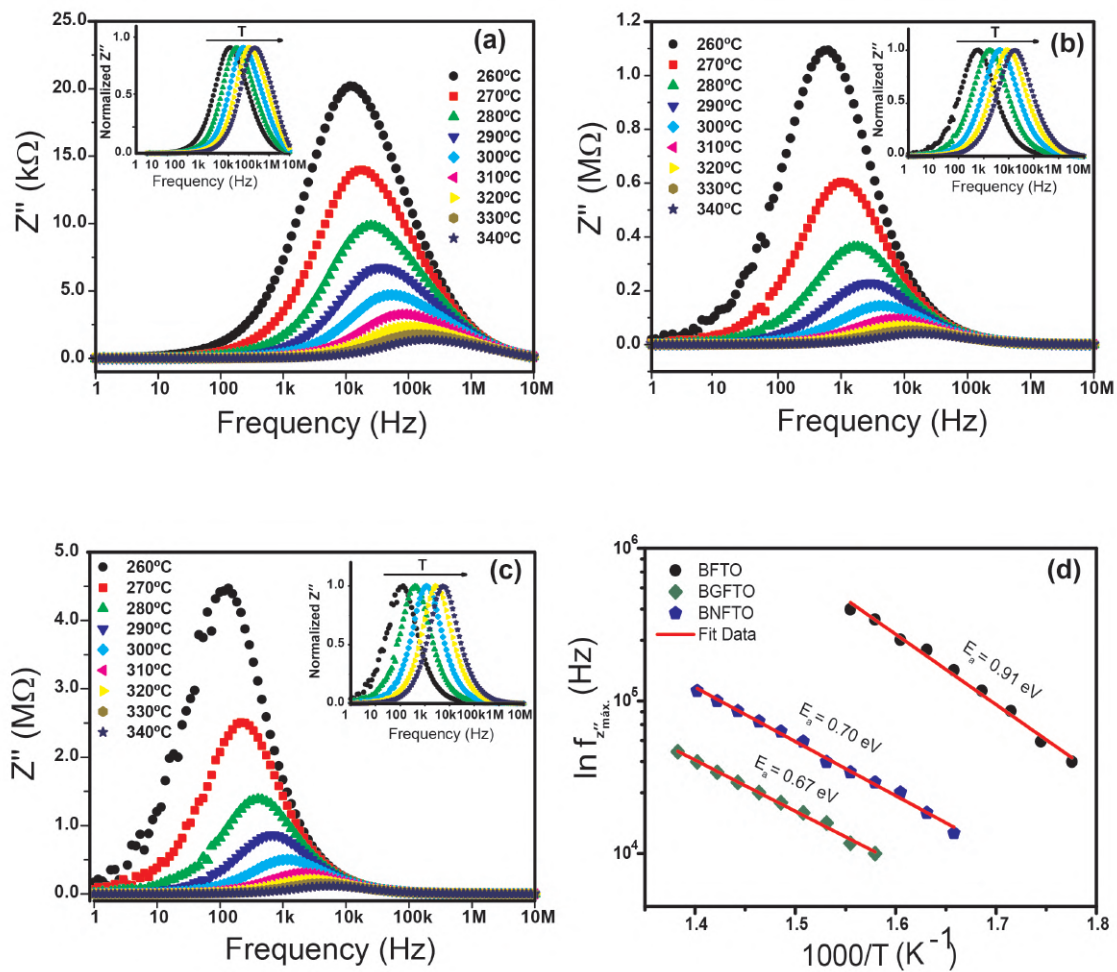
Source: (SILVA *et al.*, 2021), Copyright ©2021, Springer Nature.

anomaly behavior of both ϵ and $\tan\delta$ can be attributed to the presence of thermally activated charges, such as space charges region between interface and electrode, charged defects space charge, and relaxation phenomenon. Prajapat *et al.* (PRAJAPAT *et al.*, 2019) reported a similar anomaly for BFTO with V^{5+} ($\leq 50\%$) doping at *B*-site, and suggest an analysis using IS.

Figure 20-(a–c) shows the variation of Z'' spectrum of the BFTO, BGFTO, and BNFTO ceramics for a range of temperature 260–340 °C and the inset of these figures show the Z''/Z''_{max} normalized spectrum. It is possible to notice a large dispersion and a peak displacement

(Z''_{max}) with an increase in temperature. For samples containing REs, a greater peak displacement is noticeable. This characteristic informs the presence of a thermally activated electrical relaxation processes in the material (JONSCHER, 1999). For materials with high electrical permittivity, this indicates an active and localized conduction inside the grains (RAYMOND *et al.*, 2005). For $\text{Bi}_5\text{Ti}_3\text{FeO}_{15}$ phase, Mohapatra *et al.* (MOHAPATRA *et al.*, 2014) found similar results for a range from the RT to 500 °C.

Figure 20 – Z'' for (a) BFTO, (b) BGFTO, and (c) BNFTO ceramics as a function of frequency for different temperatures. The inset shows the normalized Z''/Z''_{max} shift of the peaks as a function of temperature. (d) Arrhenius plots for the samples at f_{max} versus $1000/T$.



Source: (SILVA *et al.*, 2021), Copyright ©2021, Springer Nature.

In order to understand this relaxation process, the activation energy (E_a) values for the studied ceramics were obtained by Arrhenius Equations 3.6 and 3.7

$$f_{dc} = \sigma_0 \exp(-E_a / \kappa_B T) \quad (3.6)$$

$$\sigma_{max} = f_0 \exp(-E_a / \kappa_B T) \quad (3.7)$$

where f_{max} is the peak frequency, known as relaxation frequency (extracted from Z''_{max} and M''_{max}), σ_{dc} is dc conductivity (in 100 Hz), κ_B is the Boltzmann constant (8.617×10^{-5} eV K⁻¹), T is the temperature (K), σ_0 and f_0 are pre-exponential factors. Figure 20-(d) shows the values extracted from Z''_{max} . The other values calculated from σ_{dc} and M''_{max} are shown in Table 6. The values summarized in Table 6 suggests that the E_a values agrees with ionized oxygen vacancy state in the perovskite structure. To case of singly ionized is in the range of 0.3–0.4 eV and that of doubly ionized is 0.6–1.2 eV (GUPTA *et al.*, 2021; PAIVA *et al.*, 2015; MOHAPATRA *et al.*, 2014). The result found in our work is consistent with the values of doubly ionized oxygen vacancy state. This is an expected result, due to the well-known problem of bismuth volatilization during the sintering process (BADOLE *et al.*, 2020; JI *et al.*, 2021a).

Table 6 – Dimensions, activation energy (measured from σ_{dc} , M''_{max} , and Z''_{max} spectrum) and the relative density for all samples.

	Activation energy (eV)			Diameter (mm)	Thickness (mm)	Relative Density (%)
	σ_{dc}	M''_{max}	Z''_{max}			
BFTO	0.93	0.90	0.91	11.864	1.638	74.90
BGFTO	0.72	0.76	0.70	12.637	1.764	60.81
BNFTO	0.67	0.64	0.67	12.842	1.470	55.08

Source: (SILVA *et al.*, 2021), Copyright ©2021, Springer Nature.

The M'' spectrum is shown in Figure 21-(a–c). As one can see, a plateau region occurring at lower frequency, becoming more evident in the BFTO sample (until to the 100 Hz). A single well-defined peak is present in the curves for the three ceramics phases. Physically, a single peak (M''_{max}) in the M'' spectrum, defines the regions where the charge carriers can move over long distances (before the peak) or confinement (after the peak) (SHARMA *et al.*, 2015). The shifts of the peaks to regions of high frequencies occurs more pronounced for the phases that contain the REs. This fact is in accordance with the results of Z'' spectrum (see inset Figure 20-(a–c)). Furthermore, it is suggesting that the BGFTO and BNFTO samples must overcome a lower potential barrier during the conduction process compared to the BFTO phase.

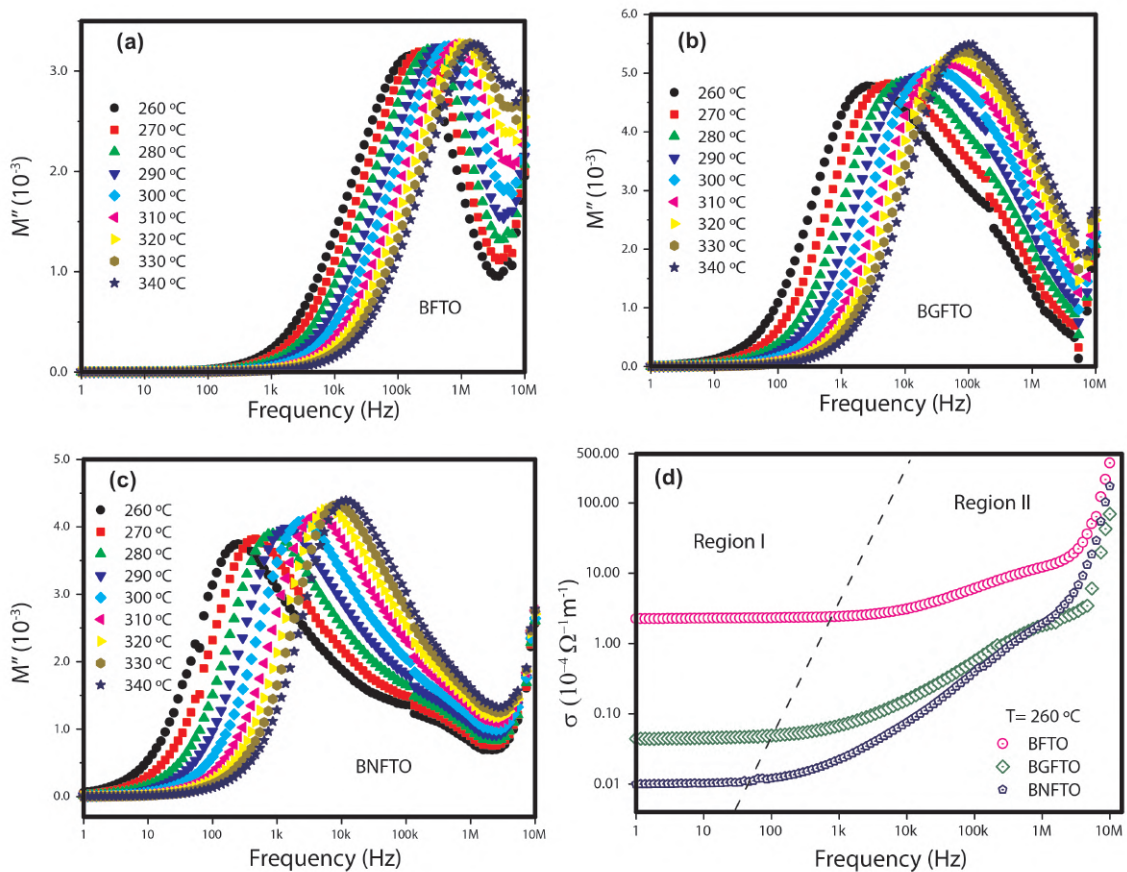
Figure 21-(d) shows the frequency dependence of conductivity (σ) at a fixed temperature of 260 °C, which is the same initial temperature for analysis performed with Z'' and M'' formalism. The curves present two well-defined regions divided by a dashed line. In the region (I), a behavior practically independent of the frequency prevails due to dc conductivity domain. For region (II), observed at high frequencies, the conductivity increases rapidly. This imply that

the conduction in the ceramics obeys the Jonscher's power-law (JONSCHER, 1977):

$$\sigma(\omega) = \sigma_{dc} + B\omega^s \quad (3.8)$$

where σ_{dc} is the dc conductivity, B is a constant that is related to the strength of the polarization process and $0 \leq s \leq 1$ represents the degree of interaction between mobile ions/charge carriers present in the sample (KUSHVAHA *et al.*, 2020). In some theoretical models, the parameters B and s are used to specify the conduction mechanism (SUTAR *et al.*, 2014). As this is out of the scope of this work, we will study this behavior in our following work. However, an observation is pertinent: the plot demonstrates that the ac conductivity of BFTO samples shows the best efficiency, when compared with the BGFTO and BNFTO ceramics. Two factors can be suggested for this result. First, the decrease in relative density and decrease in grain size for the BGFTO and BNFTO ceramics (see Table 6). Second, the difference in the amount of oxygen vacancy as compared to BFTO.

Figure 21 – Frequency dependence of M'' at various temperatures for (a) BFTO, (b) BGFTO, and (c) BNFTO. (d) Frequency dependence of the samples for σ_{ac} at temperature 260 °C.



Source: (SILVA *et al.*, 2021), Copyright ©2021, Springer Nature.

The Nyquist diagrams ($Z'' \times Z'$) to a temperature range of 260—370 °C for BFTO, BGFTO, and BNFTO are shown in Figure 22-(a–c). In general, this kind of analysis allows to indicate the contributions of grain, grain boundary, and electrode effect present in ceramic system. The shape, width and depreciation of the arcs demonstrate the possible relaxation mechanism type present in studied electroceramics (MACDONALD; JOHNSON, 2005). This behavior can be justified due to the inhomogeneity of the samples, differences between grain boundaries combined in series/parallel and even defects. In this case, non-Debye relaxation appears as alternatives to model for microstructural components of the ceramic (MAAROUFI *et al.*, 2016). From an equivalent circuit modeled on EIS Spectrum Analyser 1.0 (BONDARENKO; RAGOISHA, 2005), it was possible to obtain the best fit with two RC associations in parallel (Figure 22-(d)), where R is a resistor and C represents a constant phase element (CPE) with impedance given by Equation 3.9:

$$Z_{CPE} = (Qj\omega)^{-n} \quad (3.9)$$

where Q is a proportional factor and n is an empirical exponent with values between 0 and 1. This constant phase element approaches a fully resistive element if n approaches to zero and it is purely capacitive when n tends to 1 (MACDONALD; JOHNSON, 2005; MAAROUFI *et al.*, 2016; BONDARENKO; RAGOISHA, 2005). The equivalent impedance used in this work is given by Equation 3.10:

$$Z^* = \frac{R_g}{1 + R_g Q_g (j\omega)^{n_g}} + \frac{R_{gb}}{1 + R_{gb} Q_{gb} (j\omega)^{n_{gb}}} \quad (3.10)$$

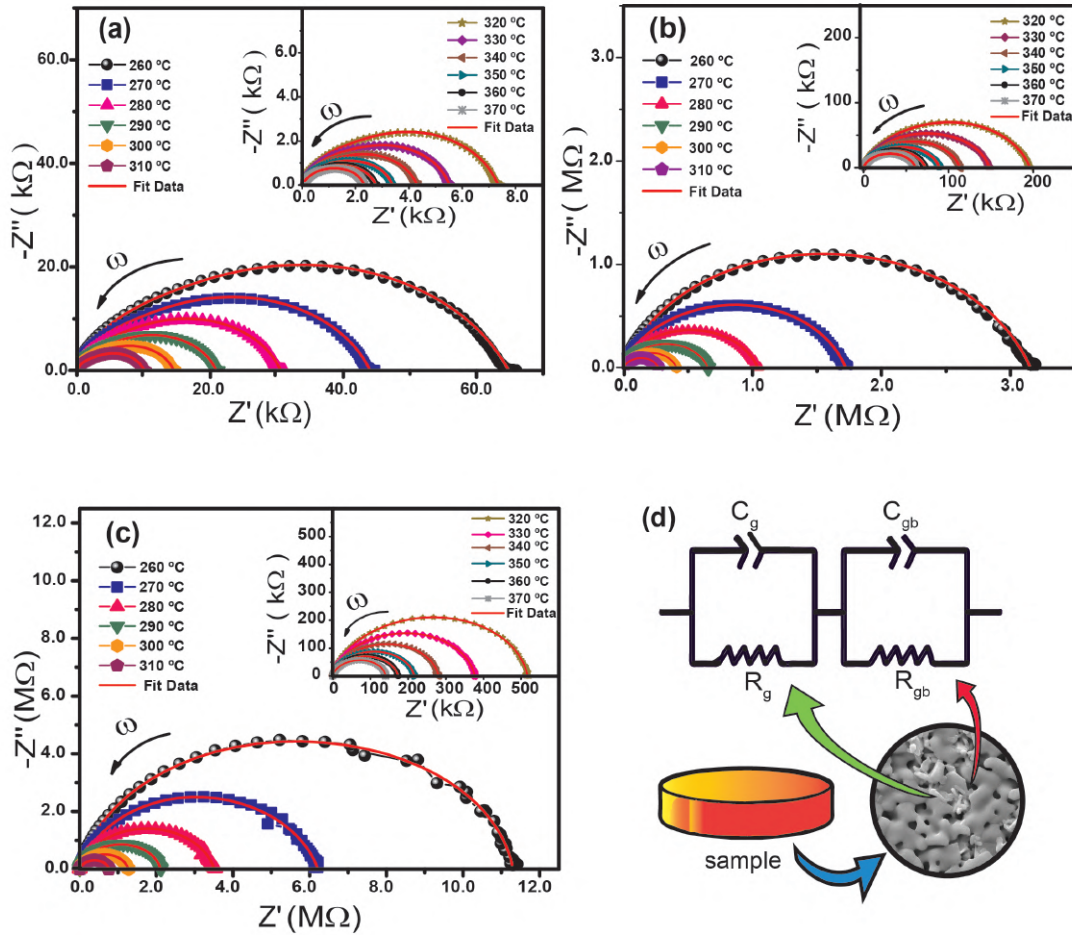
using the identity $j^n = (e^{j\pi/2})^n = \cos(n\pi/2) + j\sin(n\pi/2)$ and some algebraic manipulations, the real and imaginary part for the impedance can be written in terms of Equations 3.11 and 3.12:

$$Z' = \frac{R_g \left[1 + (\tau_g \omega)^{n_g} \cos\left(\frac{n_g \pi}{2}\right) \right]}{1 + 2(\tau_g \omega)^{n_g} \cos\left(\frac{n_g \pi}{2}\right) + (\tau_g \omega)^{2n_g}} + \frac{R_{gb} \left[1 + (\tau_{gb} \omega)^{n_{gb}} \cos\left(\frac{n_{gb} \pi}{2}\right) \right]}{1 + 2(\tau_{gb} \omega)^{n_{gb}} \cos\left(\frac{n_{gb} \pi}{2}\right) + (\tau_{gb} \omega)^{2n_{gb}}} \quad (3.11)$$

$$-Z'' = \frac{R_g \left[1 + (\tau_g \omega)^{n_g} \sin\left(\frac{n_g \pi}{2}\right) \right]}{1 + 2(\tau_g \omega)^{n_g} \cos\left(\frac{n_g \pi}{2}\right) + (\tau_g \omega)^{2n_g}} + \frac{R_{gb} \left[1 + (\tau_{gb} \omega)^{n_{gb}} \sin\left(\frac{n_{gb} \pi}{2}\right) \right]}{1 + 2(\tau_{gb} \omega)^{n_{gb}} \cos\left(\frac{n_{gb} \pi}{2}\right) + (\tau_{gb} \omega)^{2n_{gb}}} \quad (3.12)$$

where τ is the relaxation time, g and gb subscripts in the parameters R , C , and n , are associated with grain and grain boundary elements, respectively. Table 7 shows this adjusted parameter to several temperatures with residual error less than 2%.

Figure 22 – Nyquist diagrams for (a) BFTO, (b) BGFTO, and (c) BNFTO under various temperatures. (d) Equivalent circuit that best fitting the parameters of grain and grain boundaries.



Source: (SILVA *et al.*, 2021), Copyright ©2021, Springer Nature.

Both R_g and R_{gb} values for the three phases decrease with increasing temperature due to negative temperature coefficient resistance (NTCR) (THAKUR *et al.*, 2016). This indicates a semiconducting nature of the studied materials and suggests that the increase of the charge carriers mobility is added to the conduction process (OKASHA *et al.*, 2016).

The relaxation time values are larger for grain and grain boundaries of BGFTO and BNFTO than BFTO ceramic. This result is in accordance to that presented in Figure 20-(a–c), in which it is possible to see that the BFTO phase has a higher peak frequency (f_{max}) in comparison to the other phases. In this region of the spectrum, relaxation time being equal to the inverse of peak frequency. The tendency observed of the gradual decrease of τ_g and τ_{gb} , alongside the temperature rise, suggests an increase in long-range conductivity (JANGRA *et al.*, 2018). The τ

is an important parameter used in capacitors and is directly related to the stored energy and the efficiency corresponds to the change between the resistive and capacitive activities of the device (PANDIT *et al.*, 2019).

Table 7 – Temperature dependence for parameters adjusted from the Nyquist diagram ($Z'' \times Z'$) for grain and grain boundary of BFTO, BGFTO, and BNFTO samples.

	T (°C)	R_g (k Ω)	C_g (10^{-9})	n_g	τ_g (μ s)	R_{gb} (k Ω)	C_{gb} (10^{-9})	n_{gb}	τ_{gb} (μ s)
BFTO	260	58.936	3.895	0.751	14.378	5.881	0.289	0.997	1.652
	280	26.631	2.998	0.794	6.906	3.931	0.293	0.966	0.719
	300	12.547	3.244	0.799	3.203	1.967	0.253	0.976	0.350
	320	6.222	3.692	0.801	1.620	1.127	0.291	0.967	0.197
	340	3.536	4.561	0.795	0.950	0.774	0.636	0.920	0.140
	360	2.434	5.829	0.750	0.346	0.328	0.377	0.999	0.123
BGFTO	260	2617.50	0.727	0.782	335.14	537.250	0.547	0.904	124.39
	280	956.960	0.715	0.848	187.33	85.387	0.579	0.792	36.966
	300	326.670	0.824	0.821	45.170	84.744	0.769	0.852	12.375
	320	153.090	0.839	0.831	20.910	42.620	0.787	0.851	5.5490
	340	92.668	0.860	0.831	11.822	20.798	0.606	0.828	1.2130
	360	62.958	0.903	0.819	6.5750	9.915	0.465	0.819	0.3070
BNFTO	260	8419.30	1.304	0.954	8856.0	2885.60	0.275	0.876	291.64
	280	2142.70	0.965	0.847	679.79	1364.80	0.495	0.868	223.42
	300	766.570	0.700	0.909	253.11	496.610	0.491	0.848	55.113
	320	346.910	0.628	0.869	61.190	170.640	0.401	0.924	31.389
	340	191.620	0.643	0.867	31.117	89.6010	0.490	0.862	8.8310
	360	134.230	0.469	0.863	13.752	40.0630	0.883	0.873	5.8720

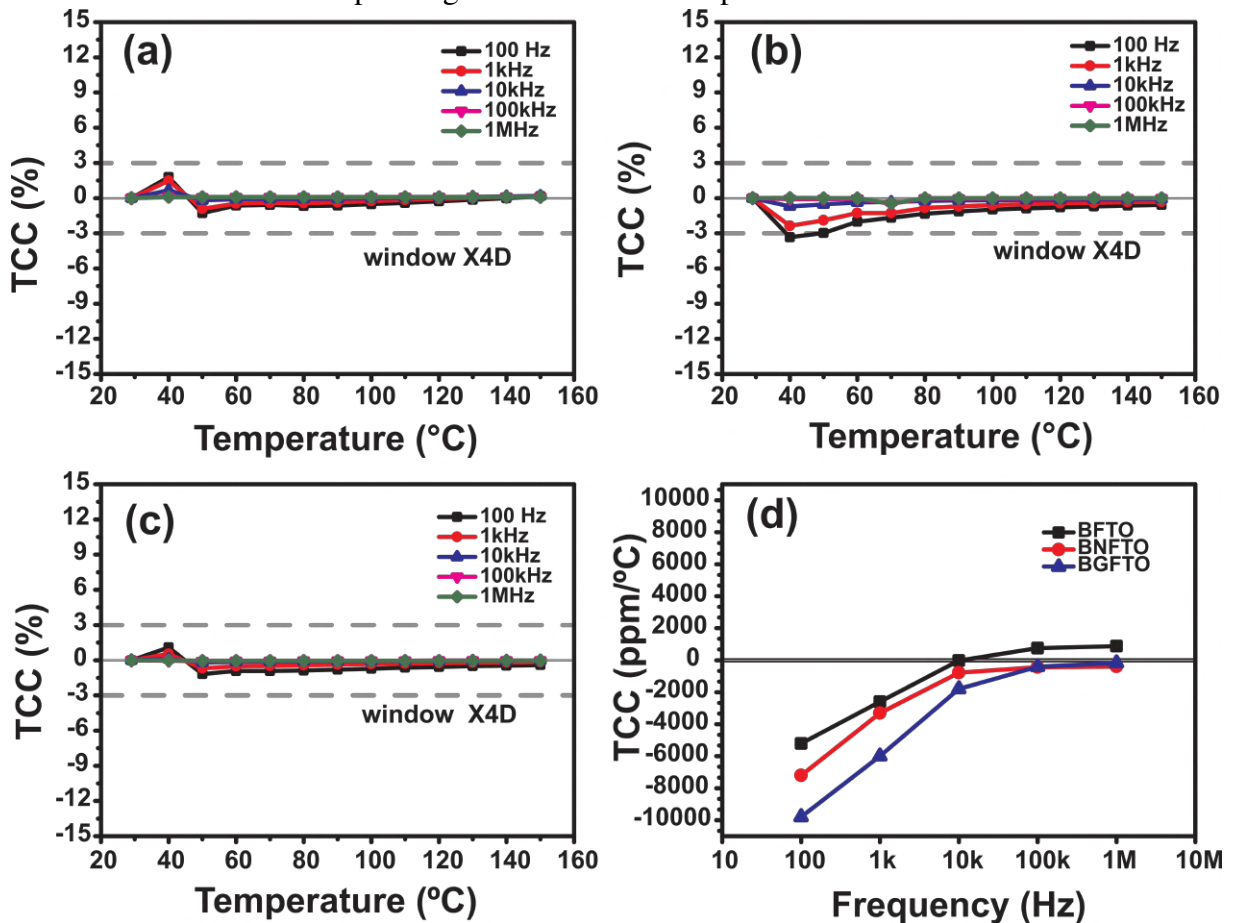
Source: (SILVA *et al.*, 2021), Copyright ©2021, Springer Nature.

The thermal stability test was performed from the temperature coefficient of capacitance (TCC). The values calculated via dielectric permittivity at 100 Hz, 1 kHz, 10 kHz, 100 kHz, and 1 MHz frequency, for the BFTO, BGFTO, and BNFTO ceramics, respectively, are shown in Figure 23-(a–c). This analysis was done under a range of 29–150 °C using Equation 3.1. The dotted horizontal lines show that the BFTO, BGFTO, and BNFTO phases present an interval that meets the requirements for X4D specification ($TCC \leq \pm 3.3\%$), according to EIA RS-198 (PAN; RANDALL, 2010). Figure 23-(d) shows the frequency dependence of TCC (ppm °C⁻¹) at a fixed temperature of 100 °C. At this temperature, the TCC is stable at 10 kHz.

The values of sintering temperature (T_s), ϵ , $\tan\delta$, and TCC (%) for all the samples and previous work are tabulated in Table 8. In comparison with reported X7R and X8R ceramics (WU *et al.*, 2021; MIAO *et al.*, 2017), Bi₃R₂Ti₃FeO₁₅ (R = Bi, Gd, and Nd) had a $\leq T_s$, a lower ϵ , approximated values of $\tan\delta$, and a better TCC, meeting the requirements of X4D specification. Compared to X4D (TCC with the same specification) (HAN *et al.*, 2020), had a lower ϵ and higher $\tan\delta$ values, and a lower T_s . The X4D capacitor is commonly used in

situations where dielectric specifications are required with greater temperature reliability, such as filtering, protection of gate turn-off thyristors and medium frequency tuning (HAN *et al.*, 2020; PAN; RANDALL, 2010).

Figure 23 – TCC as a function of temperature (29–150 °C) for (a) BFTO, (b) BGFTO, and (c) BNFTO under different frequency. (d) Variation of TCC for different frequencies. The dotted horizontal lines show the operating window for X4D capacitors.



Source: (SILVA *et al.*, 2021), Copyright ©2021, Springer Nature.

It is important to note that the ϵ and $\tan\delta$ parameters for the BGFTO and BNFTO in MW show a small change compared to the BFTO phase. This is compatible with the mentioned results above in the RF regime.

According to Ohsato (OHSATO *et al.*, 1998), the origin of ϵ values of ceramics materials can be understood by the difference of crystal structure and its dependence between ionic and covalent bonds. Covalent bonds reduce ϵ because the rattling effect of the cations in a polyhedron should be reduced due to the high bond strength. On the other hand, the BFTO, BGFTO, and BNFTO phases are titanates. Therefore, they are formed by Ti/FeO_6 octahedral framework, which is almost an ionic bond, and it has space for ionic displacement. In this case,

ϵ is sensitive to the effects of structural distortions already exposed in the discussion of the relaxation phenomenon. Furthermore, the relative density for BGFTO and BNFTO are lower than BFTO (see Table 6), and the low relative density (or high porosity) of ceramics samples affect the dielectric properties of the materials (BADGE; DESHPANDE, 2020; FUKUDA *et al.*, 1993).

Table 8 – Sintered temperature (T_S), dielectric properties in MW, and temperature coefficient of capacitance (TCC) with EIA specification for all samples and previous works.

Nominal formula	T_S (°C)	ϵ	$\tan\delta$	TCC (%)	(EIA)
$\text{Bi}_5\text{Ti}_3\text{FeO}_{15}$ (SILVA <i>et al.</i> , 2021)	1100	48.6 (RT)	0.0249	$\leq \pm 3.3$ (29 – 150 °C)	X4D
$\text{Bi}_3\text{Gd}_2\text{Ti}_3\text{FeO}_{15}$ (SILVA <i>et al.</i> , 2021)	1100	46.5 (RT)	0.0348	$\leq \pm 3.3$ (29 – 150 °C)	X4D
$\text{Bi}_3\text{Nd}_2\text{Ti}_3\text{FeO}_{15}$ (SILVA <i>et al.</i> , 2021)	1100	42.7 (RT)	0.0530	$\leq \pm 3.3$ (29 – 150 °C)	X4D
Rb/Nb co-subst $\text{Bi}_{0.5}\text{Na}_{0.5}\text{TiO}_3$ (WU <i>et al.</i> , 2021)	1100	> 800	≤ 0.050 (- 43– 292 °C)	$\leq \pm 10$	X7R
Y/Fe co-subst $\text{BaZr}_{0.13}\text{Ti}_{1.46}\text{O}_3$ (MIAO <i>et al.</i> , 2017)	1160	1443 (RT)	0.0335	$\leq \pm 15$ (- 55– 150 °C)	X8R
$(\text{Ba}_{1-x}\text{Ce}_x)(\text{Ti}_{1-x/2}\text{Mg}_{x/2})\text{O}_3$ (HAN <i>et al.</i> , 2020)	1450	~ 2242 (RT)	≤ 0.023	$\leq \pm 3.3$ (-55 – 65 °C)	X4D

Source: (SILVA *et al.*, 2021), Copyright ©2021, Springer Nature.

3.3.3 Performance of BLSF Materials as CDRA

The measurements of the real and imaginary impedance (in MW regime) are shown in Figure 24-(a–c) for BFTO, BGFTO and BNFTO, respectively. The experimental and numerical simulations exhibit a good agreement, considering that the errors are $< 10\%$ for all parameters. This gauge is necessary for the accurate acquisition of the far-field region of an antenna. For all samples, the resonant frequency showed resistance values close to 50Ω . This is important for an antenna to work efficiently because there must be an adequate impedance match between the antenna and its feed.

The S_{11} spectrum for all samples is shown in Figure 24-(d). A shift from the

minimum of S_{11} to higher frequencies is observed in the phases containing REs. This can be justified due to the decrease in ϵ (see Equation 3.3). The inset shows the schematic setup used in CDRA measurements (detailed in section 3.2) and radiation pattern. The profile shows a maximum radiation for $\theta = 0^\circ$ when analyzed by $\phi = 90^\circ$ and $\phi = 0^\circ$, which is compatible with CDRA. The performance parameters f_0 , S_{11} , BW , D , G , η , and τ_f for all the samples and previous work (with CDRA geometry) are presented in the Table 9. From the operation frequency f_0 , these materials present frequencies between 2.787 and 2.976 GHz, and are great candidates for applications on devices that operate in the S-band. According to Institute of Electrical and Electronics Engineers (IEEE), the S-band has a frequency range from 2 to 4 GHz. This band is mostly used for mobile communications, mobile satellite communications and weather/ship radar systems (see Figure 10) (ISLAM *et al.*, 2021).

Table 9 – Antenna parameters and percent error for all samples and previous works.

Nominal formula		f_0 (GHz)	S_{11} (dB)	BW (%)	D (dBi)	G (dBi)	η (%)	τ_f ppm/ $^\circ\text{C}$
Bi ₅ Ti ₃ FeO ₁₅ (1)	Exp.	2.787	- 36.21	3.946	5.19	2.98	60.13	- 428.48
	Sim.	2.786	- 35.05	3.574				
	Error (%)	0.035	3.203	9.427				
Bi ₃ Gd ₂ Ti ₃ FeO ₁₅ (1)	Exp.	2.871	- 22.51	4.391	5.26	1.73	44.39	+ 59.17
	Sim.	2.872	- 21.57	4.516				
	Error (%)	0.034	4.175	2.846				
Bi ₃ Nd ₂ Ti ₃ FeO ₁₅ (1)	Exp.	2.976	- 31.65	2.752	5.21	2.47	53.10	+ 57.69
	Sim.	2.978	- 30.32	2.810				
	Error (%)	0.067	4.202	2.107				
BaBi ₄ Ti ₄ O ₁₅ (2)	Exp.	2.2652	- 29.578	3.929	3.45	1.12	32.51	- 422.11
	Sim.	2.2650	- 29.584	3.955				
	Error (%)	0.0100	0.020	0.670				
BiVO ₄ (3)	Exp.	2.690	~ - 40.00	1.252	N/A	5.85	92.65	- 244.00
	Sim.	2.690	N/A	1.220				
	Error (%)	0.000	N/A	2.510				
SrBi ₄ Ti ₄ O ₁₅ (4)	Exp.	2.0233	- 43.95	1.80	2.53	1.78	70.00	- 178.77
	Sim.	2.0230	- 42.63	1.73				
	Error (%)	0.0100	3.00	3.88				

⁽¹⁾ (SILVA *et al.*, 2021), ⁽²⁾ (SILVA *et al.*, 2014), ⁽³⁾ (OLIVEIRA *et al.*, 2019), ⁽⁴⁾ (JUNIOR *et al.*, 2018)

Source: (SILVA *et al.*, 2021), Copyright ©2021, Springer Nature.

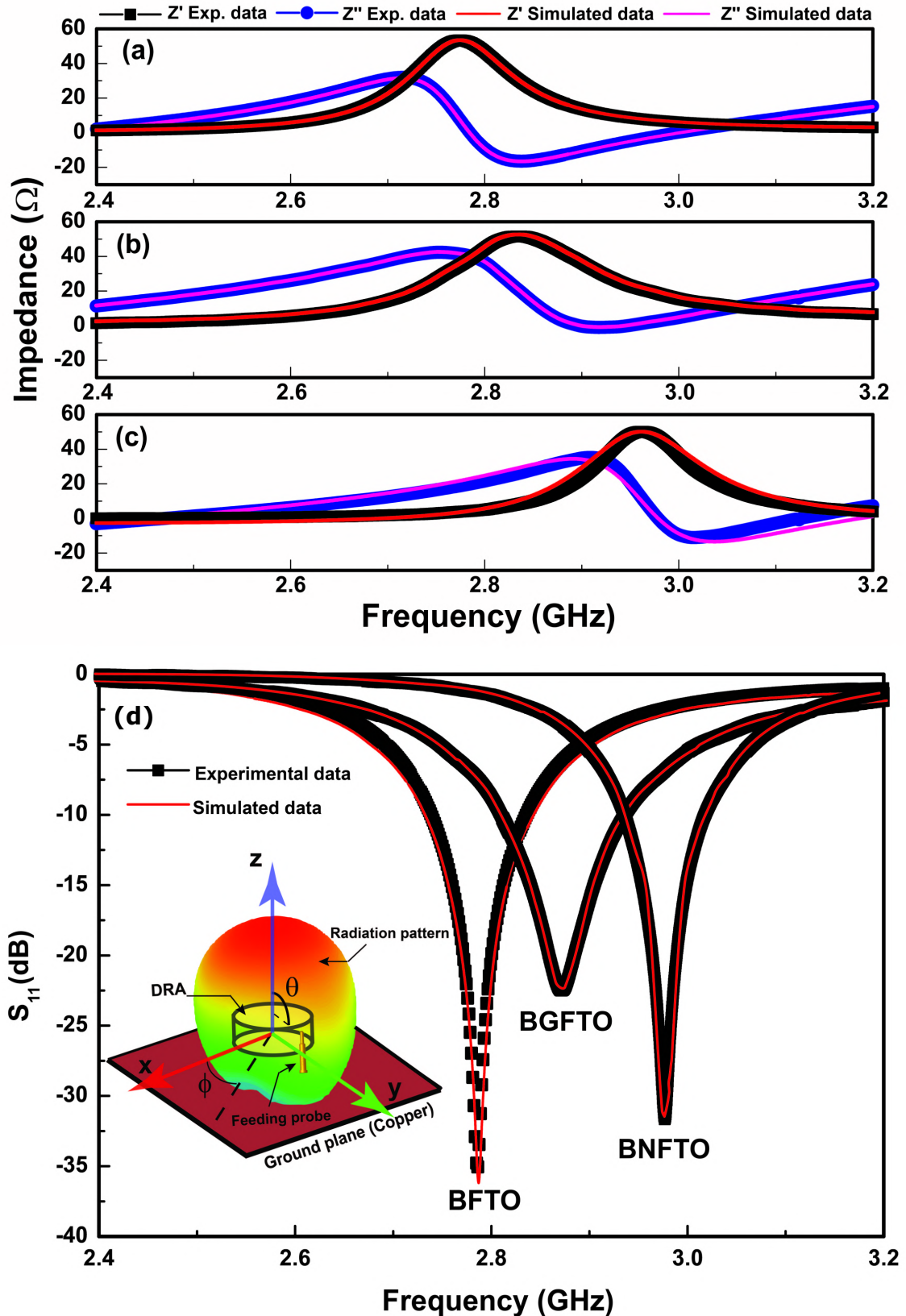
All the CDRA exhibited reflection coefficient values below - 10 dB, which is an important result for the functionality of an antenna. The BFTO and BGFTO phases present BW and D greater than BNFTO and the other tabulated phases (SILVA *et al.*, 2014; OLIVEIRA *et al.*, 2019; JUNIOR *et al.*, 2018). The BFTO sample showed higher G compared to BGFTO and BNFTO. This was already expected due to the better impedance matching. BFTO had a better G value, when compared to reported $\text{BaBi}_4\text{Ti}_4\text{O}_{15}$ (SILVA *et al.*, 2014) and $\text{SrBi}_4\text{Ti}_4\text{O}_{15}$ (JUNIOR *et al.*, 2018) ceramics. However, it is overcome by BiVO_4 (OLIVEIRA *et al.*, 2019). In terms of η , $\text{Bi}_3\text{R}_2\text{Ti}_3\text{FeO}_{15}$ (R = Bi, Gd, and Nd) shows better efficiency than $\text{BaBi}_4\text{Ti}_4\text{O}_{15}$ (SILVA *et al.*, 2014), but it is below the achieved values to BiVO_4 (OLIVEIRA *et al.*, 2019) and $\text{SrBi}_4\text{Ti}_4\text{O}_{15}$ (JUNIOR *et al.*, 2018).

For thermal stability of the resonant frequency (τ_f), BFTO phase presents $\tau_f = -428.48 \text{ ppm } ^\circ\text{C}^{-1}$, which is very close to $\text{BaBi}_4\text{Ti}_4\text{O}_{15}$ ($-422.11 \text{ ppm } ^\circ\text{C}^{-1}$). On the other hand, a change is observed for phases containing REs: BGFTO ($+59.17 \text{ ppm } ^\circ\text{C}^{-1}$) and BNFTO ($+57.69 \text{ ppm } ^\circ\text{C}^{-1}$).

The origin of τ_f is related to the linear expansion coefficient and its dielectric constant variation with temperature (WANG; CHEN, 2021). Furthermore, all phases have very similar dimensions and were subjected to the same temperature conditions, so the effects of dimensional variations, in terms of comparison, can be neglected. Several authors studied (PARIDA *et al.*, 2015; JI *et al.*, 2021b; WANG *et al.*, 2020) the effect of difference in ionic radius in ϵ , quality factor (inverse of $\tan\delta$), and τ_f . Therefore, it is acceptable that the effects of distortion in the lattice parameters of the perovskite layers and the difference in relative density (or porosity) contributes to the difference in τ_f values.

However, this difference opens up a great opportunity for future work. From the practical application, dielectric materials should possess a near-zero temperature coefficient of resonant frequency ($\tau_f \sim 0$) for thermally stable electronic devices. This result can be achieved through methods well established in the literature, such as mixed two phases with negative and positive temperature coefficients (JI *et al.*, 2021b) and/or tuning of τ_f values by doping effect in the main matrix (WANG *et al.*, 2020).

Figure 24 – Plot of simulated and experimental data impedance of CDRA for (a) BFTO, (b) BGFTO, and (c) BNFTO. (d) Reflection coefficient S_{11} for CDRA from experimental data and numerical simulation). Inset shows the typical radiation profile and schematic setup used in CDRA measurements.



3.4 Conclusions

In this work, the dielectric properties of BLSF $\text{Bi}_3\text{R}_2\text{Ti}_3\text{FeO}_{15}$ (R = Bi, Gd, and Nd) at MW and RF are investigated. The morphological analysis by SEM, shown a typical plate-like morphology to BFTO phase. A modification in the texture and average grain size occurs with the replacement of rare earth elements. This can be justified due to difference in concentration of oxygen vacancies, bond dissociation energy and crystallite size.

To low frequencies (10 kHz) and MW regime, both in room temperature, BGFTO and BNFTO show a decrease in dielectric characteristics compared to BFTO. This can be explained by structural distortion resulting from the replacement of lanthanides in the cations of A-site in the perovskite layer.

The same relaxation induced by a thermally activated mechanism can be observed in all samples. The activation energy of the materials both for the relaxation process and the conduction process found in the range of 0.6–0.9 eV indicates the association of doubly ionized oxygen vacancy in these processes. The Nyquist plot and conductivity studies showed that all samples have NTCR characteristics. The frequency-dependent ac conductivity follows the universal power law. The rare-earth substituted samples exhibit substantially low conductivity as compared to the parent BFTO. Probably due to the low density and the difference in the amount of oxygen vacancy.

The temperature stability of dielectric properties for all samples met the requirements of capacitors X4D specification. Besides that, the $\text{Bi}_3\text{R}_2\text{Ti}_3\text{FeO}_{15}$ -based CDRA showed great potential for microwave antenna application operating in the S-band. A change is observed to τ_f of BFTO phase ($-428.48 \text{ ppm}^\circ\text{C}^{-1}$) to BGFTO ($+59.17 \text{ ppm}^\circ\text{C}^{-1}$) and BNFTO ($+57.69 \text{ ppm}^\circ\text{C}^{-1}$). This result opens up a great opportunity for future work in CDRA with near-zero temperature coefficients ($\tau_f \sim 0$).

4 GENERAL CONCLUSIONS

It was shown in this work the synthesis, characterization and application of the Bismuth Layer-Structured Ferroelectric Materials $\text{Bi}_3\text{R}_2\text{Ti}_3\text{FeO}_{15}$ ($\text{R} = \text{Bi}, \text{Nd}, \text{and Gd}$). The samples were obtained through the solid-state reaction. These materials were applied to ceramic capacitors and dielectric resonator antenna (DRA), and were thoroughly characterized concerning their structural, vibrational, morphological, electrical, and magnetic properties. These properties, and their relationship with the changes caused by the introduction of rare earth ions in the crystalline structure of materials, help us to understand the processes that can affect the final properties of ceramics and the respective devices where they are applied.

In the study of the characterization of ceramic materials, all the samples showed an orthorhombic structure with $A2_1am$ space group. $\text{Bi}_3\text{Nd}_2\text{Ti}_3\text{FeO}_{15}$ (BNFTO) and $\text{Bi}_3\text{Gd}_2\text{Ti}_3\text{FeO}_{15}$ (BGFTO) presented a reduction in the orthorhombicity when compared to $\text{Bi}_5\text{Ti}_3\text{FeO}_{15}$ (BFTO). For the Raman analysis, significant changes observed in the intensity of some modes, as well as the shift of modes to higher frequencies, occurred due to the replacement of Bi atoms in the perovskite layers by the lighter Gd and Nd atoms. The magnetic susceptibility of all samples followed the Curie–Weiss law, with negative values of the Curie–Weiss temperature, demonstrating that the magnetic interactions are antiferromagnetic in nature. The magnetization curves suggested a weak canted ferromagnetic behavior for temperatures below 25 K, followed by a linear behavior in the curves at high temperatures. Mössbauer spectroscopy measurements revealed an increase of the quadrupole splitting values as the temperature decreases, indicating that the samples present local distortions, favoring the existence of weak ferromagnetic phase via the antisymmetric Dzyaloshinskii–Moriya interaction. This can be explained by structural distortion resulting from the replacement of lanthanides in the cations of A-site in the perovskite layer.

In application character, their morphology and dielectric properties were investigated. The BGFTO and BNFTO samples, show a decrease in dielectric characteristics compared to BFTO. Impedance spectroscopy was performed to establish a correlation between the electrical properties and the microstructure of the ceramics. A non-Debye relaxation induced by a thermally activated mechanism can be observed in all samples. The activation energy of the materials found in the range of 0.6–0.9 eV and indicates the association of doubly ionized oxygen vacancy. We show that the three ceramic phases BFTO, BGFTO, and BNFTO present promising results to compose this select group of ceramic capacitors. With excellent temperature stability (29–150

$^{\circ}\text{C}$, $\text{TCC} \leq \pm 3.3\%$). These characteristics are from an X4D type capacitor. Belonging to class II, the research and development of these capacitors has been gaining strength in the electronics industry. In addition, the electroceramics were used to design a cylindrical dielectric resonator antenna (CDRA) for microwave applications. A change is observed to τ_f of BFTO phase ($-428.48 \text{ ppm } ^{\circ}\text{C}^{-1}$) to BGFTO ($+59.17 \text{ ppm } ^{\circ}\text{C}^{-1}$) and BNFTO ($+57.69 \text{ ppm } ^{\circ}\text{C}^{-1}$). This result opens up a great opportunity for future work in CDRA with near-zero temperature coefficients ($\tau_f \sim 0$). The $\text{Bi}_3\text{R}_2\text{Ti}_3\text{FeO}_{15}$ -based CDRA showed great potential for microwave antenna application operating in the S-band. This band is mostly used for mobile communications, mobile satellite communications and weather/ship radar systems.

The results presented in this work aim to contribute in a wide area of electronic devices and ceramic dielectrics, helping readers and their future works about dielectric, electrical, and magnetic properties. To contribute in BLSF materials study, arising from its structural versatility and multifunctionality in MW and RF regime. Besides, it was suggested ways to improve the different materials obtained, in order to present comparable results to state-of-the-art materials.

BIBLIOGRAPHY

AGUIAR, F.; SALES, A.; ARAÚJO, B.; SABÓIA, K.; FILHO, M. C.; SOMBRA, A.; AYALA, A.; FECHINE, P. Effect of V_2O_5 addition on the phase composition of $Bi_5FeTi_3O_{15}$ ceramic and RF/Microwave dielectric properties. **Journal of Electronic Materials**, v. 46, n. 4, p. 2467–2475, 2017.

ALI, M.; GUZMÁN, R. C.; COJOCARI, O.; NELLEN, S.; SANTAMARÍA, G.; GARCÍA-MUÑOZ, L. E.; SEGOVIA-VARGAS, D.; GLOBISCH, B.; CARPINTERO, G. Quasi-optic transmitter and receiver modules enabling next-generation ultra-broadband wireless links at carrier-wave frequencies ranging from 60 to 180 GHz. **Journal of Infrared, Millimeter, and Terahertz Waves**, v. 40, n. 6, p. 688–695, 2019.

ANDO, A.; SAWADA, T.; OGAWA, H.; KIMURA, M.; SAKABE, Y. Fine-tolerance resonator applications of bismuth-layer-structured ferroelectric ceramics. **Japanese journal of applied physics**, v. 41, n. 11S, p. 7057–7061, 2002.

ARANDA, M. D. C. R.; RODRÍGUEZ-VÁZQUEZ, Á. G.; SALAZAR-KURI, U.; MENDOZA, M. E.; NAVARRO-CONTRERAS, H. R. Raman effect in multiferroic $Bi_5Fe_{1+x}Ti_{3-x}O_{15}$ solid solutions: A temperature study. **Journal of Applied Physics**, v. 123, n. 8, p. 0841011–0841018, 2018.

ARMSTRONG, R.; NEWNHAM, R. Bismuth titanate solid solutions. **Materials Research Bulletin**, v. 7, n. 10, p. 1025–1034, 1972.

AROYO, M. I.; KIROV, A.; CAPILLAS, C.; PEREZ-MATO, J.; WONDRATSCHEK, H. Bilbao crystallographic server. II. representations of crystallographic point groups and space groups. **Acta Crystallographica Section A: Foundations of Crystallography**, v. 62, n. 2, p. 115–128, 2006.

AROYO, M. I.; PEREZ-MATO, J.; OROBENGOA, D.; TASCI, E.; FLOR, G. de la; KIROV, A. Crystallography online: Bilbao crystallographic server. **Bulg. Chem. Commun**, v. 43, n. 2, p. 183–197, 2011.

AROYO, M. I.; PEREZ-MATO, J. M.; CAPILLAS, C.; KROUMOVA, E.; IVANTCHEV, S.; MADARIAGA, G.; KIROV, A.; WONDRATSCHEK, H. Bilbao crystallographic server: I. databases and crystallographic computing programs. **Zeitschrift für Kristallographie-Crystalline Materials**, v. 221, n. 1, p. 15–27, 2006.

AURIVILLIUS, B. Mixed bismuth oxides with layer lattices I. The structure type of $CaNb_2Bi_2O_9$. **Arkiv kemi**, v. 1, p. 463–480, 1949.

BADGE, S. K.; DESHPANDE, A. La^{3+} modified bismuth titanate (BLT) prepared by sol–gel synthesis: structural, dielectric, impedance and ferroelectric studies. **Solid State Ionics**, v. 347, p. 1152701–1152709, 2020.

BADOLE, M.; DWIVEDI, S.; PAREEK, T.; AHMED, S. A.; KUMAR, S. Significantly improved dielectric and piezoelectric properties of $BiAlO_3$ modified potassium bismuth titanate lead-free ceramics. **Materials Science and Engineering: B**, v. 262, p. 1147491–1147499, 2020.

- BASILE, V.; GRANDE, M.; MARROCCO, V.; LANEVE, D.; PETRIGNANI, S.; PRUDENZANO, F.; FASSI, I. Design and manufacturing of super-shaped dielectric resonator antennas for 5G applications using stereolithography. **IEEE Access**, v. 8, p. 82929–82937, 2020.
- BEHARA, S.; GHATTI, L.; KANTHAMANI, S.; DUMPALA, M.; THOMAS, T. Structural, optical, and raman studies of Gd doped sodium bismuth titanate. **Ceramics International**, v. 44, n. 11, p. 12118–12124, 2018.
- BIJUMON, P. V.; SEBASTIAN, M. T. Temperature-stable microwave dielectric ceramics in the $\text{Ca}_5\text{A}_2\text{Ti}_{1-x}\text{Zr}_x\text{O}_{12}$ (A= Nb, Ta) system. **Journal of materials research**, v. 19, n. 10, p. 2922–2928, 2004.
- BIRENBAUM, A. Y.; EDERER, C. Potentially multiferroic aurivillius phase $\text{Bi}_5\text{FeTi}_3\text{O}_{15}$: Cation site preference, electric polarization, and magnetic coupling from first principles. **Physical Review B**, v. 90, n. 21, p. 214109–21410912, 2014.
- BLADEL, J. V. On the resonances of a dielectric resonator of very high permittivity. **IEEE Transactions on Microwave Theory and Techniques**, v. 23, n. 2, p. 199–208, 1975.
- BOBIĆ, J.; KATILIUTE, R.; IVANOV, M.; PETROVIĆ, M. V.; ILIĆ, N.; DŽUNUZOVIĆ, A.; BANYS, J.; STOJANOVIĆ, B. Dielectric, ferroelectric and magnetic properties of La doped $\text{Bi}_5\text{Ti}_3\text{FeO}_{15}$ ceramics. **Journal of Materials Science: Materials in Electronics**, v. 27, n. 3, p. 2448–2454, 2016.
- BONDARENKO, A.; RAGOISHA, G. In: POMERANTSEV, A. L. (Ed.). **Progress in chemometrics research**. New York: Nova Science Publishers, 2005. p. 89–102. (the program is available online at <http://www.abc.chemistry.bsu.by/vi/analyser/>).
- BRAUN, H. P.; MEHMOOD, A.; HOVHANNISYAN, M.; ZHANG, H.; HEIDARY, D. S. B.; RANDALL, C.; LANAGAN, M. T.; JAKOBY, R.; REANEY, I. M.; LETZ, M. *et al.* Microwave properties and structure of La–Ti–Si–B–O glass-ceramics for applications in GHz electronics. **Journal of the European Ceramic Society**, v. 37, n. 5, p. 2137–2142, 2017.
- BRUDER, J.; CARLO, J.; GURNEY, J.; GORMAN, J. Ieee standard for letter designations for radar-frequency bands. **IEEE Aerospace & Electronic Systems Society**, p. 1–3, 2003.
- CALLISTER, W. D.; RETHWISCH, D. G. **Materials science and engineering: an introduction**. [S. l.]: Wiley New York, 2018. v. 9.
- CAO, B.; WANG, H.; HUANG, Y.; WANG, J.; XU, H. A novel antenna-in-package with LTCC technology for W-band application. **IEEE Antennas and Wireless propagation letters**, v. 13, p. 357–360, 2014.
- CHEN, C.; SONG, K.; BAI, W.; YANG, J.; ZHANG, Y.; XIANG, P.; QIN, M.; TANG, X.; CHU, J. Effect of Nb and more Fe ions co-doping on the microstructures, magnetic, and piezoelectric properties of aurivillius $\text{Bi}_5\text{Ti}_3\text{FeO}_{15}$ phases. **Journal of Applied Physics**, v. 120, n. 21, p. 2141041–2141048, 2016.
- CHEN, L.-F.; ONG, C.; NEO, C.; VARADAN, V.; VARADAN, V. K. **Microwave electronics: measurement and materials characterization**. [S. l.]: John Wiley & Sons, 2004.

- CHEN, X.; HUANG, F.; LU, Z.; XUE, Y.; MIN, J.; LI, J.; XIAO, J.; YANG, F.; ZENG, X. Influence of transition metal doping (X= Mn, Fe, Co, Ni) on the structure and bandgap of ferroelectric $\text{Bi}_{3.15}\text{Nd}_{0.85}\text{Ti}_2\text{X}_1\text{O}_{12}$. **Journal of Physics D: Applied Physics**, v. 50, n. 10, p. 1051041–1051045, 2017.
- CHEN, Y.; ZHANG, C.-C.; QIN, L.; JIANG, C.-B.; LIU, K.-H.; MA, C.; WU, Z.-T.; PAN, R.-K.; CAO, W.-Q.; YE, C. *et al.* Enhanced dielectric and piezoelectric properties in $\text{Na}_{0.5}\text{Bi}_{4.5}\text{Ti}_4\text{O}_{15}$ ceramics with Pr-doping. **Ceramics International**, v. 44, n. 15, p. 18264–18270, 2018.
- CHEN, Y.-C.; HSIUNG, C.-P.; CHEN, C.-Y.; GAN, J.-Y.; SUN, Y.-M.; LIN, C.-P. Crystallinity and electrical properties of neodymium-substituted bismuth titanate thin films. **Thin Solid Films**, v. 513, n. 1, p. 331–337, 2006.
- CHU, P. Y.; JONES, R. E.; ZURCHER, P.; TAYLOR, D. J.; JIANG, B.; GILLESPIE, S. J.; LIU, Y.; KOTTKE, M.; FEJES, P.; CHEN, W. Characteristics of spin-on ferroelectric $\text{SrBi}_2\text{Ta}_2\text{O}_9$ thin film capacitors for ferroelectric random access memory applications. **Journal of materials research**, v. 11, n. 5, p. 1065–1068, 1996.
- COELHO, A. A. TOPAS and TOPAS-academic: an optimization program integrating computer algebra and crystallographic objects written in C++. **Journal of Applied Crystallography**, v. 51, n. 1, p. 210–218, 2018.
- CULLITY, B. D.; GRAHAM, C. D. **Introduction to magnetic materials**. [S. l.]: John Wiley & Sons, 2011.
- DEDECKER, K.; GRANCINI, G. Dealing with lead in hybrid perovskite: A challenge to tackle for a bright future of this technology? **Advanced Energy Materials**, v. 10, n. 31, p. 20014711–20014718, 2020.
- DIAS, J. A.; BRETAS, R. E. S.; MARCONDES, L. M. S.; MORELLI, M. R. Optical and dielectric properties of Nd and Sm-doped $\text{Bi}_5\text{FeTi}_3\text{O}_{15}$. **Journal of Materials Science: Materials in Electronics**, v. 30, n. 18, p. 16812–16820, 2019.
- DICKIE, R.; CHRISTIE, S.; CAHILL, R.; BAINE, P.; FUSCO, V.; PAROW-SOUCHON, K.; HENRY, M.; HUGGARD, P. G.; DONNAN, R. S.; SUSHKO, O. *et al.* Low-pass FSS for 50-230 GHz quasi-optical demultiplexing for the MetOp second-generation microwave sounder instrument. **IEEE Transactions on antennas and propagation**, v. 65, n. 10, p. 5312–5321, 2017.
- DING, Y. R.; CHENG, Y. J.; SUN, J. X.; WANG, L.; LI, T. J. Dual-band shared-aperture two-dimensional phased array antenna with wide bandwidth of 25.0% and 11.4% at Ku-and Ka-band. **IEEE Transactions on Antennas and Propagation**, p. 7468–7477, 2022.
- DING, Z.; TANG, X.; REN, J.; LIU, X.; CHEN, Y.; XIA, Z.; CAO, L.; CHEN, X.; YANG, F. Tuning the band gaps of ferroelectric aurivillius compounds by transition metal substitution. **Ceramics International**, v. 46, n. 6, p. 8314–8319, 2020.
- DION, M.; GANNE, M.; TOURNOUX, M. Nouvelles familles de phases $M^I M^{II} \text{ }_2\text{Nb}_3\text{O}_{10}$ a feuillets “perovskites”. **Materials research bulletin**, v. 16, n. 11, p. 1429–1435, 1981.
- DJANI, H.; HERMET, P.; GHOSEZ, P. First-principles characterization of the $\text{P2}_1\text{ab}$ ferroelectric phase of aurivillius Bi_2WO_6 . **The Journal of Physical Chemistry C**, v. 118, n. 25, p. 13514–13524, 2014.

DONG, X.; WANG, K.; WAN, J.; ZHU, J.; LIU, J.-M. Magnetocapacitance of polycrystalline $\text{Bi}_5\text{Ti}_3\text{FeO}_{15}$ prepared by sol-gel method. **Journal of Applied Physics**, v. 103, n. 9, p. 0941011–0941015, 2008.

DURBHAKULA, M. K. C.; AOUTHU, S. Compact multi frequency antenna for Ku band applications. **Materials Today: Proceedings**, p. 1–7, 2020.

ERICSSON. Ericsson mobility report. 2021. (Available at <https://www.ericsson.com/en/reports-and-papers/mobility-report/reports/november-2021>. Accessed 25 Jan 2022).

FARAZ, A.; DEEPAK, N.; SCHMIDT, M.; PEMBLE, M. E.; KEENEY, L. A study of the temperature dependence of the local ferroelectric properties of c-axis oriented $\text{Bi}_6\text{Ti}_3\text{Fe}_2\text{O}_{18}$ aurivillius phase thin films: Illustrating the potential of a novel lead-free perovskite material for high density memory applications. **AIP advances**, v. 5, n. 8, p. 0871231–08712315, 2015.

FERREIRA, W. C.; RODRIGUES, G. L. C.; ARAUJO, B. S.; AGUIAR, F. A. A. de; SILVA, A. N. A. de A.; FECHINE, P. B. A.; PASCHOAL, C. W. de A.; AYALA, A. P. Pressure-induced structural phase transitions in the multiferroic four-layer aurivillius ceramic $\text{Bi}_5\text{FeTi}_3\text{O}_{15}$. **Ceramics International**, v. 46, n. 11, p. 18056–18062, 2020.

FUKUDA, K.; KITOH, R.; AWAI, I. Microwave characteristics of $\text{TiO}_2\text{-Bi}_2\text{O}_3$ dielectric resonator. **Japanese journal of applied physics**, v. 32, n. 10R, p. 4584–4588, 1993.

GAO, X.; LI, L.; ZHANG, D.; WANG, X.; JIAN, J.; HE, Z.; WANG, H. Novel layered $\text{Bi}_3\text{MoM}_7\text{O}_9$ ($M = \text{Mn, Fe, Co}$ and Ni) thin films with tunable multifunctionalities. **Nanoscale**, v. 12, n. 10, p. 5914–5921, 2020.

GARCÍA-GUADERRAMA, M.; ARIZAGA, G. G. C.; DURÁN, A. Effect of synthesis conditions on the morphology and crystal structure of biferroic $\text{Bi}_5\text{Ti}_3\text{FeO}_{15}$. **Ceramics International**, v. 40, n. 5, p. 7459–7465, 2014.

GARCIA-GUADERRAMA, M.; FUENTES, L.; MONTERO-CABRERA, M.; MARQUEZ-LUCERO, A.; VILLAFUERTE-CASTREJON, M. Molten salt synthesis and crystal structure of $\text{Bi}_5\text{Ti}_3\text{FeO}_{15}$. **Integrated Ferroelectrics**, v. 71, n. 1, p. 233–239, 2005.

GRAVES, P.; HUA, G.; MYHRA, S.; THOMPSON, J. The raman modes of the aurivillius phases: temperature and polarization dependence. **Journal of Solid State Chemistry**, v. 114, n. 1, p. 112–122, 1995.

GU, C.; BAI, L. Study of 140 GHz waveguide fed lenses with different dielectric constant. In: IEEE. **2021 IEEE Microwave Theory and Techniques in Wireless Communications (MTTW)**. [S. l.], 2021. p. 258–262.

GUO, L.; SHI, M.; FU, J.; XU, Y.; ZUO, R.; ZHAO, Z.; SI, Z.; HU, K.; MEN, E. Ferroelectric and photoluminescent properties of Eu^{3+} -doped $\text{Bi}_4\text{Ti}_3\text{O}_{12}$ films prepared via the spin-coating method. **Journal of Materials Science: Materials in Electronics**, v. 31, n. 8, p. 6339–6348, 2020.

GUPTA, P.; MAHAPATRA, P.; CHOUDHARY, R. Structural and electrical characteristics of rare-earth modified bismuth layer structured compounds. **Journal of Alloys and Compounds**, v. 863, p. 1584571–15845716, 2021.

- HAKKI, B.; COLEMAN, P. D. A dielectric resonator method of measuring inductive capacities in the millimeter range. **IRE Transactions on Microwave theory and techniques**, v. 8, n. 4, p. 402–410, 1960.
- HAN, D.; WANG, C.; LU, D.; HUSSAIN, F.; WANG, D.; MENG, F. A temperature stable $(\text{Ba}_{1-x}\text{Ce}_x)(\text{Ti}_{1-x/2}\text{Mg}_{x/2})\text{O}_3$ lead-free ceramic for X4D capacitors. **Journal of Alloys and Compounds**, v. 821, p. 1534801–1534806, 2020.
- HEIMANN, R. B. **Classic and advanced ceramics: from fundamentals to applications**. [S. l.]: John Wiley & Sons, 2010.
- HERVOCHES, C. H.; SNEDDEN, A.; RIGGS, R.; KILCOYNE, S. H.; MANUEL, P.; LIGHTFOOT, P. Structural behavior of the four-layer aurivillius-phase ferroelectrics $\text{SrBi}_4\text{Ti}_4\text{O}_{15}$ and $\text{Bi}_5\text{Ti}_3\text{FeO}_{15}$. **Journal of Solid State Chemistry**, v. 164, n. 2, p. 280–291, 2002.
- HONG, K.; LEE, T. H.; SUH, J. M.; YOON, S.-H.; JANG, H. W. Perspectives and challenges in multilayer ceramic capacitors for next generation electronics. **Journal of Materials Chemistry C**, v. 7, n. 32, p. 9782–9802, 2019.
- HORN, J. A.; ZHANG, S.; SELVARAJ, U.; MESSING, G. L.; TROLIER-MCKINSTRY, S. Templated grain growth of textured bismuth titanate. **Journal of the American Ceramic Society**, v. 82, n. 4, p. 921–926, 1999.
- HUANG, Z.; WANG, G.-S.; LI, Y.-C.; LIANG, R.-H.; CAO, F.; DONG, X.-L. Electrical properties of (Na, Ce) doped $\text{Bi}_5\text{Ti}_3\text{FeO}_{15}$ ceramics. **physica status solidi (a)**, v. 208, n. 5, p. 1047–1051, 2011.
- HUITEMA, L.; MONÉDIÈRE, T. Dielectric materials for compact dielectric resonator antenna applications. **Dielectric Material**, v. 2, p. 28–58, 2012.
- IMBERT, M.; ROMEU, J.; BAQUERO-ESCUADERO, M.; MARTINEZ-INGLES, M.-T.; MOLINA-GARCIA-PARDO, J.-M.; JOFRE, L. Assessment of LTCC-based dielectric flat lens antennas and switched-beam arrays for future 5G millimeter-wave communication systems. **IEEE Transactions on Antennas and Propagation**, v. 65, n. 12, p. 6453–6473, 2017.
- ISLAM, M. R.; ISLAM, M. T.; MONIRUZZAMAN, M.; SAMSUZZAMAN, M.; ARSHAD, H. Penta band single negative meta-atom absorber designed on square enclosed star-shaped modified split ring resonator for S-, C-, X- and Ku-bands microwave applications. **Scientific Reports**, v. 11, n. 1, p. 1–22, 2021.
- JACOBSON, A.; JOHNSON, J. W.; LEWANDOWSKI, J. Interlayer chemistry between thick transition-metal oxide layers: synthesis and intercalation reactions of $\text{K}[\text{Ca}_2\text{Na}_{n-3}\text{Nb}_n\text{O}_{3n+1}]$ ($3 \leq n \leq 7$). **Inorganic chemistry**, v. 24, n. 23, p. 3727–3729, 1985.
- JANGRA, S.; SANGHI, S.; AGARWAL, A.; RANGI, M.; KASWAN, K. Effects of Nd^{3+} and high-valence Nb^{5+} co-doping on the structural, dielectric and magnetic properties of BiFeO_3 multiferroics. **Ceramics International**, v. 44, n. 7, p. 7683–7693, 2018.
- JARTYCH, E.; MAZUREK, M.; LISIŃSKA-CZEKAJ, A.; CZEKAJ, D. Hyperfine interactions in some aurivillius $\text{Bi}_{m+1}\text{Ti}_3\text{Fe}_{m-3}\text{O}_{3m+3}$ compounds. **Journal of Magnetism and Magnetic Materials**, v. 322, n. 1, p. 51–55, 2010.

JARTYCH, E.; PIKULA, T.; MAZUREK, M.; LISINSKA-CZEKAJ, A.; CZEKAJ, D.; GASKA, K.; PRZEWOZNIK, J.; KAPUSTA, C.; SUROWIEC, Z. Antiferromagnetic spin glass-like behavior in sintered multiferroic aurivillius $\text{Bi}_{m+1}\text{Ti}_3\text{Fe}_{m-3}\text{O}_{3m+3}$ compounds. **Journal of magnetism and magnetic materials**, v. 342, p. 27–34, 2013.

JEON, M. K.; KIM, Y.-I.; NAHM, S.-H.; WOO, S. I. Crystal structure of $\text{Bi}_{4-x}\text{Ce}_x\text{Ti}_3\text{O}_{12}$ ($x = 0, 0.25, 0.5$ and 0.75) studied by raman spectroscopy and neutron powder diffraction. **Journal of Physics D: Applied Physics**, v. 39, n. 23, p. 5080—5085, 2006.

JEON, M. K.; KIM, Y.-I.; SOHN, J. M.; WOO, S. I. Cation disorder study of $\text{Bi}_{3.25}\text{La}_{0.75}\text{Ti}_3\text{O}_{12}$ by neutron powder diffraction and raman spectroscopy. **Journal of Physics D: applied physics**, v. 37, n. 18, p. 2588—2592, 2004.

JI, C.; FAN, T.; CHEN, G.; BAI, X.; WANG, J.; HE, J.; CAI, W.; GAO, R.; DENG, X.; WANG, Z. *et al.* Influence of sintering method on microstructure, electrical and magnetic properties of $\text{BiFeO}_3\text{--BaTiO}_3$ solid solution ceramics. **Materials Today Chemistry**, v. 20, p. 1004191–10041910, 2021.

JI, Y.; SONG, K.; ZHANG, S.; LU, Z.; WANG, G.; LI, L.; ZHOU, D.; WANG, D.; REANEY, I. M. Cold sintered, temperature-stable $\text{CaSnSiO}_5\text{--K}_2\text{MoO}_4$ composite microwave ceramics and its prototype microstrip patch antenna. **Journal of the European Ceramic Society**, v. 41, n. 1, p. 424–429, 2021.

JIANG, P.; DUAN, Z.; XU, L.; ZHANG, X.; LI, Y.; HU, Z.; CHU, J. Phase transformation in multiferroic $\text{Bi}_5\text{Ti}_3\text{FeO}_{15}$ ceramics by temperature-dependent ellipsometric and raman spectra: an interband electronic transition evidence. **Journal of Applied Physics**, v. 115, n. 8, p. 0831011–0831017, 2014.

JIANG, P.; ZHANG, X.; CHANG, P.; HU, Z.; BAI, W.; LI, Y.; CHU, J. Spin-phonon interactions of multiferroic $\text{Bi}_4\text{Ti}_3\text{O}_{12}\text{--BiFeO}_3$ ceramics: Low-temperature raman scattering and infrared reflectance spectra investigations. **Journal of Applied Physics**, v. 115, n. 14, p. 1441011–1441016, 2014.

JIANG, Y.; JIANG, X.; CHEN, C.; NIE, X.; HUANG, X.; JIANG, X.; ZHUANG, J.; ZHENG, L.; CHEN, Z. Effect of tantalum substitution on the structural and electrical properties of $\text{BaBi}_8\text{Ti}_7\text{O}_{27}$ intergrowth ceramics. **Ceramics International**, v. 46, n. 6, p. 8122–8129, 2020.

JONSCHER, A. K. The ‘universal’ dielectric response. **Nature**, v. 267, n. 5613, p. 673–679, 1977.

JONSCHER, A. K. Dielectric relaxation in solids. **Journal of Physics D: Applied Physics**, v. 32, n. 14, p. R57–R70, 1999.

JUNIOR, C. R.; FILHO, M. C.; SOUSA, D.; SALES, A.; LEÃO, R.; SOMBRA, A.; BARROSO, G. Structural and electrical properties of the $\text{SrBi}_4\text{Ti}_4\text{O}_{15}:\text{V}_2\text{O}_5$ matrix in the microwave frequency range. **Journal of Electromagnetic Waves and Applications**, v. 32, n. 11, p. 1329–1341, 2018.

KAMUTZKI, F.; SCHNEIDER, S.; BAROWSKI, J.; GURLO, A.; HANAOR, D. A. Silicate dielectric ceramics for millimetre wave applications. **Journal of the European Ceramic Society**, v. 41, n. 7, p. 3879–3894, 2021.

- KATZ, E. A. Perovskite: name puzzle and german-russian odyssey of discovery. **Helvetica Chimica Acta**, v. 103, n. 6, p. e2000061–e20000613, 2020.
- KEYROUZ, S.; CARATELLI, D. Dielectric resonator antennas: basic concepts, design guidelines, and recent developments at millimeter-wave frequencies. **International Journal of Antennas and Propagation**, v. 2016, p. 1–20, 2016.
- KHOMCHENKO, V.; KAKAZEI, G.; POGORELOV, Y.; ARAUJO, J.; BUSHINSKY, M.; KISELEV, D.; KHOLKIN, A.; PAIXÃO, J. Effect of Gd substitution on ferroelectric and magnetic properties of $\text{Bi}_4\text{Ti}_3\text{O}_{12}$. **Materials Letters**, v. 64, n. 9, p. 1066–1068, 2010.
- KHOMCHENKO, V.; SHVARTSMAN, V.; BORISOV, P.; KLEEMANN, W.; KISELEV, D.; BDIKIN, I.; VIEIRA, J.; KHOLKIN, A. Crystal structure and magnetic properties of $\text{Bi}_{0.8}(\text{Gd}_{1-x}\text{Ba}_x)_{0.2}\text{FeO}_3$ ($x=0, 0.5, 1$) multiferroics. **Journal of Physics D: Applied Physics**, v. 42, n. 4, p. 1–6, 2009.
- KISHK, A. A.; AUDA, H. A.; AHN, B. C. Radiation characteristics of cylindrical dielectric resonator antennas with new applications. **IEEE Antennas and Propagation Society Newsletter**, v. 31, n. 1, p. 6–16, 1989.
- KOBAYASHI, Y.; KATOH, M. Microwave measurement of dielectric properties of low-loss materials by the dielectric rod resonator method. **IEEE Transactions on Microwave Theory and Techniques**, v. 33, n. 7, p. 586–592, 1985.
- KOJIMA, A.; TESHIMA, K.; MIYASAKA, T.; SHIRAI, Y. Novel photoelectrochemical cell with mesoscopic electrodes sensitized by lead-halide compounds (2). **ECS Meeting Abstracts**, MA2006-02, n. 7, p. 397, 2006.
- KOVAL, V.; SKORVANEK, I.; VIOLA, G.; ZHANG, M.; JIA, C.; YAN, H. Crystal chemistry and magnetic properties of Gd-substituted aurivillius-type $\text{Bi}_5\text{FeTi}_3\text{O}_{15}$ ceramics. **The Journal of Physical Chemistry C**, v. 122, n. 27, p. 15733–15743, 2018.
- KRZHIZHANOVSKAYA, M.; FILATOV, S.; GUSAROV, V.; PAUFLER, P.; BUBNOVA, R.; MOROZOV, M.; MEYER, D. Aurivillius phases in the $\text{Bi}_4\text{Ti}_3\text{O}_{12}/\text{BiFeO}_3$ system: Thermal behaviour and crystal structure. **Zeitschrift für anorganische und allgemeine Chemie**, v. 631, n. 9, p. 1603–1608, 2005.
- KUBEL, F.; SCHMID, H. X-ray room temperature structure from single crystal data, powder diffraction measurements and optical studies of the aurivillius phase $\text{Bi}_5(\text{Ti}_3\text{Fe})\text{O}_{15}$. **Ferroelectrics**, v. 129, n. 1, p. 101–112, 1992.
- KUI, J. Microwave dielectric ceramic materials and their industry development overview and future prospects. **Journal of Physics: Conference Series**, v. 1885, n. 3, p. 1–7, 2021.
- KUMARI, R.; AHLAWAT, N.; AGARWAL, A.; SANGHI, S.; SINDHU, M.; RANI, S. Effect of doping of alkaline metal ions on structural and electrical properties of $\text{Bi}_{0.8}\text{M}_{0.2}\text{FeO}_3$ -modified $\text{Na}_{0.5}\text{Bi}_{0.5}\text{TiO}_3$ ceramics ($M= \text{Ca}, \text{Sr}, \text{and Ba}$). **Journal of Alloys and Compounds**, v. 747, p. 712–720, 2018.
- KUSHVAHA, D.; TIWARI, B.; ROUT, S. Enhancement of electrical energy storage ability by controlling grain size of polycrystalline BaNb_2O_6 for high density capacitor application. **Journal of Alloys and Compounds**, v. 829, p. 1545731–1545739, 2020.

LAVADO, C.; STACHIOTTI, M. G. $\text{Fe}^{3+}/\text{Nb}^{5+}$ co-doping effects on the properties of aurivillius $\text{Bi}_4\text{Ti}_3\text{O}_{12}$ ceramics. **Journal of Alloys and Compounds**, v. 731, p. 914–919, 2018.

LI, J.; PU, Y.; WANG, X.; SHI, Y.; SHI, R.; YANG, M.; WANG, W.; GUO, X.; PENG, X. Effect of yttrium doping on the structure, dielectric multiferroic and magnetodielectric properties of $\text{Bi}_5(\text{Ti}_3\text{Fe})\text{O}_{15}$ ceramics. **Journal of Materials Science: Materials in Electronics**, v. 31, n. 5, p. 4345–4353, 2020.

LI, J.-B.; HUANG, Y.; RAO, G.; LIU, G.; LUO, J.; CHEN, J.; LIANG, J. Ferroelectric transition of aurivillius compounds $\text{Bi}_5\text{Ti}_3\text{FeO}_{15}$ and $\text{Bi}_6\text{Ti}_3\text{Fe}_2\text{O}_{18}$. **Applied Physics Letters**, v. 96, n. 22, p. 2229031–2229034, 2010.

LIU, G. Z.; WANG, C.; GU, H. S.; LU, H. B. Raman scattering study of La-doped $\text{SrBi}_2\text{Nb}_2\text{O}_9$ ceramics. **Journal of Physics D: Applied Physics**, v. 40, n. 24, p. 7817–7820, 2007.

LIU, J.; BAI, W.; YANG, J.; XU, W.; ZHANG, Y.; LIN, T.; MENG, X.; DUAN, C.-G.; TANG, X.; CHU, J. The Cr-substitution concentration dependence of the structural, electric and magnetic behaviors for aurivillius $\text{Bi}_5\text{FeTi}_3\text{O}_{15}$ multiferroic ceramics. **Journal of Applied Physics**, v. 114, n. 23, p. 234101–2341017, 2013.

LIU, T.; LI, Y.; CHENG, Z.; PENG, Y.; SHEN, M.; YANG, S.; ZHANG, Y. Crystal face-selective $\text{Bi}_4\text{Ti}_3\text{O}_{12}/\text{BiOI}$ heterojunction constructed for enhanced visible light-driven photocatalytic activity. **Applied Surface Science**, v. 552, p. 1495071–1495079, 2021.

LIU, Y.; FAN, L.; YI, W.; YAN, C.; MA, J.; JI, Q.; LIN, Q. Microstructure and ferroelectric properties of bi-excess $\text{Bi}_4\text{Ti}_3\text{O}_{12}$ thin films grown on Si and Pt/Ti/SiO₂/Si substrates. **Ferroelectrics**, v. 554, n. 1, p. 144–149, 2020.

LOMANOVA, N.; MOROZOV, M.; UGOLKOV, V.; GUSAROV, V. Properties of aurivillius phases in the $\text{Bi}_4\text{Ti}_3\text{O}_{12}$ - BiFeO_3 system. **Inorganic Materials**, v. 42, n. 2, p. 189–195, 2006.

LOMANOVA, N.; SEMENOV, V.; PANCHUK, V.; GUSAROV, V. Structural changes in the homologous series of the aurivillius phases $\text{Bi}_{n+1}\text{Fe}_{n-3}\text{Ti}_3\text{O}_{3n+3}$. **Journal of alloys and compounds**, v. 528, p. 103–108, 2012.

LONG, C.; CHANG, Q.; FAN, H. Differences in nature of electrical conduction among $\text{Bi}_4\text{Ti}_3\text{O}_{12}$ -based ferroelectric polycrystalline ceramics. **Scientific reports**, v. 7, n. 1, p. 1–15, 2017.

LONG, C.; DU, T.; REN, W. Significant ion conduction in Cu acceptor-substituted bismuth titanate polycrystalline ceramics. **Journal of Materials Science**, v. 55, n. 14, p. 5715–5729, 2020.

LONG, S.; MCALLISTER, M.; SHEN, L. The resonant cylindrical dielectric cavity antenna. **IEEE Transactions on Antennas and Propagation**, v. 31, n. 3, p. 406–412, 1983.

MAAROUFI, A.; OABI, O.; LUCAS, B. Ac-conductivity and dielectric response of new zinc-phosphate glass/metal composites. **Physica B: Condensed Matter**, v. 492, p. 31–38, 2016.

MACDONALD, J. R.; JOHNSON, W. B. **Impedance Spectroscopy: Theory, Experiment, and Applications**. 2. ed. Hoboken, NJ: John Wiley & Sons, Inc., 2005. ISBN 9780471647492.

- MANOUN, B.; BENMOKHTAR, S.; BIH, L.; AZROUR, M.; EZZAHI, A.; IDER, A.; AZDOUZ, M.; ANNERSTEN, H.; LAZOR, P. Synthesis, structure, and high temperature mössbauer and raman spectroscopy studies of $\text{Ba}_{1.6}\text{Sr}_{1.4}\text{Fe}_2\text{WO}_9$ double perovskite. **Journal of alloys and compounds**, v. 509, n. 1, p. 66–71, 2011.
- MANTRI, S.; DANIELS, J. Domain walls in ferroelectrics. **Journal of the American Ceramic Society**, v. 104, n. 4, p. 1619–1632, 2021.
- MAO, X.; SUN, H.; WANG, W.; LU, Y.; CHEN, X. Effects of Co-substitutes on multiferroic properties of $\text{Bi}_5\text{FeTi}_3\text{O}_{15}$ ceramics. **Solid state communications**, v. 152, n. 6, p. 483–487, 2012.
- MAO, X.; WANG, W.; CHEN, X. Electrical and magnetic properties of $\text{Bi}_5\text{Ti}_3\text{FeO}_{15}$ compound prepared by inserting BiFeO_3 into $\text{Bi}_4\text{Ti}_3\text{O}_{12}$. **Solid state communications**, v. 147, n. 5-6, p. 186–189, 2008.
- MAZUREK, M.; JARTYCH, E.; OLESZAK, D. Mössbauer studies of $\text{Bi}_5\text{Ti}_3\text{FeO}_{15}$ electroceramic prepared by mechanical activation. **Przegląd Elektrotechniczny**, v. 88, n. 9b, p. 256–258, 2012.
- MCALLISTER, M.; LONG, S. A. Resonant hemispherical dielectric antenna. **Electronics Letters**, v. 20, n. 16, p. 657–659, 1984.
- MCALLISTER, M.; LONG, S. A.; CONWAY, G. Rectangular dielectric resonator antenna. **Electronics letters**, v. 19, n. 6, p. 218–219, 1983.
- MCKENZIE, P. Growing demand for electronics... and ceramic components. **American Ceramic Society Bulletin**, v. 100, n. 6, p. 22–23, 2021.
- MIAO, K.; WANG, X.; HU, D.; WANG, Y.; XIAO, J. Fabrication of Y and Fe co-doped $\text{BaZr}_{0.13}\text{Ti}_{1.46}\text{O}_3$ fine-grained ceramics for temperature-stable multilayer ceramic capacitors. **Ceramics International**, v. 43, n. 12, p. 9099–9104, 2017.
- MITZI, D. B.; FEILD, C.; HARRISON, W.; GULOY, A. Conducting tin halides with a layered organic-based perovskite structure. **Nature**, v. 369, n. 6480, p. 467–469, 1994.
- MOHAPATRA, A.; DAS, P. R.; CHOUDHARY, R. Structural and electrical properties of $\text{Bi}_5\text{Ti}_3\text{FeO}_{15}$ ceramics. **Journal of Materials Science: Materials in Electronics**, v. 25, n. 3, p. 1348–1353, 2014.
- MOHAPATRA, S.; SAHU, B.; CHANDRASEKHAR, M.; KUMAR, P.; KAUSHIK, S.; RATH, S.; SINGH, A. Effect of cobalt substitution on structural, impedance, ferroelectric and magnetic properties of multiferroic $\text{Bi}_2\text{Fe}_4\text{O}_9$ ceramics. **Ceramics International**, v. 42, n. 10, p. 12352–12360, 2016.
- MOMMA, K.; IZUMI, F. VESTA: a three-dimensional visualization system for electronic and structural analysis. **Journal of Applied Crystallography**, v. 41, n. 3, p. 653–658, 2008.
- MONEBHURRUN, V. Standard definitions of terms for antennas and radio wave propagation. In: IEEE. **2019 Antenna Measurement Techniques Association Symposium (AMTA)**. [S. l.], 2019. p. 1–2.

- MONGIA, R. K.; BHARTIA, P. Dielectric resonator antennas—a review and general design relations for resonant frequency and bandwidth. **International Journal of Microwave and Millimeter-Wave Computer-Aided Engineering**, v. 4, n. 3, p. 230–247, 1994.
- MOULSON, A. J.; HERBERT, J. M. **Electroceramics: materials, properties, applications**. [S. l.]: John Wiley & Sons, 2003.
- MOZHAROVSKIY, A.; ARTEMENKO, A.; SSORIN, V.; MASLENNIKOV, R.; SEVASTYANOV, A. Wideband tapered antipodal fin-line waveguide-to-microstrip transition for E-band applications. In: IEEE. **2013 European Microwave Conference**. [S. l.], 2013. p. 1187–1190.
- NAN, C.-W.; BICHURIN, M.; DONG, S.; VIEHLAND, D.; SRINIVASAN, G. Multiferroic magnetoelectric composites: Historical perspective, status, and future directions. **Journal of applied physics**, v. 103, n. 3, p. 1–35, 2008.
- OHSATO, H. Microwave dielectrics with perovskite-type structure. In: PAN, L.; ZHU, G. (Ed.). **Perovskite Materials**. Rijeka: IntechOpen, 2016. cap. 9.
- OHSATO, H.; MIZUTA, M.; IKOMA, T.; ONOGI, Y.; NISHIGAKI, S.; OKUDA, T. Microwave dielectric properties of tungsten bronze-type $\text{Ba}_{6-3x}\text{R}_{8+2x}\text{Ti}_{18}\text{O}_{54}$ (R= La, Pr, Nd and Sm) solid solutions. **Journal of the Ceramic Society of Japan**, v. 106, n. 1230, p. 178–182, 1998.
- OKASHA, N.; EL-DEK, S.; AYMAN, M.; ALI, A. I. Comparative study on the influence of rare earth ions doping in $\text{Bi}_{0.6}\text{Sr}_{0.4}\text{FeO}_3$ nanomultiferroics. **Journal of Alloys and Compounds**, v. 689, p. 1051–1058, 2016.
- OLIVEIRA, R.; SILVA, R.; MORAIS, J. D.; BATISTA, G.; SILVA, M.; GOES, J.; ANDRADE, H. de; JÚNIOR, I. Q.; SINGH, C.; SOMBRA, A. Effects of CaTiO_3 addition on the microwave dielectric properties and antenna properties of BiVO_4 ceramics. **Composites Part B: Engineering**, v. 175, p. 1071221–1071226, 2019.
- PAIVA, D.; SILVA, M.; RIBEIRO, T.; VASCONCELOS, I.; SOMBRA, A.; GÓES, J.; FECHINE, P. Novel magnetic–dielectric composite ceramic obtained from $\text{Y}_3\text{Fe}_5\text{O}_{12}$ and CaTiO_3 . **Journal of Alloys and Compounds**, v. 644, p. 763–769, 2015.
- PAN, M.-J.; RANDALL, C. A. A brief introduction to ceramic capacitors. **IEEE electrical insulation magazine**, v. 26, n. 3, p. 44–50, 2010.
- PANDEY, A. K.; PATHAK, S. K. Wideband circularly polarized concentric cylindrical dielectric resonator antenna excited by helix. **International Journal of RF and Microwave Computer-Aided Engineering**, v. 32, n. 1, p. 1–9, 2022.
- PANDEY, S.; KUMAR, D.; PARKASH, O.; PANDEY, L. Design and development of dielectric resonator antenna using ceramic materials: an overview. **Transactions of the Indian Institute of Metals**, v. 72, n. 8, p. 2019–2028, 2019.
- PANDIT, B.; SANKAPAL, B. R.; KOINKAR, P. M. Novel chemical route for $\text{CeO}_2/\text{MWCNTs}$ composite towards highly bendable solid-state supercapacitor device. **Scientific reports**, v. 9, n. 1, p. 1–13, 2019.
- PARIDA, S.; SATAPATHY, A.; SINHA, E.; BISEN, A.; ROUT, S. Effect of neodymium on optical bandgap and microwave dielectric properties of barium zirconate ceramic. **Metallurgical and Materials Transactions A**, v. 46, n. 3, p. 1277–1286, 2015.

- PATRI, T.; PATANGI, R.; KANDULA, K. R.; BANERJEE, K.; ASTHANA, S.; BABU, P. Effect of W/Co co-substitution on structural, microstructural, magnetic and electrical properties of $\text{Bi}_4\text{NdFeTi}_3\text{O}_{15}$ aurivillius compound. **Journal of Materials Science: Materials in Electronics**, v. 31, n. 2, p. 874–884, 2020.
- PAWAR, R.; PATANGE, S. M.; SHITRE, A.; GORE, S.; JADHAV, S.; SHIRSATH, S. E. Crystal chemistry and single-phase synthesis of Gd^{3+} substituted Co-Zn ferrite nanoparticles for enhanced magnetic properties. **RSC advances**, v. 8, n. 44, p. 25258–25267, 2018.
- PENG, Z.; YAN, D.; CHEN, Q.; XIN, D.; LIU, D.; XIAO, D.; ZHU, J. Crystal structure, dielectric and piezoelectric properties of Ta/W codoped $\text{Bi}_3\text{TiNbO}_9$ aurivillius phase ceramics. **Current Applied Physics**, v. 14, n. 12, p. 1861–1866, 2014.
- PETOSA, A.; ITTIPIBOON, A. Dielectric resonator antennas: A historical review and the current state of the art. **IEEE antennas and Propagation Magazine**, v. 52, n. 5, p. 91–116, 2010.
- PIKULA, T.; DZIK, J.; GUZDEK, P.; MITSUOK, V.; SUROWIEC, Z.; PANEK, R.; JARTYCH, E. Magnetic properties and magnetoelectric coupling enhancement in $\text{Bi}_5\text{Ti}_3\text{FeO}_{15}$ ceramics. **Ceramics International**, v. 43, n. 14, p. 11442–11449, 2017.
- PRAJAPAT, D.; SAGDEO, A.; REDDY, V. R. Structural, magnetic and dielectric properties of vanadium substituted four layered aurivillius $\text{Bi}_5\text{FeTi}_3\text{O}_{15}$ ceramics. **Ceramics International**, v. 45, n. 15, p. 19093–19097, 2019.
- PRASATH, S. D. R.; BALAJI, S.; RAJU, S.; ABHAIKUMAR, V. Synthesis and characterization of zinc substituted nickel ferrite materials for L band antenna applications. **Journal of Materials Science: Materials in Electronics**, v. 27, n. 8, p. 8247–8253, 2016.
- PULI, V. S.; ADIREDDY, S.; RAMANA, C. Chemical bonding and magnetic properties of gadolinium (Gd) substituted cobalt ferrite. **journal of alloys and compounds**, v. 644, p. 470–475, 2015.
- QIU, Y.; ZHAO, S.; WANG, Z. Magnetoelectric effect of Dy doped $\text{Bi}_5\text{FeTi}_3\text{O}_{15}$ films prepared by sol-gel method. **Materials Letters**, v. 170, p. 89–92, 2016.
- RAGHAVAN, C. M.; KIM, J. W.; CHOI, J. Y.; KIM, J.-W.; KIM, S. S. Effects of donor W^{6+} -ion doping on the microstructural and multiferroic properties of aurivillius $\text{Bi}_7\text{Fe}_3\text{Ti}_3\text{O}_{21}$ thin film. **Applied Surface Science**, v. 346, p. 201–206, 2015.
- RAI, C.; SINGH, S.; SINGH, A. K.; VERMA, R. K. Design and analysis of dual-band circularly polarized hybrid ring cylindrical dielectric resonator antenna for wireless applications in c and x-band. **Wireless Personal Communications**, p. 1–19, 2022.
- RAVANAMMA, R.; REDDY, K. M.; KRISHNAIAH, K. V.; RAVI, N. Structure and morphology of yttrium doped barium titanate ceramics for multi-layer capacitor applications. **Materials Today: Proceedings**, v. 46, p. 259–262, 2021.
- RAVEENDRAN, A.; SEBASTIAN, M. T.; RAMAN, S. Applications of microwave materials: a review. **Journal of Electronic Materials**, v. 48, n. 5, p. 2601–2634, 2019.

- RAYMOND, O.; FONT, R.; SUÁREZ-ALMODOVAR, N.; PORTELLES, J.; SIQUEIROS, J. Frequency-temperature response of ferroelectromagnetic $\text{Pb}(\text{Fe}_{1/2}\text{Nb}_{1/2})\text{O}_3$ ceramics obtained by different precursors. part I. structural and thermo-electrical characterization. **Journal of Applied Physics**, v. 97, n. 8, p. 0841071–0841078, 2005.
- REHMAN, F.; JIN, H.-B.; WANG, L.; TANVER, A.; SU, D.-Z.; LI, J.-B. Effect of Nd^{3+} substitution for Bi^{3+} on the dielectric properties and conduction behavior of aurivillius $\text{NdBi}_4\text{Ti}_3\text{FeO}_{15}$ ceramics. **RSC Advances**, v. 6, n. 25, p. 21254–21260, 2016.
- RICHTMYER, R. Dielectric resonators. **Journal of applied physics**, v. 10, n. 6, p. 391–398, 1939.
- ROUSSEAU, D. L.; BAUMAN, R. P.; PORTO, S. Normal mode determination in crystals. **Journal of Raman Spectroscopy**, v. 10, n. 1, p. 253–290, 1981.
- RUDDLESDEN, S.; POPPER, P. New compounds of the K_2NiF_4 type. **Acta Crystallographica**, v. 10, n. 8, p. 538–539, 1957.
- RUDDLESDEN, S.; POPPER, P. The compound $\text{Sr}_3\text{Ti}_2\text{O}_7$ and its structure. **Acta Crystallographica**, v. 11, n. 1, p. 54–55, 1958.
- SABBAN, A. **Wideband RF Technologies and Antennas in microwave frequencies**. [S. l.]: John Wiley & Sons, 2016.
- SABBAN, A. Microwave technologies for wearable communication systems. In: **Novel Wearable Antennas for Communication and Medical Systems**. [S. l.]: CRC Press, 2017. p. 329–372.
- SAGER, O.; TISI, F. On eigenmodes and forced resonance-modes of dielectric spheres. **Proceedings of the IEEE**, v. 56, n. 9, p. 1593–1594, 1968.
- SCHNEIDER, C. A.; RASBAND, W. S.; ELICEIRI, K. W. NIH Image to ImageJ: 25 years of image analysis. **Nature methods**, v. 9, n. 7, p. 671–675, 2012.
- SCOTT, J.; ORLANDO, A.; RAMESH, R. Device physics of ferroelectric memories. **Ferroelectrics**, v. 183, n. 1, p. 51–63, 1996.
- SHAHJEHAN, W.; HUSSAIN, I.; AMIN, K.; ALI, I.; RIAZ, A.; UTHANSAKUL, P. Hepta-band antenna for 5G applications. **Wireless Personal Communications**, p. 1–24, 2022.
- SHANNON, R. D. Revised effective ionic radii and systematic studies of interatomic distances in halides and chalcogenides. **Acta crystallographica section A: crystal physics, diffraction, theoretical and general crystallography**, v. 32, n. 5, p. 751–767, 1976.
- SHARMA, S.; SHAMIM, K.; RANJAN, A.; RAI, R.; KUMARI, P.; SINHA, S. Impedance and modulus spectroscopy characterization of lead free barium titanate ferroelectric ceramics. **Ceramics International**, v. 41, n. 6, p. 7713–7722, 2015.
- SHIMAKAWA, Y.; KUBO, Y.; TAUCHI, Y.; KAMIYAMA, T.; ASANO, H.; IZUMI, F. Structural distortion and ferroelectric properties of $\text{SrBi}_2(\text{Ta}_{1-x}\text{Nb}_x)_2\text{O}_9$. **Applied Physics Letters**, v. 77, n. 17, p. 2749–2751, 2000.
- SIDDIQUE, M.; AHMED, E.; BUTT, N. Particle size effect on Mössbauer parameters in $\gamma\text{-Fe}_2\text{O}_3$ nanoparticles. **Physica B: Condensed Matter**, v. 405, n. 18, p. 3964–3967, 2010.

SILVA, M.; FERNANDES, T.; SOMBRA, A. An alternative method for the measurement of the microwave temperature coefficient of resonant frequency (τf). **Journal of Applied Physics**, v. 112, n. 7, p. 0741061–0741066, 2012.

SILVA, P.; FERNANDES, T.; OLIVEIRA, R.; SILVA, M.; SOMBRA, A. Radiofrequency and microwave properties study of the electroceramic $\text{BaBi}_4\text{Ti}_4\text{O}_{15}$. **Materials Science and Engineering: B**, v. 182, p. 37–44, 2014.

SILVA, P.; SILVA, M.; SILVA, R. da; CORREA, M.; BOHN, F.; MENEZES, A. de; FERREIRA, W.; AYALA, A.; SOMBRA, A.; FECHINE, P. Effects of the Bi^{3+} substitution on the structural, vibrational, and magnetic properties of bismuth layer-structured ferroelectrics. **Applied Physics A**, v. 126, n. 8, p. 1–12, 2020.

SILVA, P.; SILVA, M.; SOMBRA, A.; FECHINE, P. Dielectric properties of bismuth layer structured ferroelectric $\text{Bi}_3\text{R}_2\text{Ti}_3\text{FeO}_{15}$ (R= Bi, Gd, and Nd) at microwave and radiofrequency. **Journal of Materials Science: Materials in Electronics**, p. 1–16, 2021.

SIMONE, M.; LODI, M. B.; MUNTONI, G.; CURRELI, N.; FANTI, A.; PISANU, T.; VALENTE, G.; MONTISCI, G.; MAZZARELLA, G. Two co-linear transitions for Q-band horn waveguide dense cluster. In: IEEE. **2022 16th European Conference on Antennas and Propagation (EuCAP)**. [S. l.], 2022. p. 1–4.

SOREN, D.; TAMBOLI, N. Revisited the design technique of hybrid dielectric resonator antenna. In: **Smart Technologies for Energy, Environment and Sustainable Development, Vol 1**. [S. l.: s. n.], 2022. p. 609–620.

SUBBARAO, E. A family of ferroelectric bismuth compounds. **Journal of Physics and Chemistry of Solids**, v. 23, n. 6, p. 665–676, 1962.

SUN, S.; LIU, C.; WANG, G.; CHEN, Z.; CHEN, T.; PENG, R.; LU, Y. Structural and physical properties of mixed-layer aurivillius-type multiferroics. **Journal of the American Ceramic Society**, v. 99, n. 9, p. 3033–3038, 2016.

SUTAR, B.; CHOUDHARY, R.; DAS, P. R. Dielectric and impedance spectroscopy of $\text{Sr}(\text{Bi}_{0.5}\text{Nb}_{0.5})\text{O}_3$ ceramics. **Ceramics International**, v. 40, n. 6, p. 7791–7798, 2014.

SUZUKI, S.; YAMAGUCHI, S.; DOI, A.; SHIOTA, A.; IWAJI, N.; ABE, S.; MATSUDA, M.; NAKAMURA, T.; SANO, H. Suppressive effect of Ni–Sn internal electrode at the anode on the leakage current degradation of BaTiO_3 -based multilayer ceramic capacitors. **Applied Physics Letters**, v. 118, n. 11, p. 1129041–1129044, 2021.

SWAIN, S.; KUMAR, P.; CHOUDHARY, R. B. Electrical and ferroelectric studies of the 2-layered $\text{SrBi}_2\text{Ta}_2\text{O}_9$ based ceramics. **Physica B: Condensed Matter**, v. 477, p. 56–63, 2015.

TANG, K.; BAI, W.; LIU, J.; YANG, J.; ZHANG, Y.; DUAN, C.-g.; TANG, X.; CHU, J. The effect of mn doping contents on the structural, dielectric and magnetic properties of multiferroic $\text{Bi}_5\text{FeTi}_3\text{O}_{15}$ aurivillius ceramics. **Ceramics International**, v. 41, p. S185–S190, 2015.

THAKUR, S.; RAI, R.; BDIKIN, I.; RAI, S. P. Dielectric relaxation and ac conduction in multiferroic $\text{Bi}_{0.8}\text{Gd}_{0.1}\text{Pb}_{0.1}\text{Fe}_{0.9}\text{Ti}_{0.1}\text{O}_3$ ceramics: impedance spectroscopy analysis. **Phase Transitions**, v. 89, n. 12, p. 1213–1224, 2016.

TI, R.; HUANG, F.; ZHU, W.; HE, J.; XU, T.; YUE, C.; ZHAO, J.; LU, X.; ZHU, J. Multiferroic and dielectric properties of $\text{Bi}_4\text{LaTi}_3\text{FeO}_{15}$ ceramics. **Ceramics International**, v. 41, p. S453–S457, 2015.

TILLEY, R. J. **Perovskites: structure-property relationships**. [S. l.]: John Wiley & Sons, 2016.

TSENG, C.-F.; HUANG, C.-L.; YANG, W.-R.; HSU, C.-H. Dielectric characteristics of $\text{Nd}(\text{Zn}_{1/2}\text{Ti}_{1/2})\text{O}_3$ ceramics at microwave frequencies. **Journal of the American Ceramic Society**, v. 89, n. 4, p. 1465–1470, 2006.

ULLAH, A.; LIU, H.; MANAN, A.; AHMAD, A. S.; PENGCHENG, Z.; HAO, H.; CAO, M.; YAO, Z.; ULLAH, A.; JAN, A. *et al.* Microwave dielectric properties of $\text{Bi}_2(\text{Li}_{0.5}\text{Ta}_{1.5})\text{O}_7\text{-TiO}_2$ -based ceramics for 5G cellular base station resonator application. **Ceramics International**, v. 47, n. 6, p. 8416–8423, 2021.

UNIYAL, P.; YADAV, K. Pr doped bismuth ferrite ceramics with enhanced multiferroic properties. **Journal of Physics: Condensed Matter**, v. 21, n. 40, p. 4059011–4059019, 2009.

WANG, J.; LU, X.; LI, Y.; WANG, L.; ZHU, H.; FU, Z.; YAN, F.; WANG, X.; ZHANG, Q. Correlations between microwave dielectric properties and crystal structures of Sb-doped $\text{Co}_{0.5}\text{Ti}_{0.5}\text{NbO}_4$ ceramics. **Ceramics International**, v. 46, n. 3, p. 3464–3470, 2020.

WANG, Y.; ZHANG, M.; WU, J.; HU, Z.; ZHANG, H.; YAN, H. Ferroelectric and photocatalytic properties of aurivillius phase $\text{Ca}_2\text{Bi}_4\text{Ti}_5\text{O}_{18}$. **Journal of the American Ceramic Society**, v. 104, n. 1, p. 322–328, 2021.

WANG, Z.; CHEN, Y. Structures and microwave dielectric properties of Ti-doped CeO_2 ceramics with a near-zero temperature coefficient of resonant frequency. **Journal of Alloys and Compounds**, v. 854, p. 1572701–1572708, 2021.

WENDARI, T. P.; ARIEF, S.; MUFTI, N.; INSANI, A.; BAAS, J.; BLAKE, G. R. *et al.* Structural and multiferroic properties in double-layer aurivillius phase $\text{Pb}_{0.4}\text{Bi}_{2.1}\text{La}_{0.5}\text{Nb}_{1.7}\text{Mn}_{0.3}\text{O}_9$ prepared by molten salt method. **Journal of Alloys and Compounds**, v. 820, p. 1531451–1531456, 2020.

WU, F.-F.; ZHOU, D.; DU, C.; JIN, B.-B.; LI, C.; QI, Z.-M.; SUN, S.; ZHOU, T.; LI, Q.; ZHANG, X.-Q. Design of a sub-6 GHz dielectric resonator antenna with novel temperature-stabilized $(\text{Sm}_{1-x}\text{Bi}_x)\text{NbO}_4$ ($x=0\text{--}0.15$) microwave dielectric ceramics. **ACS Applied Materials & Interfaces**, v. 14, n. 5, p. 7030–7038, 2022.

WU, J.; ZHANG, H.; MENG, N.; KOVAL, V.; MAHAJAN, A.; GAO, Z.; ZHANG, D.; YAN, H. Perovskite $\text{Bi}_{0.5}\text{Na}_{0.5}\text{TiO}_3$ -based materials for dielectric capacitors with ultrahigh thermal stability. **Materials & Design**, v. 198, p. 1093441–1093449, 2021.

WU, M.; TIAN, Z.; YUAN, S.; HUANG, Z. Magnetic and optical properties of the aurivillius phase $\text{Bi}_5\text{Ti}_3\text{FeO}_{15}$. **Materials Letters**, v. 68, p. 190–192, 2012.

XIAO, J.; ZHANG, H.; XUE, Y.; LU, Z.; CHEN, X.; SU, P.; YANG, F.; ZENG, X. The influence of Ni-doping concentration on multiferroic behaviors in $\text{Bi}_4\text{NdTi}_3\text{FeO}_{15}$ ceramics. **Ceramics International**, v. 41, n. 1, p. 1087–1092, 2015.

- YAFENG, Q.; XIAOJUAN, W.; JUN, Z.; XIANGY, M.; XIAOBING, C. Microstructure of $\text{Bi}_{3-x}\text{Nd}_x\text{TiNbO}_9$ bismuth layer-structured ceramics. **Journal of Rare Earths**, v. 25, p. 240–243, 2007.
- YIN, W.; CHEN, C.; BAI, W.; YANG, J.; ZHANG, Y.; TANG, X.; DUAN, C.-G.; CHU, J. Dielectric behavior dependence on temperature and Cr-doping contents of aurivillius $\text{Bi}_5\text{Ti}_3\text{FeO}_{15}$ ceramics. **Ceramics International**, v. 42, n. 3, p. 4298–4305, 2016.
- YU, G.; WANG, L.; ZHU, C.; LV, F.; LIU, F.; KONG, W.; ZHAO, Y.; ZENG, P.; HUANG, Z. Relaxor dielectric properties of lead-free $\text{Bi}_4\text{Ti}_3\text{O}_{12}/\text{Bi}_{4.5}\text{Na}_{0.5}\text{Ti}_4\text{O}_{15}$ intergrowth ceramics. **Ceramics International**, v. 46, n. 7, p. 9474–9484, 2020.
- YU, Z.; YU, B.; LIU, Y.; ZHOU, P.; JIANG, J.; LIANG, K.; LU, Y.; SUN, H.; CHEN, X.; MA, Z. *et al.* Enhancement of multiferroic properties of aurivillius $\text{Bi}_5\text{FeTi}_3\text{O}_{15}$ ceramics by Co doping. **Ceramics International**, v. 43, n. 17, p. 14996–15001, 2017.
- ZHANG, D.; FENG, L.; HUANG, W.; ZHAO, W.; CHEN, Z.; LI, X. Oxygen vacancy-induced ferromagnetism in $\text{Bi}_4\text{NdTi}_3\text{FeO}_{15}$ multiferroic ceramics. **Journal of Applied Physics**, v. 120, n. 15, p. 1541051–1541057, 2016.
- ZHANG, M.; CHEN, Z.; YUE, Y.; CHEN, T.; YAN, Z.; JIANG, Q.; YANG, B.; ERIKSSON, M.; TANG, J.; ZHANG, D. *et al.* Terahertz reading of ferroelectric domain wall dielectric switching. **ACS Applied Materials & Interfaces**, v. 13, n. 10, p. 12622–12628, 2021.
- ZHAO, H.; KIMURA, H.; CHENG, Z.; OSADA, M.; WANG, J.; WANG, X.; DOU, S.; LIU, Y.; YU, J.; MATSUMOTO, T. *et al.* Large magnetoelectric coupling in magnetically short-range ordered $\text{Bi}_5\text{Ti}_3\text{FeO}_{15}$ film. **Scientific reports**, v. 4, n. 1, p. 1–8, 2014.
- ZUO, X.; HE, E.; QIN, Y.; GUAN, B.; ZHAO, G.; WU, J.; HUI, Z.; YANG, J.; ZHU, X.; DAI, J. Structural, magnetic, electrical and optical properties of aurivillius phase $\text{Bi}_6\text{Fe}_{1.5}\text{Co}_{0.5}\text{Ti}_{3-x}\text{W}_x\text{O}_{18}$ ($0 \leq x \leq 0.07$) ceramics. **Journal of Alloys and Compounds**, v. 906, n. 164393, p. 1–10, 2022.
- ZUO, X.; YANG, J.; YUAN, B.; SONG, D.; TANG, X.; ZHANG, K.; ZHU, X.; SONG, W.; DAI, J.; SUN, Y. Enhanced multiferroic properties of aurivillius $\text{Bi}_6\text{Fe}_{1.4}\text{Co}_{0.6}\text{Ti}_3\text{O}_{18}$ thin films by magnetic field annealing. **Applied Physics Letters**, v. 107, n. 22, p. 222901–2229014, 2015.
- ZUO, X.; ZHANG, M.; HE, E.; GUAN, B.; QIN, Y.; YANG, J.; ZHU, X.; DAI, J. Structural, magnetic, and dielectric properties of W/Cr co-substituted aurivillius $\text{Bi}_5\text{Ti}_3\text{FeO}_{15}$. **Journal of Alloys and Compounds**, v. 726, p. 1040–1046, 2017.

APPENDIX A – ATOMIC POSITIONS AND FACTORS OCCUPATION THE SAMPLES BFTO, BGFTO AND BNFTO

Table 10 – Atomic positions and factors occupation the samples BFTO, BGFTO and BNFTO.

Atom	x	y	z	occ	x	y	z	occ	x	y	z	occ
O1	0.3310	0.3252	0.0000	1.00	0.3310	0.3252	0.0000	1.00	0.3310	0.3252	0.0000	1.00
O2	0.0082	-0.0075	0.25050	1.00	0.0082	-0.0075	0.25050	1.00	0.0082	-0.0075	0.25050	1.00
O3	0.3271	0.1882	0.09477	1.00	0.3271	0.1882	0.09477	1.00	0.3271	0.1882	0.09477	1.00
O4	0.2918	0.3026	0.19455	1.00	0.2918	0.3026	0.19455	1.00	0.2918	0.3026	0.19455	1.00
O5	0.0419	0.0310	0.03988	1.00	0.0419	0.0310	0.03988	1.00	0.0419	0.0310	0.03988	1.00
O6	0.6088	0.4554	0.0511	1.00	0.6088	0.4554	0.0511	1.00	0.6088	0.4554	0.0511	1.00
O7	0.0843	-0.0311	0.14698	1.00	0.0843	-0.0311	0.14698	1.00	0.0843	-0.0311	0.14698	1.00
O8	0.5346	0.5144	0.13864	1.00	0.5346	0.5144	0.13864	1.00	0.5346	0.5144	0.13864	1.00
Ti1	0.2951	0.2514	0.04871	0.75	0.2951	0.2514	0.04871	0.75	0.2951	0.2514	0.04871	0.75
Ti2	0.2916	0.2582	0.15292	0.75	0.2916	0.2582	0.15292	0.75	0.2916	0.2582	0.15292	0.75
Fe1	0.2951	0.2514	0.04871	0.25	0.2951	0.2514	0.04871	0.25	0.2951	0.2514	0.04871	0.25
Fe2	0.2916	0.2582	0.15292	0.25	0.2916	0.2582	0.15292	0.25	0.2916	0.2582	0.15292	0.25
Bi1	0.2500	0.7559	0.0000	1.00	0.2500	0.7559	0.0000	0.50	0.2500	0.7559	0.0000	0.50
Bi2	0.2322	0.7304	0.21925	1.00	0.2322	0.7304	0.21925	0.625	0.2322	0.7304	0.21925	0.625
Bi3	0.2470	0.7548	0.104680	1.00	0.2470	0.7548	0.104680	0.625	0.2470	0.7548	0.104680	0.625
Gd1					0.2500	0.7559	0.0000	0.50				
Gd2					0.2322	0.7304	0.21925	0.375				
Gd3					0.2470	0.7548	0.104680	0.375				
Nd1					0.25	0.7559	0.0000	0.500				
Nd2					0.2322	0.7304	0.21925	0.375				
Nd3					0.2470	0.7548	0.104680	0.375				

Source: (SILVA *et al.*, 2020), Copyright ©2020, Springer Nature.

APPENDIX B – DISTRIBUTION OF THE NORMAL MODES TO BFTO PHASE

Table 11 – Distribution of the normal modes of vibration of the BFTO

Atom	Wyckoff Site	Symmetry	Irreducible Representations
Bi1	4a	C_s^{yz}	$2A_1 \oplus A_2 \oplus B_1 \oplus 2B_2$
Bi2	8b	C_1	$3A_1 \oplus 3A_2 \oplus 3B_1 \oplus 3B_2$
Bi3	8b	C_1	$3A_1 \oplus 3A_2 \oplus 3B_1 \oplus 3B_2$
(Ti/Fe)1	8b	C_1	$3A_1 \oplus 3A_2 \oplus 3B_1 \oplus 3B_2$
(Ti/Fe)2	8b	C_1	$3A_1 \oplus 3A_2 \oplus 3B_1 \oplus 3B_2$
O1	4a	C_s^{yz}	$2A_1 \oplus A_2 \oplus B_1 \oplus 2B_2$
O2	8b	C_1	$3A_1 \oplus 3A_2 \oplus 3B_1 \oplus 3B_2$
O3	8b	C_1	$3A_1 \oplus 3A_2 \oplus 3B_1 \oplus 3B_2$
O4	8b	C_1	$3A_1 \oplus 3A_2 \oplus 3B_1 \oplus 3B_2$
O5	8b	C_1	$3A_1 \oplus 3A_2 \oplus 3B_1 \oplus 3B_2$
O6	8b	C_1	$3A_1 \oplus 3A_2 \oplus 3B_1 \oplus 3B_2$
O7	8b	C_1	$3A_1 \oplus 3A_2 \oplus 3B_1 \oplus 3B_2$
O8	8b	C_1	$3A_1 \oplus 3A_2 \oplus 3B_1 \oplus 3B_2$
Total			$37A_1 \oplus 35A_2 \oplus 35B_1 \oplus 37B_2$
Acoustic modes			$A_1 \oplus B_1 \oplus B_2$
Raman active modes			$36A_1 \oplus 35A_2 \oplus 34B_1 \oplus 36B_2$
Infrared active modes			$36A_1 \oplus 34B_1 \oplus 36B_2$

Source: (SILVA *et al.*, 2020), Copyright ©2020, Springer Nature.

APPENDIX C – LIST OF PAPERS AND ABSTRACTS RELATED TO THIS THESIS

In the following pages, the main academic productions throughout this work are presented. The first page of published articles, certificates from participation in symposiums and conferences in the form of posters or oral presentations. In addition to the book chapter produced in collaboration with my research group.



Effects of the Bi³⁺ substitution on the structural, vibrational, and magnetic properties of bismuth layer-structured ferroelectrics

P. H. T. Silva¹ · M. A. S. Silva² · R. B. da Silva³ · M. A. Correa³ · F. Bohn³ · A. S. de Menezes⁴ · W. C. Ferreira⁵ · A. P. Ayala⁵ · A. S. B. Sombra² · P. B. A. Fechine¹

Received: 14 June 2020 / Accepted: 26 July 2020 / Published online: 31 July 2020
© Springer-Verlag GmbH Germany, part of Springer Nature 2020

Abstract

Bismuth layer-structured ferroelectric Bi₃R₂Ti₃FeO₁₅ (R = Bi, Nd, and Gd) ceramics were synthesized by conventional solid-state reaction. All the samples showed an orthorhombic structure with A2₁am space group. Bi₃Nd₂Ti₃FeO₁₅ and Bi₃Gd₂Ti₃FeO₁₅ presented a reduction in the orthorhombicity when compared to Bi₅Ti₃FeO₁₅. The magnetic susceptibility of all samples followed the Curie–Weiss law, with negative values of the Curie–Weiss temperature, demonstrating that the magnetic interactions are antiferromagnetic in nature. The magnetization curves suggested a weak canted antiferromagnetic behavior for temperatures below 25 K, followed by a linear behavior in the curves at high temperatures. Mössbauer spectroscopy measurements revealed an increase of the quadrupole splitting values as the temperature decreases, indicating that the samples present local distortions, favoring the existence of weak ferromagnetic phase via the antisymmetric Dzyaloshinskii–Moriya interaction.

Keywords Bi₅ti₃FeO₁₅ · Rare earth · Raman spectroscopy · Bismuth-layer-structured-ferroelectric

Electronic supplementary material The online version of this article (<https://doi.org/10.1007/s00339-020-03858-y>) contains supplementary material, which is available to authorized users.

✉ P. B. A. Fechine
fechine@ufc.br

- ¹ Grupo de Química de Materiais Avançados (GQMat), Departamento de Química Analítica e Físico-Química, Universidade Federal do Ceará-UFC, Campus do Pici, CP 12100, Fortaleza, CE CEP 60451-970, Brazil
- ² Laboratório de Telecomunicações e Ciência e Engenharia de Materiais (LOCEM), Departamento de Física, Universidade Federal do Ceará, Fortaleza, CE 60451-970, Brazil
- ³ Departamento de Física, Universidade Federal do Rio Grande do Norte, Natal, RN CEP 59078-900, Brazil
- ⁴ Departamento de Física, Centro de Ciências Exatas e Tecnologia, Universidade Federal do Maranhão, Bacanga, São Luís, MA CEP 65080-805, Brazil
- ⁵ Departamento de Física, Universidade Federal do Ceará, Campus do Pici, CP 6030, Fortaleza, CE CEP 65455-900, Brazil

1 Introduction

Over the 50 years, bismuth layer-structured ferroelectrics (BLSF) have attracted great attention due to their interesting physical properties and broad potential of applications, such as in sensors, electronic devices, memory storage, antennas, and solar cells [1–10]. Generally, BLSF are presented in the form (Bi₂O₂)²⁺[A_{m-1}B_mO_{3m+1}]²⁻, in which site A can be mono, di or trivalent cations (or a combination of these). Site B generally holds tetravalent, pentavalent, and hexavalent cations, similar ions or combinations [11–13]. The subscript *m* informs the number of perovskite layers [A_{m-1}B_mO_{3m+1}] intercalated by (Bi₂O₂)²⁺ layers [14, 15]. Bi₅Ti₃FeO₁₅ (BFTO) is a typical member of the Aurivillius family with *m* = 4 (four perovskite-like layers per unit cell), where the cube-octahedral site A is occupied by 12 coordinated Bi³⁺ and site B is occupied by Ti/Fe octahedrally coordinated [16]. For BFTO with *m* = 4, there are two orthorhombic phases with *Fmm*2 [17, 18] and A2₁am [19] space groups.

The structural, electrical, magnetic, and optical properties of BFTO have been investigated by numerous techniques, focusing on different aspects [20–24]. These works show that the crystalline structure belongs to the A2₁am



Dielectric properties of bismuth layer structured ferroelectric $\text{Bi}_3\text{R}_2\text{Ti}_3\text{FeO}_{15}$ (R = Bi, Gd, and Nd) at microwave and radiofrequency

P. H. T. Silva¹, M. A. S. Silva², A. S. B. Sombra², and P. B. A. Fechine^{1,*}

¹Grupo de Química de Materiais Avançados (GQMat)- Departamento de Química Analítica e Físico-Química, Universidade Federal do Ceará – UFC, Campus do Pici, CP 12100, Fortaleza, CE CEP 60451-970, Brazil

²Laboratório de Telecomunicações e Ciência e Engenharia de Materiais (LOCEM), Departamento de Física, Universidade Federal do Ceará, Fortaleza, Brazil

Received: 29 March 2021

Accepted: 3 June 2021

© The Author(s), under exclusive licence to Springer Science+Business Media, LLC, part of Springer Nature 2021

ABSTRACT

Bismuth layer structured ferroelectric $\text{Bi}_3\text{R}_2\text{Ti}_3\text{FeO}_{15}$ with R = Bi (BFTO), Gd (BGFTO), and Nd (BNFTO) composition were synthesized by solid-state route, and their morphology and dielectric properties were investigated. The BGFTO and BNFTO samples, show a decrease in dielectric characteristics compared to BFTO. This can be explained by structural distortion resulting from the replacement of lanthanides in the cations of A-site in the perovskite layer. Impedance spectroscopy was performed to establish a correlation between the electrical properties and the microstructure of the ceramics. A non-Debye relaxation induced by a thermally activated mechanism can be observed in all samples. The activation energy of the materials found in the range of 0.6–0.9 eV and indicates the association of doubly ionized oxygen vacancy. The three phases proved to be news candidates for X4D capacitors, with excellent temperature stability (29–150 °C, $TCC \leq \pm 3.3\%$). In addition, the electroceramics were used to design a cylindrical dielectric resonator antenna (CDRA) for microwave applications. The $\text{Bi}_3\text{R}_2\text{Ti}_3\text{FeO}_{15}$ -based CDRA showed great potential for microwave antenna application operating in the S-band. A change is observed to τ_f of BFTO phase ($-428.48 \text{ ppm } ^\circ\text{C}^{-1}$) to BGFTO ($+59.17 \text{ ppm } ^\circ\text{C}^{-1}$) and BNFTO ($+57.69 \text{ ppm } ^\circ\text{C}^{-1}$). This result opens up a great opportunity for future work in CDRA with near-zero temperature coefficients ($\tau_f \sim 0$).

Address correspondence to E-mail: fechine@ufc.br

<https://doi.org/10.1007/s10854-021-06332-4>


Published online: 08 June 2021

**Universidade Federal do Ceará
Pró-Reitoria de Pesquisa e Pós-Graduação
Encontros Universitários 2018**

CERTIFICADO

Certificamos que o trabalho 'ESTUDO DAS PROPRIEDADES ELÉTRICAS DA FASE BI3R2TI3FEO15 (R=BI, ND E GD) POR ESPECTROSCOPIA DE IMPEDÂNCIA' do(s) autor(es) PAULO HENRIQUE TEIXEIRA DA SILVA, ANTONIO SERGIO BEZERRA SOMBRA, ALAN SILVA DE MENEZES, MARCELO ANTONIO SANTOS DA SILVA e PIERRE BASÍLIO ALMEIDA FECHINE foi apresentado no XI Encontro de Pesquisa e Pós-Graduação realizado no período de 24 a 26 de Outubro de 2018.

Fortaleza, 28 de Maio de 2019


Antonio Gomes de Souza Filho
Pró-Reitor de Pesquisa e Pós-Graduação


Geanne Matos de Andrade
Coordenadora de Pesquisa



Brazilian Materials
Research Society

Excellence in the union of science and research
in materials technology in Brazil

Certificate

(P6.D.16)

Hereby we certify that the work
Structural and dielectric behaviour of the four-layer Aurivillius-phase $\text{Bi}_3\text{R}_2\text{FeTi}_3\text{O}_{15}$ (R= Bi, Gd and Nd),

submitted by

Paulo Henrique Teixeira da Silva, Marcelo Antonio Santos da Silva, Alan Silva de Menezes, Wellington Castro Ferreira, Alejandro Pedro Ayala, Antonio Sérgio Bezerra Sombra and Pierre Basílio Almeida Fachine

was presented in **Poster** form by **Paulo Henrique Teixeira da Silva** at
the XVII Brazilian MRS Meeting, in Natal-RN, from 16th to 20th of September 2018.

Antonio Eduardo Martinelli
Conference Chair

Osvaldo Novais de Oliveira Júnior
Brazil MRS President

CERTIFICADO



18ª SEMANA
NACIONAL DE
**CIÊNCIA E
TECNOLOGIA**

A TRANSVERSALIDADE DA
CIÊNCIA, TECNOLOGIA E INOVAÇÕES PARA O PLANETA

semanact.mcti.gov.br

01 A 03 DE DEZEMBRO DE 2021



INSTITUTO FEDERAL
Piauí
Campus Corrente

Certificamos que **Paulo Henrique Teixeira da Silva**, participou, na qualidade de **Palestrante**, do evento Semana Nacional de Ciências e Tecnologia - SNCT CACOR, ministrando a atividade **Palestra - Cerâmicas ferroelétricas estruturadas em camadas de bismuto: versatilidade estrutural e aplicações em dispositivos eletrônicos**, contabilizando carga horária total de 1 hora(s).

Corrente-PI, 03 de dezembro de 2021

Laécio Barros Dias

Diretor geral do IFPI Campus Corrente

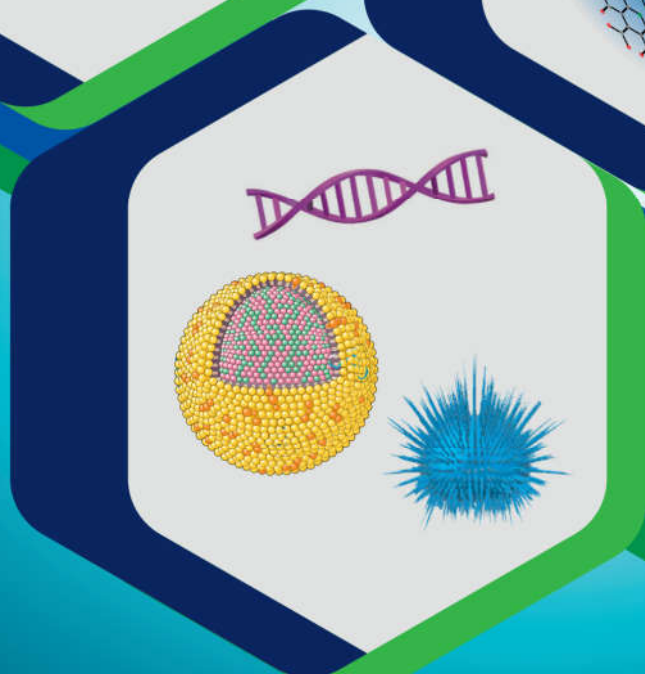
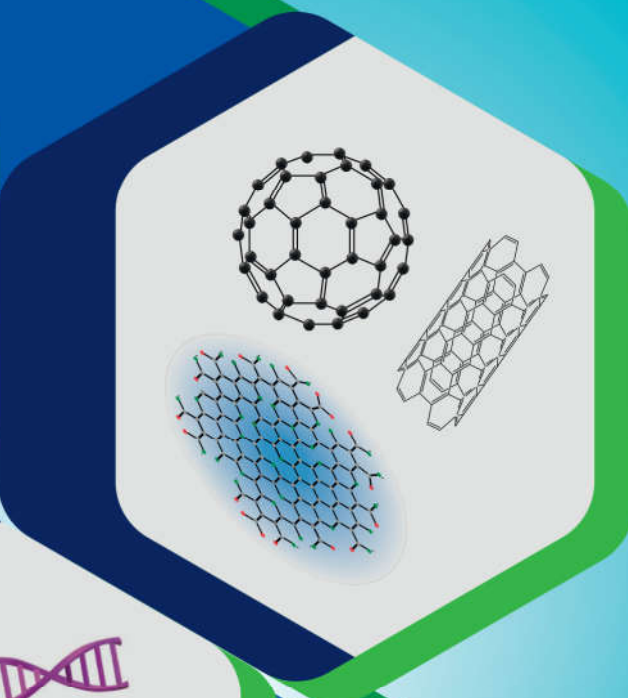
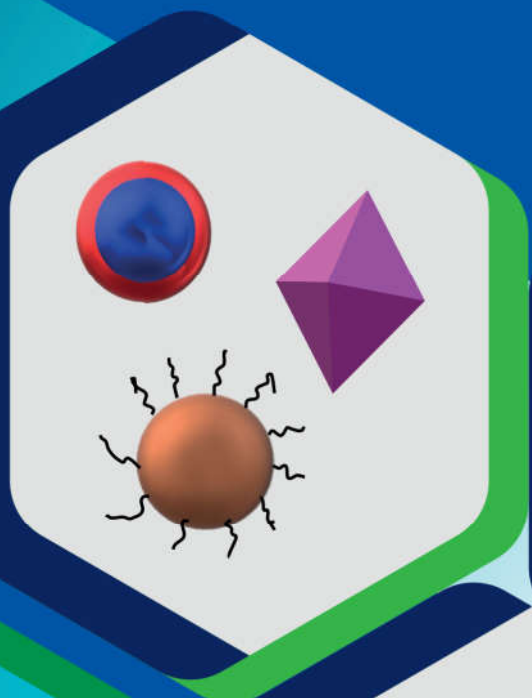
Josélia Paes Ribeiro de Souza

Coordenadora de Pesquisa
Presidente da 18ª SNCT

Avanços no desenvolvimento de nanomateriais

Pierre Basílio Almeida Fechine

ORGANIZADOR



NANOPARTÍCULAS SEMICONDUTORAS

Anderson Valério Chaves
Paulo Henrique Teixeira da Silva
Samuel Veloso Carneiro
Janaína Sobreira Rocha
Pierre Basílio Almeida Fechine

Podemos caracterizar os materiais conhecidos atualmente, de acordo com suas propriedades elétricas, como: isolantes, condutores e semicondutores. Considerando suas estruturas em materiais sólidos, a classificação pode ser dada como: materiais cristalinos, policristalinos ou amorfos.

Metais e materiais semicondutores possuem uma característica semelhante quanto à dependência da resistividade com a temperatura. A teoria do orbital molecular descreve a possibilidade da transição de elétrons deslocados pelo material como o exemplo de condutores eletrônicos. Os condutores metálicos possuem uma relação inversa com a temperatura, uma vez que a resistividade elétrica diminui à medida que a temperatura aumenta. Já os materiais semicondutores tendem a aumentar sua resistividade elétrica ao se aumentar a temperatura, sendo que os metais condutores, geralmente, possuem uma resistividade elétrica maior. Finalmente, os materiais isolantes não conduzem eletricidade. Uma classe especial quanto à resistividade é a dos supercondutores, os quais possuem praticamente resistividade zero à corrente elétrica, em alguns casos, a baixas temperaturas (abaixo de 20 K), ou a altas temperaturas (100 K),